Development of Synthesis Routes for Epitaxial Oxide Thin Films

By

Jonathon L. Schad

A dissertation submitted in partial fulfillment of

the requirements for the degree of

Doctor of Philosophy

(Materials Science and Engineering)

at the

UNIVERSITY OF WISCONSIN-MADISON

2022

Date of final oral examination: 9/21/2022

The dissertation is approved by the following members of the Final Oral Committee:

Chang-Beom Eom, Professor, Materials Science and Engineering/Physics

Mark Rzchowski, Professor, Physics

Xudong Wang, Professor, Materials Science and Engineering

Jiamian Hu, Assistant Professor, Materials Science and Engineering

Thomas Tybell, Professor, Electronic Systems (NTNU)

Abstract

Using the deposition method best suited for depositing an oxide thin film can be the difference between measuring the intrinsic properties of the thin film and measuring extrinsic properties arising from defects, impurity phases, and contamination. In this work, unique synthesis routes for the deposition of three epitaxial oxide thin films is presented. Applying these new routes, new material properties were able to be discerned that had been concealed in thin films deposited utilizing conventional methods.

Dual off-axis RF sputtering of Bi-rich $BiFeO_3$ targets was employed to deposit a 1 μm-thick multiferroic $BiFeO_3$ film on various $(111)_{pc}$-orientated substrates with cubic and orthorhombic symmetries. Using non-resonant x-ray magnetic scattering (NXMS) and neutron diffraction, the magnetic domain populations in the $BiFeO_3$ were measured. We found that growing on reduced-symmetry substrate $NdGaO_3$ $(011)_o$, yields a $BiFeO_3$ film with a single ferroelectric, structural, and magnetic domain consistent across the whole sample. The single domain remains stable even after switching a region of the sample ferroelectrically up to 10,000 times. Using NXMS polarimetry we confirm that there is a change in the magnetic polarity of the $BiFeO_3$ domain after ferroelectric switching, demonstrating the coupling of the magnetic and ferroelectric orders in monodomain $(111)_{pc}$-orientated $BiFeO_3$ thin films.

Using reactive RF sputtering of a pure Fe target, phase pure deposition of antiferromagnetic insulator α-Fe_2O_3 was achieved. SQUID magnetometry confirms the absence of any ferromagnetic minority domains in the film. We showed that the Morin transition temperature, above which α-Fe_2O_3 has a weak canted moment, decreases when reducing the thickness of the film. For films 10 nm and thinner, the Morin transition was suppressed completely. Using the XMLD contrast of the 10 nm-thick α-Fe_2O_3 film, X-ray Photoemission Electron Microscopy (PEEM) measurements uncovered a complex mosaic of sub-micron size antiferromagnetic domains connected by a network of antiferromagnetic spin vortices. The vortices were mostly found in vortex/antivortex pairs which could be annihilated through the application of an

external magnetic field. When a ferromagnetic 1 nm-thick Co layer was overlayed, the mosaic of domains present in the α-Fe_2O_3 was coupled to the Co which takes on the same mosaic pattern in its ferromagnetic domain structure.

Pulsed laser deposition of SrO and chemical vapor deposition of a TiO_2 precursor gas were used simultaneously to deposit high quality $SrTiO_3$ thin films in a hybrid deposition technique we refer to as metal-organic pulsed laser deposition (MOPLD). We demonstrated a conductive 2-dimensional electron gas (2DEG) at the interface between MOPLD-grown $SrTiO_3$ and PLD-grown $LaAlO_3$, indicative that the $SrTiO_3$ thin film is highly stoichiometric. The increased stoichiometry control afforded by MOPLD also grants the ability to control the point defects in the system. By decreasing the abundance of point defects, quantum properties of $SrTiO_3$ become accessible.

Acknowledgements

Research is a group effort. None of what is presented here would be possible without the help of others whom I would like to thank. First and foremost, I would like to thank Professor Chang-Beom Eom, my close advisor over the last six years. I first got to know Professor Eom when he hired me as an undergraduate intern for the summer of 2015, at the recommendation of Professor Greg Denbeaux at SUNY Polytechnic Institute. The freedom Professor Eom has given me to pursue research pathways has been vital to my education. He has ensured that I have the hands-on experience needed to find a rewarding position in the semiconductor industry upon graduation.

I also would like to acknowledge the rest of my thesis committee including Professor Mark Rzchowski (UW – Madison, Department of Physics), Professor Xudong Wang (UW – Madison, Department of Materials Science and Engineering), Professor Jiamian Hu (UW – Madison, Department of Materials Science and Engineering), and Professor Thomas Tybell (Norwegian University of Science and Technology, Department of Electronic Systems). Their helpful feedback on my thesis proposal has guided my research.

I have had the pleasure of working alongside so many exceptional graduate students, post docs, research scientists, and visiting faculty in the Oxide Lab. Performing thin film deposition research takes a team; from brainstorming new ideas to performing maintenance and troubleshooting on equipment. First, I must thank Jungwoo Lee and Anthony Edgeton for their help in designing and building the MOPLD deposition system. Next, the $BiFeO_3$ sputtering expertise that Seung Hyub Baek and Wittawat Saenrang accrued was vital to me continuing the group's research into $BiFeO_3$, knowledge that I hope I have added to and can pass onto Pratap Pal to continue the research project. Finally, I would like to thank Shane Lindemann for his knowledge of ferroelectrics, Neil Campbell, Mike Patton, and Tianxiang Nan for performing electrical measurements, and David Harris for help in ceramic processing and sputtering. Many Oxide Lab members

were not only my colleagues but became my friends. Without their friendship in the lab and outside of it, I couldn't have completed my studies.

While I like to think Oxide Lab members are experts at growing oxide thin films, we rely on collaborators who are experts in other areas such as characterization techniques and theory. Mark Rzchowski and his group need to be thanked for their close collaboration on many projects, especially Neil Campbell and Julian Irwin for SQUID and MOKE measurements, respectively. For the characterization of the MOPLD grown STO thin films, I would like to especially thank the Brillson group (The Ohio State University) for CL measurements, the Tenne group (Boise State University) for Raman measurements, and the Pryds group (Technical University of Denmark) for SdH oscillation measurements. I need to thank the Radaelli group (Noah Waterfield Price, Francis Chmiel, Anuradha Vibhakar, and Professor Paolo Radaelli) at the University of Oxford for their novel ideas on $BiFeO_3$ research and PEEM and NXMS measurements of the samples that we grew in the Oxide Lab. Furthermore, I need to thank the Radaelli group for initiating our interest in deposition of Fe_2O_3 thin films which they extensively studied.

Lastly, I would like to thank my family for the support they have provided including my mom, Lori, and dad, Todd, as well as my sisters, Emma and Gwen. It is with their help that I have been able to pursue my K-12, undergraduate, and graduate education. Their support and guidance while preparing to defend my thesis and determining my next steps after graduate school was crucial to me completing my studies.

Table of Contents

List of Figures

Chapter 1

Introduction and Methods

1.1 Introduction to Epitaxial Oxides

Studying oxide materials as epitaxial thin films has numerous advantages over studying the materials in their bulk state. Foremost among them is the ability to create layered heterostructures and superlattices that harness interfacial states in the materials and can combine materials with different functionalities into a single system. For example, a thin film of a piezoelectric material can be combined with a thin film of a material that has magnetostriction, creating a magnetoelectric heterostructure whereby the application of an electric field causes the piezoelectric to distort changing the strain on the magnetostriction layer, changing its magnetic order. The selection of substrate for epitaxial growth is also important, imparting its symmetry and lattice parameters onto the film causing it to be strained, potentially changing its functional properties. Metastable materials that are stabilized with strain can also be grown this way.

1.2 Introduction to Thin Film Deposition

This thesis focuses on the development of new synthesis techniques for epitaxial oxides. An overview of the basic deposition methods is provided here.

1.2.1 Magnetron Sputtering

Sputtering (Figure 1-1a) is the process whereby atoms or molecules of a target material are liberated from the surface of the target by the bombardment of energetic ions. Argon is often used as a sputtering gas due to its nonreactivity with other elements even when ionized, its high sputtering yield, and relatively low cost compared to other nonreactive gases. Magnetron sputtering (Figure 1-1b) is an improvement of the sputtering process developed in the 1970s that drastically increases the deposition rate and widened the operating pressure range that sputtering can occur at. By using a set of permanent magnets embedded in the target assembly, a magnetic field above the target surface is generated trapping ionized species close to the target surface, increasing the plasma density. Instead of ions randomly bouncing about the chamber, they are concentrated at the surface of the target where they more readily hit the target surface, sputtering the material. If the target material is conducting, a simple constant high voltage bias is enough to ignite the plasma and initiate the sputtering process.

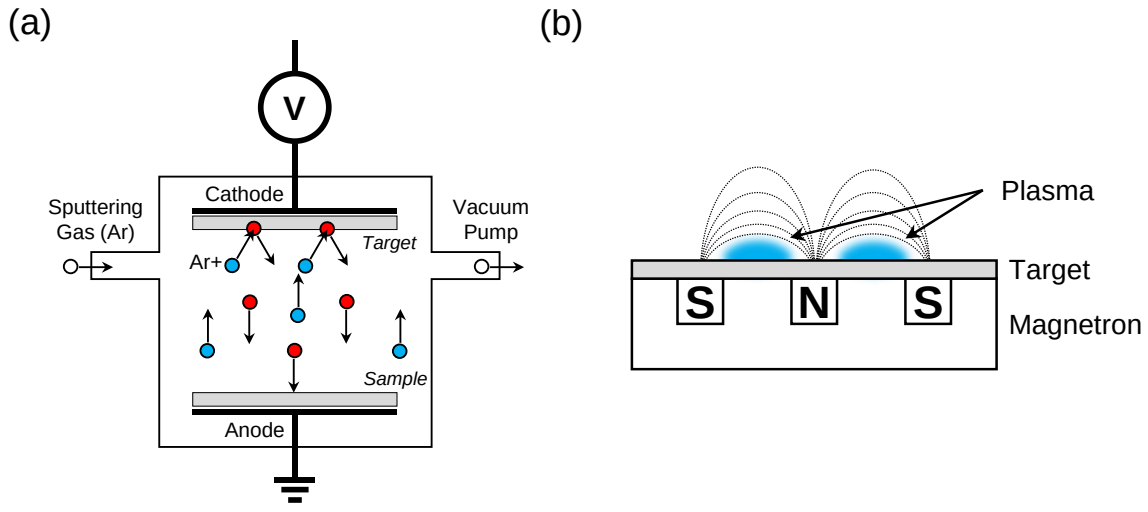

Figure 1-1: Magnetron sputtering schematic. (a) A schematic of a magnetron sputtering system. Sputtering gas (Ar) is inserted into the chamber where it ionizes and sputters atoms of the sputtering target. Some of the sputtered atoms are deposited on the sample. (b) A cross-section view of the magnetron sputtering cathode. A plasma is confined between the button magnet (N) in the middle and the ring magnet (S). The target material is mounted directly to the magnets of the sputtering source.

DC sputtering is only applicable for sputtering of conducting materials and a plasma will not be ignited if the target material has low conduction or is insulating. For these materials, RF sputtering can be useful. Instead of applying a constant high voltage bias to the target, a high frequency source, usually 13.56 Mhz, is used. The constantly varying bias of the sputtering cathode causes a buildup of charges on the insulating surface of the target, which eventually is great enough to ignite the plasma. A matching box is used to ensure that the RF source is impedance matched with the plasma, maximizing the power transferred from the source to the plasma.

Advancements have also been made in the sputtering process to obtain epitaxial oxide thin films. It was learned that placing the sample in the side of the plasma plume at a 90° angle with respect to the target surface instead of directly in front of the sputtering target, sputtering damage to the sample from negative oxygen ion bombardment can be limited[1]. High growth pressures (hundreds of mTorr) can also slow down ions before they reach the sample.

1.2.2 Pulsed Laser Deposition

Pulsed laser deposition (PLD) is a physical vapor deposition technique specifically designed for the deposition of epitaxial oxide thin films. The first uses of PLD in the 1980s were directed at the growth of high T_c cuprate superconductors[2,3] such as $YBa_2Cu_3O_{7-x}$ (YBCO). In a PLD system, a schematic of which is shown in Figure 1-2, a pulsed, high-energy KrF excimer laser (248 nm) is focused onto a rotating target material. The target material exposed to the laser is instantly vaporized and turned into a plasma consisting of ions, atoms, and molecules which adsorbs onto the surface of the sample. The technique is highly energetic with plasma energies far above what is needed to thermally evaporate the material. Thus ample energy is available for the deposited adatoms to move around the surface and form high quality epitaxial layers. The sample is also usually heated to further aide in increasing the rate of surface diffusion and a background pressure of O_2 is present to stabilize the correct oxidation state of the thin film.

One of the advantages of PLD is the few limitations it places on target material selection. The target can be electrically or thermally insulating or conductive. Also, the stoichiometry of the target is the same as what is deposited onto the sample, simplifying the growth of complex and doped oxides. The only limitation in target selection being that the material is not highly reflective in the UV regime near the wavelength of the laser, otherwise the material will ablate slowly with most of the laser's power being reflected. This can be an issue with elemental metal targets such as Au and Pt which have a deposition rate using PLD of nm/hour.

PLD systems usual come equipped with a real time *in-situ* RHEED monitoring system to keep track of the quality of the deposited film and its thickness during deposition. A high energy electron beam is diffracted off the sample at a grazing incidence and the diffraction pattern is captured using a phosphor-coated screen. From the diffraction pattern, the crystalline geometry of the sample surface, growth mode, and growth rate can be determined in real time. To use an electron beam in the high-pressure environment used in PLD (up to 1 Torr), the electron beam source must be kept at a higher level of vacuum. This is accomplished using one or more stages of differential pumping, passing the beam through a small orifice,

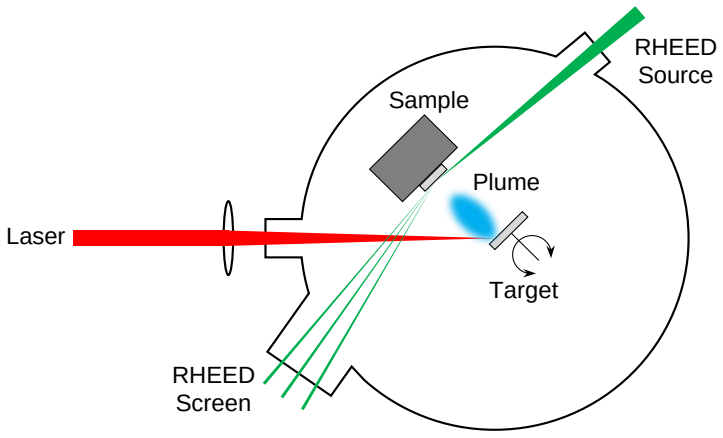

Figure 1-2: Pulsed laser deposition schematic. Schematic of a pulsed laser deposition (PLD) system. The excimer laser (in red) is focused by a lens to a small point on the target where it ablates material converting the solid target material into a plasma (in blue). The sample is aligned so that it aligned axially to the laser plume to maximize the number of ablated atoms that are deposited on the sample. A RHEED source and screen (in green) monitor the growth of the thin film in real time.

and pumping the cavities between orifices using turbomolecular pumps. At high pressures, the mean free path is also much reduced, necessitating that the final orifice be mounted on a tube that extends into the chamber minimizing the distance the electron beam must travel in the high-pressure environment.

1.2.3 Molecular Beam Epitaxy

Unlike magnetron sputtering or PLD, molecular beam epitaxy (MBE) is a near-equilibrium physical vapor deposition technique. MBE was originally developed in the 1970s for the epitaxy of III-V compounds[4]. Atomic or molecular beams of materials are generated by evaporation or sublimation of ultra-high purity source materials loaded in crucibles pointed at the sample surface. *In-situ* flux monitors are used to calibrate the flux of each beam. To ensure that the atomic beams reach the sample surface without collisions with gases molecules in the chamber, MBE is done in ultra-high vacuum (UHV) which is generally defined as pressures of 10^{-9} Torr or less. In magnetron sputtering and PLD, species arrive at the sample surface with potentially hundreds of eV of energy whereas MBE uses thermal beams with species generally having < 1 eV of energy. An absorption-controlled growth can be established using MBE for the deposition of certain compound materials such as GaAs. For growth of GaAs using MBE, the temperature of the sample is set such that only As atoms that react to form the solid GaAs compound can remain on the sample. Unreacted As on the surface desorbs and is pumped out of the chamber as a gas. If As is supplied in excess so that all Ga that reaches the surface reacts with As, the film is guaranteed to have the correct 1:1 stoichiometry. The UHV conditions present in the chamber mean that a RHEED monitoring system that is installed on an MBE chamber does not need differential pumping of the filament electron source. To grow oxides using MBE, the elemental beams are combined with a flow of O_2 gas, O_3, or atomic O plasma.

1.3 Plan of Thesis

The thesis is split into three major sections, each covering work on a specific research project and material. Each section is focused on the synthesis route taken to achieve the quality of film needed for the experiment

performed, and also includes the results of the experiments that were performed on each of the films or film heterostructures.

Chapters 2 and 3 focus on $BiFeO_3$, a multiferroic material. Chapter 2 focuses on how the films were deposited and characterized. The individual steps to make a $BiFeO_3$ device are highlighted including fabricating the sputtering target, depositing each of the layers of the heterostructure, and the fabrication steps taken to transform the stack of layers into a functioning device. A basic overview of how each of the characterization methods works and what information can be obtained about $BiFeO_3$ structure, surface, and electrical and magnetic properties is provided. Chapter 3 focuses on the studies we were done on $BiFeO_3$ $(111)_{pc}$ thin films to investigate the antiferromagnetic domains present in the films. We experimented with depositing the films on different substrates with different symmetries to see if we could affect the domain populations. NXMS and neutron diffraction were used to get data on magnetic scattering. Our data shows that we can create a $BiFeO_3$ $(111)_{pc}$ thin film with a single multiferroic domain across the whole sample and that the magnetization can be switched electrically.

Chapter 4 compares the film quality of α-Fe_2O_3 thin films deposited by RF sputtering of a Fe_2O_3 target to films deposited by reactive sputtering of a pure Fe target. Characterization was performed to determine which deposition method yielded the best crystalline quality and phase purity. Particular attention is paid to the magnetic properties of the films which was characterized by SQUID magnetometry. While SQUID can deduce the magnetization of the overall sample, we used PEEM and XMLD to generate a vector map of the antiferromagnetic spin direction for a portion of the α-Fe_2O_3 sample surface. Analysis of the vector maps showed interesting patterns including topologically protected vortices. PEEM and XMCD were used to study how the domain state of the α-Fe_2O_3 coupled to a Co ferromagnetic overlayer.

Chapter 5 gives a detailed description of how a deposition system was designed and built that could deposit thin films using our new metal-organic pulsed laser deposition (MOPLD) process. Certain design decisions we made were highlighted and discussed. $SrTiO_3$ thin films were then synthesized using the new

MOPLD technique and the film quality was compared to $SrTiO_3$ thin films synthesized using other techniques such as standard PLD. We show that the quality of the $SrTiO_3$ synthesized using the new MOPLD method improves upon the quality obtainable using standard PLD and yields a more consistent quality of film thanks to the presence of a wide growth parameter window.

1.4 References

1. Eom, C. B. *et al.* Synthesis and properties of YBa2Cu3O7 thin films grown in situ by 90° off-axis single magnetron sputtering. *Phys. C Supercond.* **171**, 354–383 (1990).
2. Dijkkamp, D. *et al.* Preparation of Y-Ba-Cu oxide superconductor thin films using pulsed laser evaporation from high T c bulk material. *Appl. Phys. Lett.* **51**, 619–621 (1987).
3. Moorjani, K. *et al.* Superconductivity in bulk and thin films of La1.85Sr0.15CuO4−δ and Ba2YCu3O7−δ. *Phys. Rev. B* **36**, 4036–4038 (1987).
4. Cho, A. Y. & Arthur, J. R. Molecular beam epitaxy. *Prog. Solid State Chem.* **10**, 157–191 (1975).

Chapter 2

Deposition and Characterization of $BiFeO_3$ Thin Films

2.1 Introduction to $BiFeO_3$

Bismuth ferrite ($BiFeO_3$ or BFO) is a complex oxide that is multiferroic at room temperature, exhibiting ferroelectric, ferroelastic, and antiferromagnetic ordering simultaneously in a single phase. The coexistence of these orders along with the observation of coupling between the electrical and magnetic order parameters, makes $BiFeO_3$ a leading material candidate in the search for beyond CMOS logic and memory architectures. Structurally, $BiFeO_3$ has a noncentrosymmetric rhombohedral R3c perovskite crystal structure[1,2] with lattice parameters of a = 3.964 Å and α = 89.4°. The perovskite unit cell consists of Bi at the A-site (corner) cation position, Fe at the B-site (central) cation position, and an oxygen anion octahedral cage surrounding the central Fe cation (Figure 2-1a). As shown in Figure 2-1b, the unit cell is distorted along the [111] direction below the ferroelectric phase transition (T_C) at ~ 1100 K originating from the lone pair mechanism[3] whereby Bi s^2 electrons hybridize with neighboring O *p* electrons. The polar distortion of $BiFeO_3$ leads to a rather large spontaneous polarization[4] of ~ 90 μC cm^{-2}. The large ionic radii mismatch between Bi and Fe causes alternating oxygen octahedra tilting along the [111] following an *a*-*a*-*a*- tilting by Glazer notation[5]. Antiferromagnetic ordering is present in $BiFeO_3$ below T_N ~ 640 K[6].

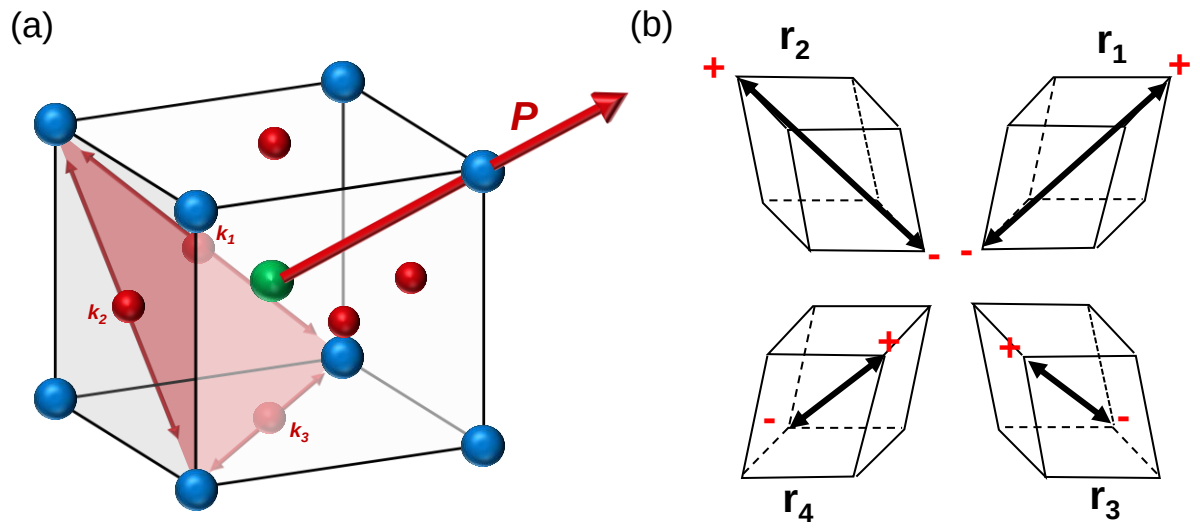

Figure 2-1: $BiFeO_3$ perovskite unit cell. (a) Pseudocubic unit cell of $BiFeO_3$ where blue ions are bismuth, green ion is iron, and red ions are oxygen. Polarization vector along [111] direction denoted as P. Possible spin cycloidal vectors for P are denoted as k_1, k_2, and k_3. (b) A schematic of the four possible structural variants (r_1, r_2, r_3, r_4) and eight possible polarization vector directions ($r_1^{\pm}$, $r_2^{\pm}$, $r_3^{\pm}$, $r_4^{\pm}$) for rhombohedral phase $BiFeO_3$.

$BiFeO_3$ was first synthesized in the 1950s, followed a few years later by the identification of its R3c structure[1,2]. Confirmation of ferroelectricity came in 1970 when a hysteresis loop was fist measured on a bulk crystal[7]. Neutron diffraction experiments in 1963 revealed that $BiFeO_3$ was a G-type antiferromagnet[6]. Additional experiments in 1982 were the first to show that a more complex spin cycloidal ordering of spins was present on top of the G-type ordering[8]. In 2003, epitaxial thin films showed that $BiFeO_3$ had one of the largest spontaneous polarizations of any ferroelectric[4], jumpstarting the scientific interest in the material as a multiferroic.

2.2 Sputtering Target Fabrication

To deposit a thin film of $BiFeO_3$ using RF sputtering a high density ceramic $BiFeO_3$ target is needed. $BiFeO_3$ sputtering targets were synthesized using the solid-state reaction method using Bi_2O_3 powder (99.9%, Sigma Aldrich), Fe_2O_3 powder (99.9%, Alfa Aesar), and 0.5% by weight binder and plasticizer (Butvar 76 and Solusolv 2075 respectively). To compensate for volatile Bi_2O_3 flux lost during sintering and during

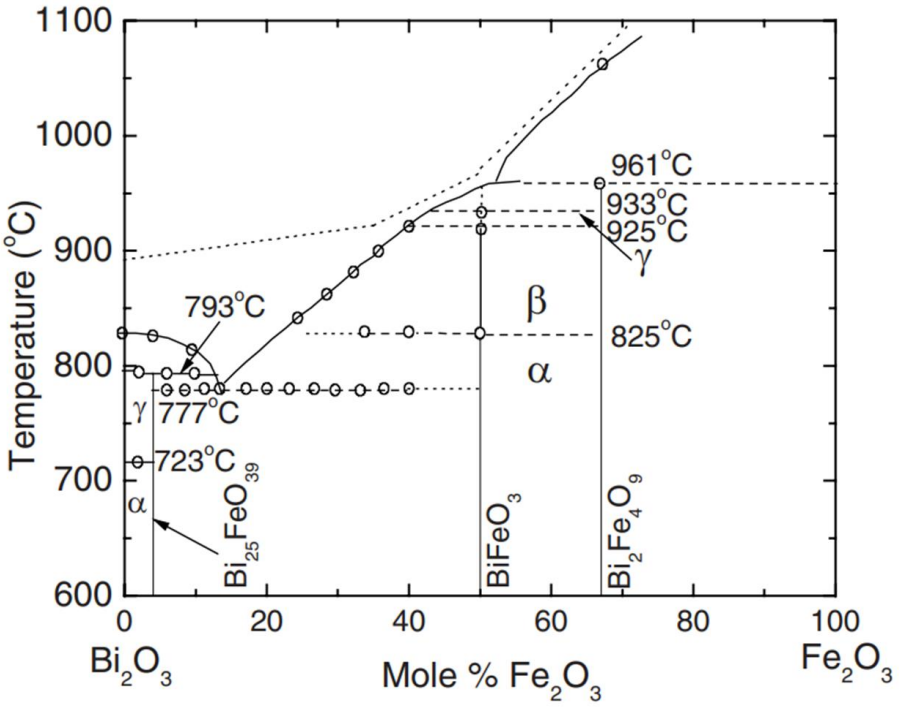

Figure 2-2: $Bi_2O_3 – Fe_2O_3$ binary phase diagram. The α, β, and γ phases are rhombohedral, orthorhombic, and cubic, respectively. Reproduced from reference[22] with permission from Physical Review B.

sputtering deposition, between 2.5%-5% excess Bi_2O_3 powder was added to the starting mixture. If excess Bi_2O_3 powder is not added to the target, the resulting thin films become Fe-rich and are mixed phase with both $BiFeO_3$ and $Bi_2Fe_4O_9$ phases present in the film. The powders were mixed and then milled in a planetary ball mill at 400 rpm for 1 hour using a Retsch PM 100 with YSZ milling jar. To maximize mixing and particle size reduction during milling, equal volume powder and 5mm spherical Yttria-stabilized cubic zirconia (YSZ) milling media was used along with enough isopropyl alcohol (IPA) so that the consistency of the slurry was that of motor oil. After milling, the slurry was poured into a drying dish and the isopropyl alcohol was evaporated off. The milled powder was then sieved through an 8-inch diameter #120 steel mesh (125 μm) sieve and around 70 grams of powder was weighed out for each target.

2.2.1 Optimizing Target Fabrication

Previous methods to create $BiFeO_3$ targets for RF sputtering[9,10] followed a process that included a calcination step followed by pressing and then sintering, yielding a 95+% dense target. With a calcination anneal step of 2 hours at 850°C, the resulting powder successfully reacts to form the $BiFeO_3$ phase, but also sinters. The partially sintered powder requires processing of the powder using a mortar and pestle or planetary ball mill to reduce the particle size so that it can be sieved again. Once this is accomplished, the powder is pressed and sintered at 910°C for 8 hours resulting. For all targets, the powder was loaded into a 2.125-inch die set and pressed with a Carver 25-ton hydraulic press at 10 tons for 1 minute. Pressure was released from the die over 5 minutes to slowly relieve pressure on the target, preventing target cracking. In Figure 2-3a, the powder x-ray diffraction data from target using a separate calcination step is shown. Diffraction peaks from both the Bi- and Fe-rich phases $Bi_{25}FeO_{39}$ and $Bi_2Fe_4O_9$, respectively, are present indicated a phase decomposition has occurred. Phase diagrams of the Bi_2O_3–Fe_2O_3 system (Figure 2-2) shows that $BiFeO_3$ is stable from room temperature up to 830°C but reports show that the phase is only metastable[11,12]. The $BiFeO_3$ peaks are also shown to be speckled indicating a growth in crystalline size,

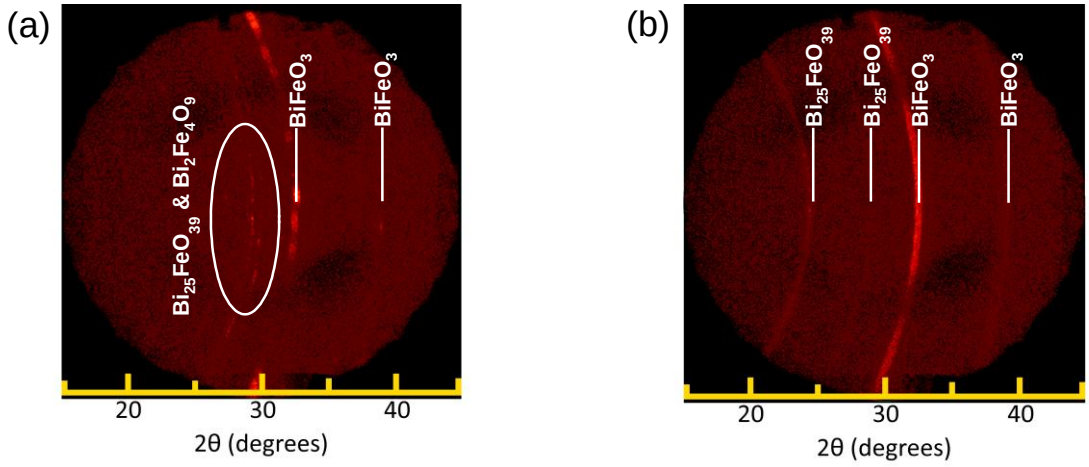

Figure 2-3: 2D out-of-plane x-ray diffraction scan of $BiFeO_3$ sputtering targets. The target with separate calcination and sintering steps (a) shows that some of the $BiFeO_3$ has phase separated into Bi-rich $Bi_{25}FeO_4$ and Fe-rich $Bi_2Fe_4O_9$. The grain size of the two-step target also was much larger than the one-step target evident by its spotty diffraction pattern. This is not ideal for a sputtering target.

which is also due to the high sintering temperature. To create a single-phase target without crystalline growth, a process that subjects the material to the minimum temperature for the minimum amount of time that is required to both calcine and sinter the target is desired. This can most easily be accomplished by combining the calcination and sintering steps into one anneal which has been shown to not cause target cracking if the volume change during calcination is small.

To determine the minimum temperature required to calcinate and sinter the starting powder mixture, a series of experimental runs were done for 4 hours at various temperatures. Diffraction peaks for the perovskite $BiFeO_3$ phase started to appear at 650°C. Above 750°C, full calcination to the perovskite phase is shown to occur evident by the disappearance of Bi_2O_3 and Fe_2O_3 peaks in the out-of-plane x-ray diffraction shown in Figure 2-4. Due to the excess Bi_2O_3 used in the starting mixture, a peak remains near where the Bi_2O_3 peak was. This is most likely a $Bi_{25}FeO_{39}$ peak which is isostructural with the Bi_2O_3 γ phase[13]. Above 800°C, a sufficiently dense target of 95% was achieved. The final optimized sintering conditions was determined to be to heat the target at 400°C for 4 hours to burn off the binder used to keep

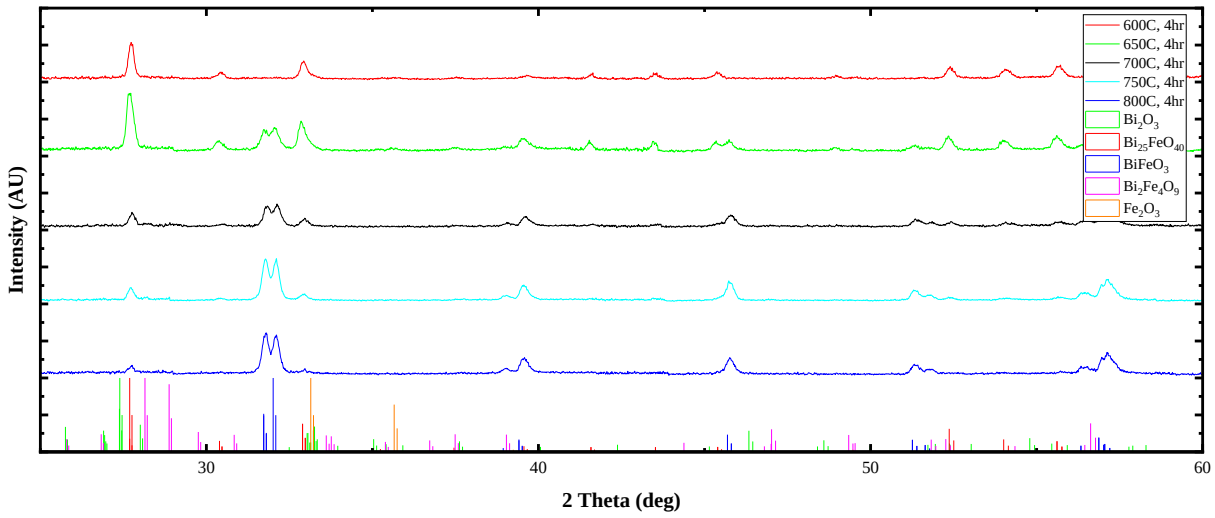

Figure 2-4: Out-of-plane powder x-ray diffraction scans of Bi_2O_3 and Fe_2O_3 powder mixtures with an atomic ratio of 1.05:1 annealed at various temperatures for 4 hours, compared to the delta functions of compounds found on the Bi_2O_3 – Fe_2O_3 binary phase diagram. Above 700°C, the powder is shown to have calcinated into the complex oxide along with a small amount of $Bi_{25}FeO_4$ due to the excess Bi_2O_3 used.

the loose powder together, then raise the temperature to 800°C for 8 hours to calcine and sinter. Doubling the final sintering step duration to 8 hours increased the density of the target from 94.4% to 98.1% without changing the phase of the target. Figure 2-3b shows a single phase $BiFeO_3$ target with small crystalline size with the optimized one-step process.

2.2.2 Preparing Target for Sputtering

Before using the target for sputtering, under growth pressures the RF power applied to the target was slowly ramped at approximately 10 watts every 30 minutes until the operating power of 100 watts was reached. The target was held at 100 watts for another 5 hours to complete the preconditioning of the target before use.

The ceramic target was mounted into a copper cup with 1/16-inch thick backing and sidewalls. The job of the copper cup is both to provide structural support to the ceramic target and to aide in heat transfer between the ceramic and the water block of the sputtering cathode. Two methods were used to mount the ceramic target into the copper cup. For the first method, a two-part 1:1 EPO-TEK H20e silver epoxy was thoroughly mixed and around 2 grams for each assembly was applied coating both the ceramic target and copper cup before placing the target into the cup. The assembly was then heated on a hot plate overnight at 120°C to fully cure the epoxy. Alternatively, Indium bonding was employed. The target and cup were heated to 175°C along with 2.5 grams of 99.99% Indium shot. Once the shot melted, the Indium was spread out to cover the mating surfaces of both the target and cup before joining the two parts and letting the assembly cool. Indium bonding, of the two methods, has the better thermal conductivity and is malleable, reducing cracking of the brittle ceramic target from thermal expansion coefficient mismatches.

2.3 Thin Film Deposition

First, a thin film of strontium ruthenate ($SrRuO_3$ or SRO) was deposited on the substrate. The $SrRuO_3$ layer has multiple roles. $SrRuO_3$ is a conductive oxide and acts as a bottom/ground electrode in out-of-plane

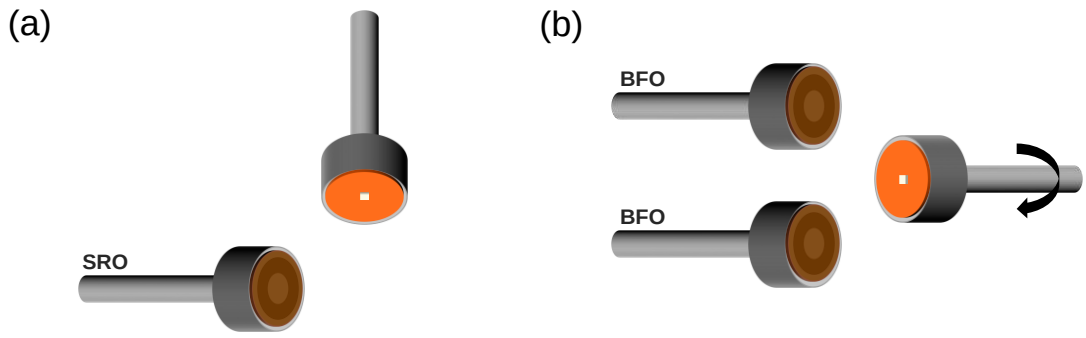

Figure 2-5: Sputtering geometry used to sputter $SrRuO_3$ and $BiFeO_3$. For $SrRuO_3$, the sputtering cathode was positioned perpendicular to the face of the substrate heater assembly. For $BiFeO_3$, both sputtering cathodes are positioned parallel to the substrate heater face but are offset by 1.5 inches from the heater's centerline. Off-axis sputtering techniques are used to produce higher-quality thin films.

devices or for measurements such as piezoelectric force microscopy (PFM). Secondly, it provides a depolarization field that orientates the polarity of the $BiFeO_3$. It also acts as a buffer material usually being more closely lattice matched to $BiFeO_3$ than the substrate. To deposit $SrRuO_3$, RF sputtering of a stoichiometric $SrRuO_3$ target was employed. The target was obtained commercially from Praxair Specialty Ceramics and attached to a MeiVac 2-inch spherical MAK magnetron sputtering cathode. The sputtering geometry was 90 degrees off-axis as shown in Figure 2-5a. Off-axis sputtering avoids backsputtering damage from negative ions that occurs when sputtering on-axis, leading to a superior film quality[14]. Using the side of the sputtering plume also yields better thickness uniformity across the sample. The trade-off of off-axis sputtering is the slower growth rate versus on-axis sputtering. A 3.0-inch MeiVac HTR substrate heater was used with an embedded PID-controlled thermocouple for temperature regulation. 100 watts of RF power was applied to each of the two targets. The temperature was held at 600°C during film growth followed by rapid post-growth cooling in 300 Torr of O_2. Growth pressure was a 3:2 Ar:O_2 gas mixture at 200 mTorr.

$BiFeO_3$ was deposited by using dual off-axis sputtering, as shown in Figure 2-5b. The technique has the advantage of low backsputtering damage because of the offset design but with a faster deposition rate than 90 degree off-axis sputtering[15]. Two MeiVac 2-inch spherical MAK magnetron sputtering cathodes spaced 3-inches apart were used to sputter the stoichiometric (with excess Bi to offset volatility) targets. To heat the samples during deposition, a 2.0-inch MeiVac HTR substrate heater was used for *ex-situ* heterostructure samples while a 1-inch TSST button heater was used for the *in-situ* heterostructure samples. The heater was placed at a working distance of 1.75-inch from the plane of the sputtering target surface. The growth temperature was 740°C followed by rapid post-growth cooling in 300 Torr of O_2. Growth pressure was a 3:1 Ar:O_2 gas mixture at 400 mTorr.

2.4 Design of in-situ Metal Deposition

For spintronics applications, the 'cleanliness' of the $BiFeO_3$/metal interface is essential for the proper transfer of spins across the interface. *Ex-situ* deposition of the metal overlayer can lead to carbon contamination of the $BiFeO_3$ surface when transferring the sample between deposition systems. The idea then is to use *in-situ* deposition, where the sample stays under high vacuum and is not exposed to atmosphere between depositing of the layers of the heterostructure. One system design concept for *in-situ* sputtering would be to use the same vacuum chamber to sputter both $BiFeO_3$ and metals. To prevent cross-contamination between the high vacuum, oxygen free metal sputtering process and the low vacuum, oxygen-based sputtering of $BiFeO_3$, separate deposition chambers is desired. We designed and built a system that connects two isolated chambers for metals and $BiFeO_3$ sputtering with a detachable and movable substrate heater block that can be transferred from one chamber to another, as seen in Figure 2-6a.

The original system that we built for dual off-axis sputtering of $BiFeO_3$ used a simple 16-inch diameter spherical vacuum chamber with a 2.0-inch MeiVac HTR substrate heater. To avoid needing to reoptimize the process of sputtering $BiFeO_3$, it was necessary to not modify the original chamber. A custom

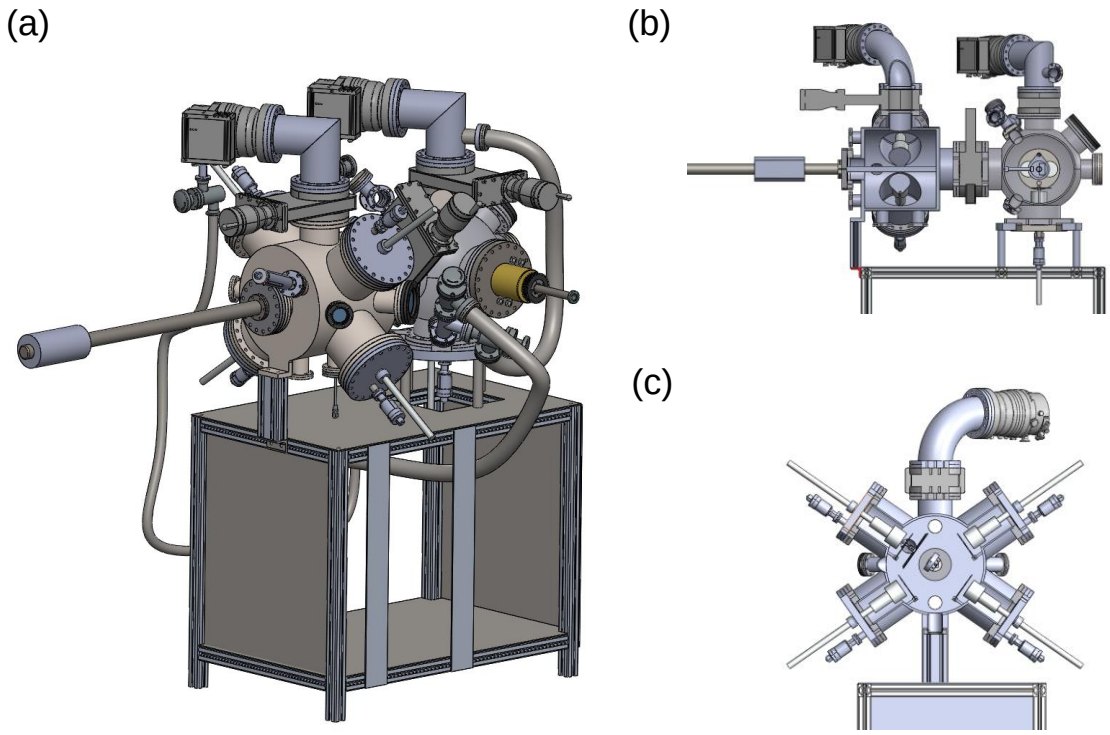

Figure 2-6: BFO/metal sputtering deposition system schematic. (a) Isometric view of the BFO/metal sputtering deposition system. (b) Side view of the system showing the high vacuum metals sputtering chamber on the left side and the BFO sputtering chamber on the right. (c) Cross-sectional view of the metals sputtering chamber showing the four ports available for the mounting of sputtering cathodes. The sample stage is rotated using the transport arm to face the sputtering cathode to be used to perform on-axis sputtering.

cylindrical vacuum chamber was fabricated and attached to the $BiFeO_3$ sputtering chamber using an 8-inch diameter gate valve. Mounting points for the additional chamber were designed in such a way as to utilize the existing chamber support frame to support the new chamber as well. In Figure 2-6b, a cross-sectional view of the system is shown with the metals chamber on the left, gate valve in the middle, and the original $BiFeO_3$ chamber on the right. Figure 2-6c shows a cross-sectional view of just the metals sputtering chamber. Four 8-inch ConFlat ports are used to mount one or more sputtering cathode assemblies on each port. Additional, smaller ports were added to mount quartz microbalance (QCM) growth rate monitoring sensors, a set of retractable magnets for applying an external magnetic field to the sample during sputtering,

and for an optical viewport. A turbomolecular pump, vacuum gauges, and process gas inlet was also accommodated for.

It was determined that there was no design that would allow the original MeiVac HTR substrate heater to be used in the new system. If the $BiFeO_3$ and metals sputtering chambers must be isolated from one another, then the electrical connections to the substrate heater, used to heat and control the temperature during $BiFeO_3$ growth, need to be disconnected to move the heater to the metals sputtering chamber. The MeiVac HTR substrate heater has screw posts for its power leads which use fork-style crimped wire connectors that need to be tightened down to make a good electrical connection. Thus, connecting the heater to the power feed wires is a manual process that is done outside of the chamber and achieving a low resistance connection can be difficult due to the insulating coating of $BiFeO_3$ that is sputtered on the connections each deposition. We decided to switch the substrate heater to a 1-inch TSST button heater. The TSST sample heater is designed from the start for in-vacuum transport using sliding pin connectors for all electrical connections and including a M8-1.25 treaded post for attaching to a transfer arm. A new stage was built up around the new heater so that the new or original stage could be used interchangeably. Re-optimization of the sputtering process was required as the heater surface temperature varied between designs when set to the same temperature. To transfer the sample between chambers a rotary and linear motion magnetically coupled transport arm was used. The linear motion moved the sample from chamber to chamber while the rotary motion was used to thread the sample heater's threaded post onto the mating end of the transport arm. Once tightened onto the end of the transport arm, the rotary motion was used to reorient the heater to face one of the ports on the metals sputtering chamber used for mounting sputtering cathodes. A digital tilt meter was affixed to the transport arm manipulator to align the sample heater to a port so that it is directly on-axis with the port and the sputtering cathode. As seen in Figure 2-6, no load lock was added to the system for transferring samples and sample heaters in and out of the chambers. The sample loading/unloading procedure was to remove the $BiFeO_3$ sample heater stage to mount the heater

with a new sample, deposit $BiFeO_3$, transfer the sample to the metals sputtering chamber to deposit metals, transfer the sample back to the $BiFeO_3$ sputtering chamber, and then vent the $BiFeO_3$ sputtering chamber to atmosphere to remove the sample. This was the preferred method as it kept the metals sputtering chamber always under vacuum, and the $BiFeO_3$ sputtering chamber needed to be vented to atmosphere to be able to wipe clean the surface of the sputtering targets between depositions.

2.4.1 Sample Heater Rotational Feedthrough

To counteract the anisotropic deposition rate uniformity inherent in the dual off-axis sputtering design, the sample is slowly rotated about the sample surface normal during deposition. A homemade rotational feedthrough for the heater power and thermocouple wires that was capable of continuous rotation was developed, a schematic of which is provided in Figure 2-7a. This design used a dynamic Viton O-ring where the O-ring was fixed but the shaft that it was sealing around was moving, which eventual leads to failure of the O-ring and vacuum leaks due to friction. This problem is exacerbated when the O-ring temperature is elevated from the sample heater and becomes softer and easier to damage from friction. With a maximum power output of 450 watts for the MeiVac substrate heater, specific consideration for the heating of nearby

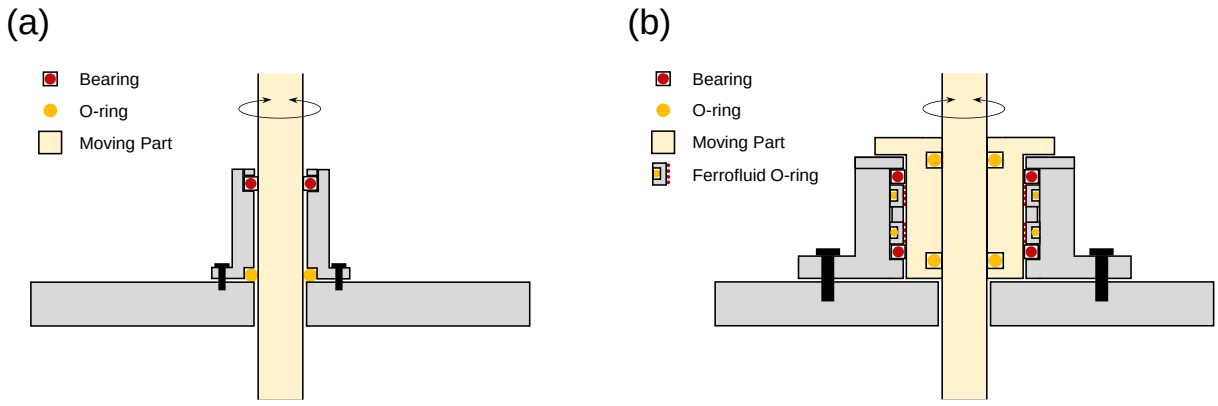

Figure 2-7: Rotational feedthrough schematic. (a) Feedthrough design that uses a single dynamic O-ring to seal between the chamber and the rotating ¾-inch hollow shaft of the sample heater. (b) More robust feedthrough design that uses a ferrofluid liquid O-rings to seal between the fixed chamber side and the rotating shaft. The shaft clamps into a moving cartridge and dual redundant static O-rings seal between the shaft and the cartridge.

parts of the chamber needs to be considered. The heater is thermally isolated from the heater mount through ceramic standoffs and the low pressure inside the chamber means that most of the power output of the heater is radiatively transferred heating the chamber itself and other components attached to it. One solution to limit the heating of the Viton O-ring seal was to point a computer fan (120 mm diameter) at the location of the O-ring. The fan successfully cooled down the area of the O-ring, but as the O-ring is located internally, heating and degradation of the seal was still occurring, although at a much-reduced rate. Replacement of the O-ring seal required complete disassembly of the sample heater stage which took over an hour. Additionally, thermal cycling from the sample heater caused parts of the stage to sometimes bind together which could lead to damage of fragile parts like ceramic standoffs when disassembling the stage.

We replaced the homemade sample heater rotational feedthrough with a FerroTec ferrofluidic vacuum feedthrough shown in Figure 2-7b. The ferrofluidic feedthrough works using a ring of fixed magnets placed around the rotating shaft, which is magnetically permeable. When a ferrofluidic solution is injected in the radial gap between the magnetic pole pieces and the shaft, a magnetic circuit is completed and a vacuum tight seal around the rotating shaft is created. The ferrofluidic solution rearranges in the magnetic field of the magnets in the shape of an O-ring. Multiple ferrofluid seals are used in series with each capable of holding a 0.2 atmosphere differential. Water cooling of the seals is used to prevent breakdown of the ferrofluid from heat from the sample heater. This new rotational feedthrough has worked to rotate the $BiFeO_3$ heater during deposition without failure since installation.

2.5 Device Fabrication

To create a standard out-of-plane device, a top metal electrode was deposited via DC magnetron sputtering. To prevent oxidation of easily oxidized metals, a UHV (10^{-8} Torr or below) base pressure was used before sputtering. For devices where the $BiFeO_3$/metal interface quality was important, the metal was ideally sputtered *in-situ* without exposing the sample to atmosphere between depositing the $BiFeO_3$ and metal

layers. To pattern the metal layer, S1813 positive photoresist was spin coated onto the surface and then baked. The resist was then exposed using a SUSS MicroTec MJB3 contact mask aligner and developed using 2% dilute TMAH developer. Ar ion milling was utilized to pattern the metal layer after which the sample was dipped in acetone to remove the photoresist mask. The liftoff process was used if depositing the top electrode *ex-situ* was acceptable. To make electrical contact with the buried bottom electrode, a scribe line was made through the $BiFeO_3$ using a diamond scribe and a silver electrode was painted onto the surface. Annealing of the finished device at up to 200°C was found to reduce the leakage of the ferroelectric hysteresis loop.

2.6 Characterization

Various characterization techniques were carried out to determine the quality of the deposited thin films for the purpose of optimizing growth conditions. Characterization can be roughly split into categories, structural, surface, and electrical. Techniques from each of these categories was employed to characterize samples for the purpose of optimizing the deposition of the thin film.

2.6.1 X-ray Diffraction

X-ray diffraction (XRD) is widely used to analyze the crystallinity and structural properties of the sample. X-ray wavelengths are on the same scale as the inter-atomic spacing of atoms in a crystalline structure leading to a large scattering factor between incident x-rays and electrons of the atoms. Figure 2-8a shows the typical x-ray diffraction setup consisting of a monochromatic x-ray beam source, a translatable/rotatable sample stage, and a detector which can also be rotated about the sample. The angle between the incident beam and the diffracted beam is 2θ. Depending on the angle of the incident beam to the crystalline structure of the sample, the reflected x-ray waves from each atomic plane in the sample will either constructively or deconstructivity interfere with each other. The angles that constructively interfere is dependent on the wavelength used and the interatomic spacing d_{hkl}, given by the Bragg's Law equation $n\lambda = 2d_{hkl}\sin\theta$. In

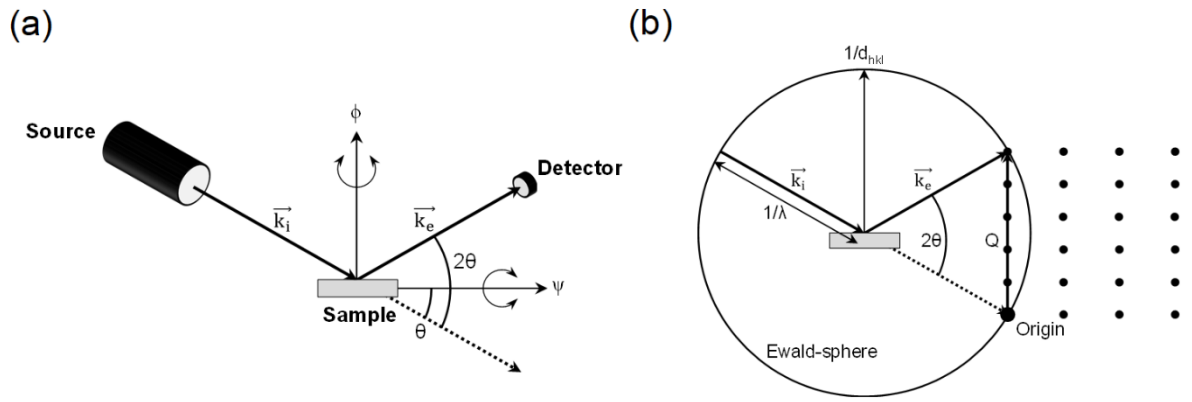

Figure 2-8: X-ray diffraction setup in real space and reciprocal space. (a) Real space schematic of a typical four circle (θ, 2θ, ϕ, and ψ) diffractometer setup. X-rays from the source scatter off the sample surface. Scattered x-rays constructively interfere yielding a diffraction condition when the geometry meets the Bragg's Law condition of $n\lambda = 2d\,sin\,\theta$. (b) Reciprocal space schematic of a diffraction condition. A diffraction condition is met when $Q = d^*_{hkl}$.

reciprocal space, as shown in Figure 2-8b, a lattice of peaks exists with a spacing of $1/d_{hkl}$ where the Bragg's Law condition is met. If the difference, Q, between the incident x-ray beam k_i and the diffracted x-ray beam k_e is equal to an integer multiple of the reciprocal interatomic spacing, diffraction occurs. Any reciprocal space point can be accessed if the system geometry is allowed. The intensity of the diffracted beam is determined by a structure factor dependent on the arrangement of the atoms as well as the elemental composition.

2.6.2 Nonresonant X-ray Magnetic Scattering

Nonresonant x-ray magnetic scattering (NXMS) is the component of the elastically scattered cross-section of photons that can be contributed to the magnetic ordering of the crystalline material, the measurement of which can be accomplished with the setup that is shown in Figure 2-9a. Nonresonant refers to the fact that the x-ray beam energy is not tuned to the gap in energy levels in the material and no energy is exchanged between the x-ray photons and the atoms of the material, which occurs for so-called elastically scattered x-rays (Figure 2-10b). This usually means for nonresonant techniques, a beam with higher energy (> 5 keV) is used. The intensity of nonresonant magnetic scattering is typically many orders of less than that of

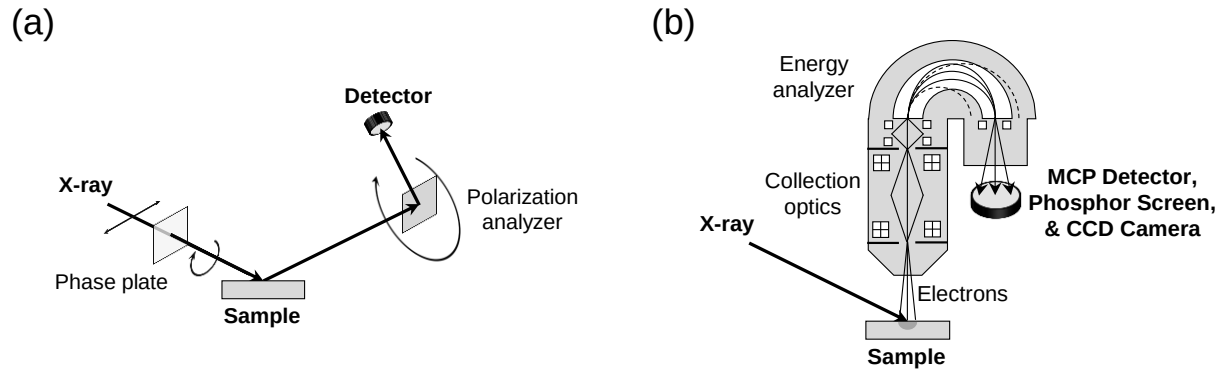

Figure 2-9: Setup for synchrotron beamline characterization techniques. (a) Schematic of Nonresonant X-ray Magnetic Scattering (NXMS). (b) Schematic of X-ray Photoemission Electron Microscopy (PEEM). A polarized x-ray beam hits the sample and emitted photoelectrons are collected by the collection optics of the PEEM detector. A hemispherical analyzer then screens the energy of the photoelectrons. Finally, the photoelectron signal is amplified by a multichannel plate, converted to light with a phosphor screen, and a digital image taken with a CCD camera.

nonresonant charge scattering. The ratio can be calculated using Equation (2-1) by multiplying the ratio of nonresonant magnetic scattering to charge

$$\frac{I_{Magnetic}}{I_{Electronic}} = \frac{N_m}{N_c}\left(\frac{\hbar\omega}{mc^2}\right)^2 \frac{f_m^2}{f_c^2} \tag{2-1}$$

scattering $\left(\frac{\hbar\omega}{mc^2}\right)^2$, the ratio of magnetic (N_m) to nonmagnetic (N_c) electrons present in the material, and the ratio of magnetic (f_m) to charge (f_c) form factors. Considering the case of Fe at a beam energy of 10 keV, the magnetic scattering is 10^{-6} weaker than the charge scattering[16]. Furthermore, the magnetic scattering is also polarization dependent. By selecting for diffraction conditions that maximize the magnetic scattering and minimize the normally overpowering contribution from charge (Thomson) scattering, we can isolate the contribution from magnetic scattering. With the correct diffraction geometries, the full magnetic structure of a material can be solved using NXMS[17].

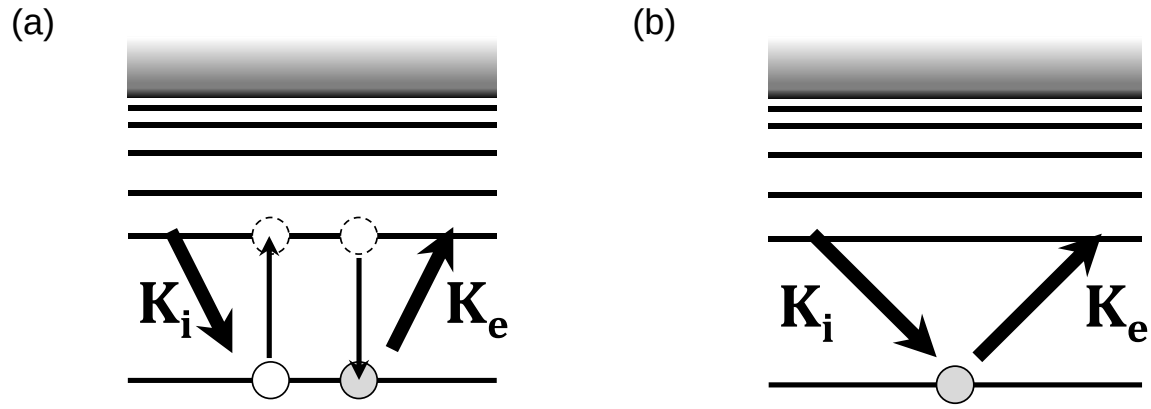

Figure 2-10: Types of x-ray scattering. (a) Resonant electron scattering. The x-ray photon tuned to the difference in energy levels is absorbed by the atom exciting a core electron to a higher energy state. A photon is later remitted when the electron returns to the ground state. (b) Nonresonant electron scattering. No energy is absorbed by the atom.

2.6.3 X-ray Photoemission Electron Microscopy

X-ray photoemission electron microscopy (PEEM) is a form of electron microscopy that collects the electrons that are emitted from the sample via photoemission that result from the energy absorbed by the sample from the incident x-ray beam. It is therefore an indirect measurement of x-ray absorption. If the x-ray energy is well matched to the atomic transition energies for the elements in the sample, there is a possibility that the x-ray photon will be absorbed by the material. When the atom relaxes by filling the core level electron hole, the energy absorbed is finally released, usually by Auger decay. This describes resonant scattering as shown in Figure 2-10a. The absorption of energy that occurs causes a core level electron to jump to a higher energy level leaving a core electron hole. If an electron microscope is used to collect the emitted electrons as shown in Figure 2-9b, a spatial map can be created to map the spatial variations in absorption by the sample surface. This is a surface sensitive technique due to the limited penetration depth of the secondary electrons generated. While the penetration depth of x-ray beam in large[18], only electrons generated at or a few nanometers from the surface will escape the sample and be collected by the detector while electrons generated in the bulk will be reabsorbed by the material[19]. A synchrotron x-ray source is

usually used for PEEM due to the capability of tuning the x-ray energy to maximize the absorption of x-rays by selecting beam energies at the absorption edge of elements present in the sample. As with other electron microscopy techniques, PEEM requires a sufficient quality of vacuum so that the electron mean free path length in the system is significantly larger than the distance between the sample and the detector.

2.6.4 X-ray Dichroism

X-ray PEEM is especially relevant to the study of magnetic materials when used in conjunction with x-ray magnetic dichroism where x-ray photoabsorption is anisotropic due to the orientation of spins in a material. Dichroism, or "two-colored", is the effect whereby photon absorption is dependent on polarization direction. If the energy of the x-ray beam is tuned to the absorption edge of an element with magnetic spin, a difference in adsorption can be observed for different polarizations of the incident beam. When there is a difference in the absorption of right versus left hand circularly polarized light, it is called x-ray magnetic circular dichroism (XMCD). When there is a difference in the absorption of horizontal versus vertical linearly polarized light, it is called x-ray magnetic linear dichroism (XMLD).

2.6.5 Neutron Diffraction

Thermal neutrons emitted from a nuclear reactor with a wavelength of similar length to the interatomic spacing of crystalline materials are also useful for the purpose of diffraction. A 25 meV neutron has a wavelength of approximately 1.8 Å, close to the 1.54 Å wavelength of $Cu_{K\alpha}$ x-rays. Unlike x-rays however, which are readily absorbed by the material, neutrons have a large penetration depth making them suitable for the measurement of bulk samples or very thick thin films. Also, unlike x-rays which scatter off the cloud of electrons surrounding the nucleus of the atom and thus scatter more readily off heavier atoms with more electrons, neutrons can also be scattered by the atomic nuclei via the strong force, called nuclear scattering which is not proportional to the atomic number and can be useful for measuring of light elements that have a small scattering cross-section with x-rays.

Scattering of neutrons off the electron cloud also occurs and is useful for magnetic scattering experiments. The magnetic moment of the neutron can interact with the unpaired electrons in a magnetic material. Importantly, the scattering amplitude from magnetic scattering of neutrons is on the same order as from scattering from the atomic nucleii[20] and thus has historically been used more readily for the study of magnetic materials than x-rays which have a magnetic scattering amplitude many orders of magnitude smaller than from charge scattering. The very first use of neutron diffraction was in the study of the antiferromagnetism in MgO[21].

2.6.6 Atomic Force Microscopy

To study the surface morphology of $BiFeO_3$ thin films atomic force microscopy (AFM) was used. In tapping mode AFM, an oscillating, atomically sharp tip is scanned over the area of the surface to be studied. By observing how the tip is deflected when the tip comes in close contact with the sample surface, a topological map of the surface can be created. The deflection of the tip is measured using a quadrupole photodiode which detects the light from laser diode reflecting off the backside surface of the tip as shown in Figure 2-11a. In Figure 2-11b, the deflected laser beams position on the photodiode sensor is shown. The measured

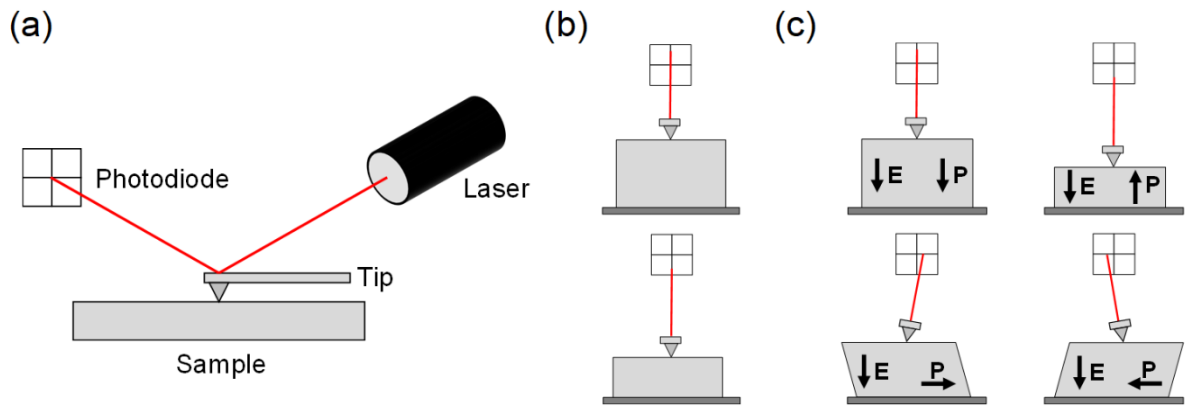

Figure 2-11: Schematic of the operation of the atomic force microscope. (a) The deflection of an atomically sharp tip deflects light from a laser diode, changing the position of the beam on the photodiode. (b) Deflection of the tip caused by topography changes. (c) Deflection of the tip during piezo force microscopy caused by out-of-plane piezo response (top) and in-plane response (bottom).

topology map is a convolution of the tip and surface geometries meaning the larger the effective tip radius of the tip, the worse the resolution is. Tapping mode is preferred for hard thin films like oxide materials that were studied as it limits the contact the tip has with the surface, preventing degradation of the tip. Contact mode AFM is the alternative method in which the AFM tip is in constant contact with the sample surface instead of oscillating. AFM was used to catch deposition problems run to run and was useful to determine if the thin film grew by the correct growth mode, if there were any particle contamination on the film, or if any secondary phases were present.

Beyond measuring surface morphology, functional properties of the surface can also be measured using AFM. By selecting a tip that has been coated in a conductive metal coating, electrical measurements such as piezoresponse force microscopy (PFM). With PFM, the direction of the polarization vector in piezoelectric and ferroelectric thin films can be deduced. PFM is a contact mode technique where an oscillating electric potential is applied between the tip and the sample. For this reason, the sample must be properly grounded. For out-of-plane $BiFeO_3$ devices, silver paint is used to connect the bottom $SrRuO_3$ electrode with the sample puck and instrument ground. A diamond scribe is used to scratch through the insulating $BiFeO_3$ layer so that the silver paste can contact the buried bottom electrode. Figure 2-11c shows that the piezoresponse to the electric field from the tip causes a distortion in the material which can be observed by the tip's deflection. The electric field oscillations are picked up by a lock-in amplifier so that the steady state deflection of the tip by the sample topology can be deconvoluted from the piezoresponse. Out-of-plane distortions of the material's surface cause the tip to be deflected up and down, while in-plane distortions cause the tip to be deflected right and left. Using PFM, a map of ferroelectric domains present in $BiFeO_3$ thin films can be observed.

2.6.7 Ferroelectric Hysteresis Measurement

Ferroelectric measurements are done by plotting the charge or polarization that develops (P) across the material against the applied electric field (E). The measurement setup consists of the dielectric material that is to be tested sandwiched between parallel plate electrodes as shown in Figure 2-12a. The Sawyer Tower circuit[20] shown is used to obtain the P-E loop connecting one channel of an oscilloscope to the output of the signal generator and another channel connected to a capacitor or current to voltage converter to read the charge on the material. A typical P-E loop response of a ferroelectric material[21] can be seen in Figure 2-12b. Several reference points can be drawn from the P-E loop which can used to quantify the ferroelectric properties of the material. The two points where the curve crosses the x-axis, denoted $-E_c$ and E_c, define the coercive field or the strength of the field needed to switch the ferroelectric. The two points where the curve crosses the y-axis, denoted $-P_r$ and $+P_r$, are the remnant polarization or the charge that remains in the material when no field is applied. Finally, $-P_{sat}$ and $+P_{sat}$ defines the saturated polarization strength. More information can be obtained by varying the frequency the measurement is done at, the temperature of the device under test, and the overall size (area of electrode, thickness, etc.) of the device.

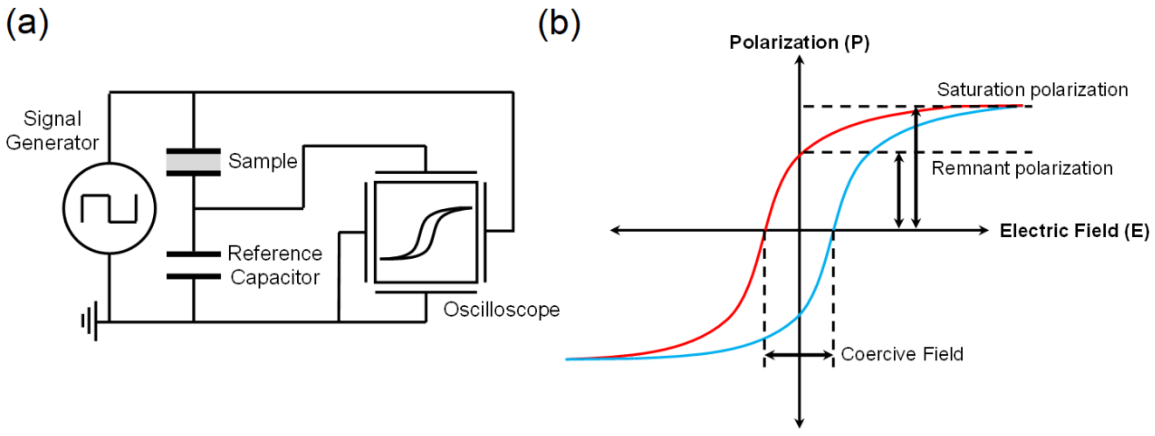

Figure 2-12: Ferroelectric circuit diagram and resulting Polarization – Electric Field hysteresis loop. (a) Classic Sawer-Tower circuit schematic diagram used to measure the quality of a ferroelectric. (b) Polarization – Electric Field loop for a ferroelectric. The curves x-intercepts define the coercive field strength needed to switch the ferroelectric. The y-intercepts determine the remnant polarization (P_r) or the polarization that remains in the sample in the presence of no applied electric field.

To make electrical contact with a device, two methods were employed. Either the raw sample was mounted into a Signatone probe station and manipulator-mounted probe tips were used to connect to the metal pads of the sample, or the sample was bonded into a chip carrier package and wire bonding was used to connect the package's pins to the pads on the sample. Ferroelectric measurements and device switching were carried out using a Precision Multiferroic tester from Radiant Technologies.

2.7 References

1. Moreau, J. M., Michel, C., Gerson, R. & James, W. J. Ferroelectric BiFeO3 X-ray and neutron diffraction study. *J. Phys. Chem. Solids* **32**, 1315–1320 (1971).
2. Royen, P. D. P. & Swars, D. rer. nat. K. Das System Wismutoxyd-Eisenoxyd im Bereich von 0 bis 55 Mol% Eisenoxyd. *Angew. Chemie* **69**, 779–779 (1957).
3. Seshadri, R. & Hill, N. A. Visualizing the role of Bi 6s 'lone pairs' in the off-center distortion in ferromagnetic BiMnO3. *Chem. Mater.* **13**, 2892–2899 (2001).
4. Wang, J. *et al.* Epitaxial BiFeO3 multiferroic thin film heterostructures. *Science* **299**, 1719–1722 (2003).
5. Glazer, A. M. The classification of tilted octahedra in perovskites. *Acta Crystallogr. Sect. B Struct. Crystallogr. Cryst. Chem.* **28**, 3384–3392 (1972).
6. Kiselev, S. V. Detection of magnetic order in ferroelectric BiFeO3 by neutron diffraction. *Sov. Phys.* **7**, 742 (1963).
7. Teague, J. R., Gerson, R. & James, W. J. Dielectric hysteresis in single crystal BiFeO3. *Solid State Commun.* **8**, 1073–1074 (1970).
8. Sosnowska, I., Neumaier, T. P. & Steichele, E. Spiral magnetic ordering in bismuth ferrite. *J. Phys. C Solid State Phys.* **15**, 4835–4846 (1982).
9. Hyub, S. Multifunctional oxide thin films for magnetoelectric and electromechanical applications. (University of Wisconsin - Madison, 2010).
10. Saenrang, W. Deterministic and Robust Room – Temperature Exchange Coupling in Monodomain Multiferroic BiFeO3/Co Heterostructures. (University of Wisconsin - Madison, 2015).
11. M. I. Morozov, N. A. Lomanova, and V. V. G. Specific Features of BiFeO3 Formation in a Mixture of Bismuth(III) and Iron(III) Oxides. *Russ. J. Gen. Chem.* **73**, 1676–1680 (2003).
12. T.T. Carvalho, P. B. T. Synthesis and thermodynamic stability of multiferroic BiFeO3. *Mater. Lett.* **62**, 3984–3986 (2008).
13. Valant, M., Axelsson, A. K. & Alford, N. Peculiarities of a solid-state synthesis of multiferroic polycrystalline BiFeO3. *Chem. Mater.* **19**, 5431–5436 (2007).

14. Eom, C. B. *et al.* I n s i t u grown YBa 2 Cu 3 O 7− d thin films from single-target magnetron sputtering. *Appl. Phys. Lett.* **55**, 595–597 (1989).

15. Brewer, A. *et al.* Uniform sputter deposition of high-quality epitaxial complex oxide thin films. *J. Vac. Sci. Technol. A* **35**, (2017).

16. Lovesey, S. W. & Collins, S. P. *X-ray Scattering and Absorption by Magnetic Materials*. (Clarendon Press, 1996).

17. Gibbs, D. *et al.* Polarization and resonance studies of x-ray magnetic scattering in holmium. *Phys. Rev. B* **43**, 5663–5681 (1991).

18. Anders, S. *et al.* Photoemission electron microscope for the study of magnetic materials. *Rev. Sci. Instrum.* **70**, 3973–3981 (1999).

19. Nakajima, H. *Lectures on Hilbert Schemes of Points on Surfaces*. *Progress in Mathematics* vol. 18 (American Mathematical Society, 1999).

20. Sawyer, C. B. & Tower, C. H. Rochelle salt as a dielectric. *Phys. Rev.* **35**, 269–273 (1930).

21. Stewart, M., Cain, M. G. & Hall, D. A. *Ferroelectric Hysteresis Measurement and Analysis*. (1999).

22. Palai, R. *et al.* β phase and γ-β metal-insulator transition in multiferroic BiFe O3. *Phys. Rev. B - Condens. Matter Mater. Phys.* **77**, 1–11 (2008).

Chapter 3

Antiferromagnetic domain control in $BiFeO_3$ $(111)_{pc}$

3.1 Introduction to $BiFeO_3$ Domains

Magnetic ordering occurs in $BiFeO_3$ below the Néel temperature (T_N) where the magnetic Fe ions order their spins into a long-period magnetic structure (Figure 3-1a). While $BiFeO_3$ has the R3c space group, the magnetic ordering breaks the three-fold symmetry of the rhombohedral unit cell. The long-range order has a periodicity of 62 nm in the bulk and can propagate in one of three crystallographic directions: $\mathbf{k_1}$ = [-110], $\mathbf{k_2}$ = [0-11], or $\mathbf{k_3}$ = [10-1] which are shown in Figure 3-1b. Note that all the propagation directions for the spin cycloid fall in the (111) crystallographic plane and are all orthogonal to the ferroelectric polarization direction [111]. Recent reports have disputed whether $BiFeO_3$ is in fact rhombohedral in bulk or thin film, claiming instead that structurally the three-fold symmetry is also broken and is in fact monoclinic. If this is the case, each propagation direction of the spin cycloid also has a monoclinic distortion making the magnetic domains also structural domains. This could prove to be useful for controlling the population of domains present in as-grown films, if the methods used to select for ferroelastic $BiFeO_3$ variants also work to select for magnetic variants.

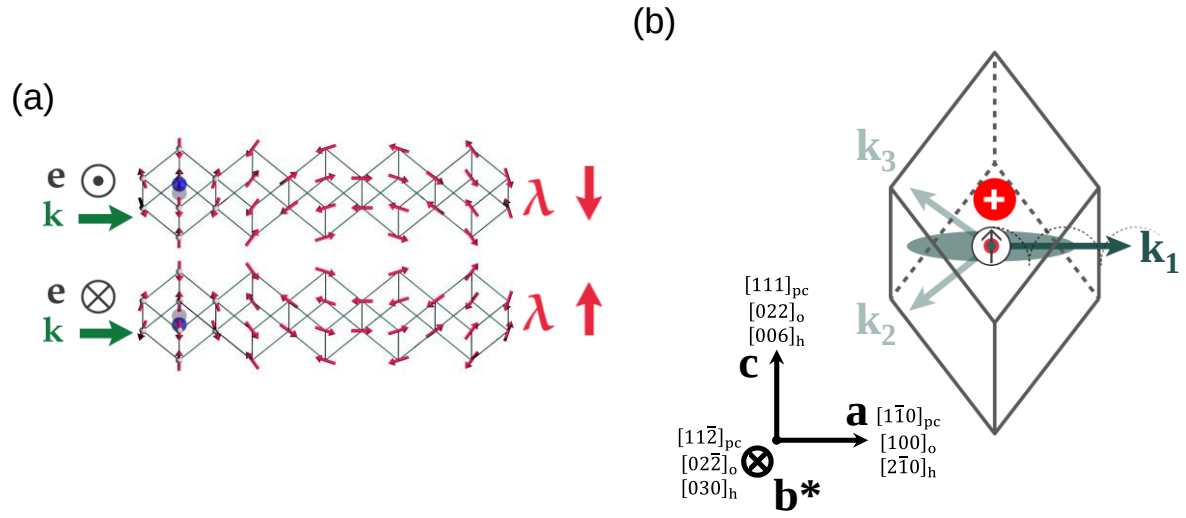

Figure 3-1: AFM spin cycloid configuration in $BiFeO_3$ $(111)_{pc}$. (a) Right-handed (top) and left-handed (bottom) schematics of the AFM spin cycloid present in $BiFeO_3$. (b) A schematic of the $BiFeO_3$ rhombohedral unit cell showing the three allowable propagation vectors ($\mathbf{k_1}$, $\mathbf{k_2}$, and $\mathbf{k_3}$) for the spin cycloid. The crystallographic basis is provided in pseudocubic, orthorhombic, and hexagonal settings.

3.2 A Review of Domain Control in $BiFeO_3$ $(001)_{pc}$ Thin Films

The first reports of $BiFeO_3$ epitaxial thin films had mosaic domain patterns, consisting of four different polarization direction (ferroelastic) domains when deposited on exact $SrTiO_3$ $(001)_{pc}$ substrates[1]. Originally, attempts to control the domain populations was by the use of reduced substrate symmetry[2] by one of two different methods. The first was to not use a cubic substrate and instead use a non-cubic substrate such as orthorhombic $DyScO_3$. Secondly, by purposely choosing a substrate whose surface normal is a few degrees from the intended crystallographic plane, certain domain variants can become more energetically favorable than other variants. Using either of these methods, researchers were able to make $BiFeO_3$ with only two domain variants with stripe-shaped domains instead of a mosaic spread. Later, the miscut method was improved[3] by angling the surface normal a few degrees toward $(110)_{pc}$ instead of $(100)_{pc}$, eliminating another domain variant and leaving a single domain (Figure 3-2). Experimental evidence (Figure 4-8) of the ferroelastic domain populations in the thin film is done using x-ray reciprocal space map (RSM) of the

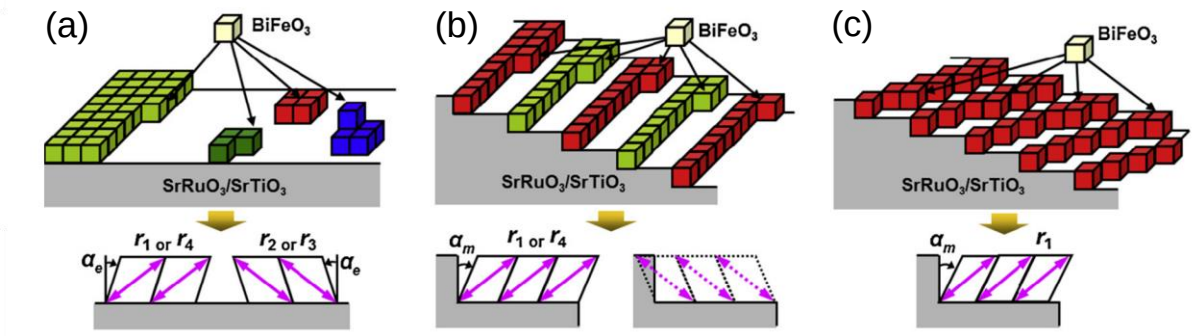

Figure 3-2: Domain control in $BiFeO_3$ $(001)_{pc}$ using miscut substrates. (a) Exact SrTiO3 $(001)_{pc}$ substrates have many nucleation points for $BiFeO_3$ domains to begin growing. These nucleation points have no preference for a particular domain orientation. (b) A high density of low energy nucleation points along the atomic step edge are present on substrates that are miscut from the crystallographic plane. Further, certain domains preferentially form at these edges. When the miscut is toward $(100)_{pc}$, two $BiFeO_3$ domains are preferred while a single domain is preferred (c) when the miscut is toward $(110)_{pc}$. Reproduced and adapted from reference[3] with permission from Current Opinion in Solid State and Materials Science.

(013) Bragg peak and piezoforce microscopy (PFM) of the surface. The $BiFeO_3$ rhombohedral distortion angle of 0.5°, a large separation in reciprocal space between each domain variant is seen in the x-ray RSM. The number of domain variants present can simply be calculated by counting the number of peaks that the $BiFeO_3$ Bragg peak is split into. The population of each variant is related to the peak intensity. Populations of variants can also be calculated by mapping the sizes of the domains imaged using PFM.

By eliminating domain walls from the as-grown thin film, the electric properties of the entire film also improved. The leakage current through the film was four orders of magnitude better than for samples with four domains present[3].

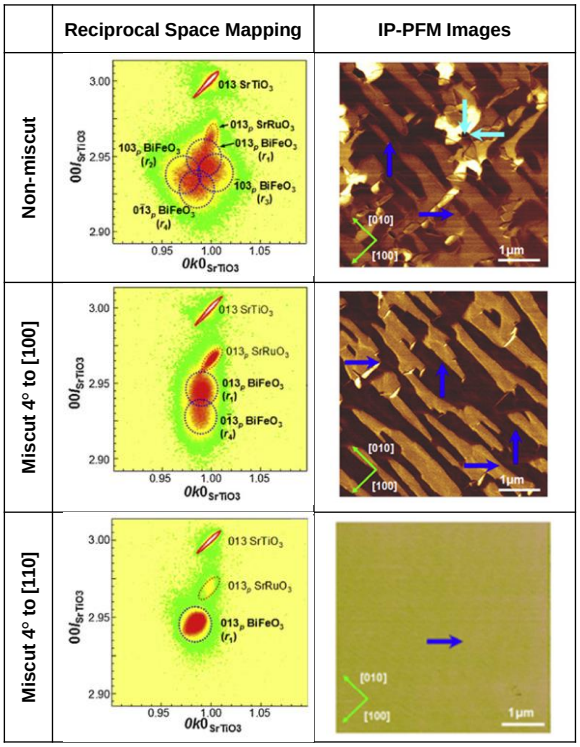

Figure 3-3: Domain populations in $BiFeO_3$ $(001)_{pc}$ with different miscut substrates. Reciprocal space maps (RSM) taken using x-ray diffraction around the $(013)_{pc}$ diffraction condition of the substrate and the thin films. The RSM images show peak splitting of the $BiFeO_3$ peak from the multiple domains present when grown on exact $SrTiO_3$ substrates and substrates highly miscut towards the $(100)_{pc}$ direction. $BiFeO_3$ on $SrTiO_3$ highly miscut towards $(110)_{pc}$ shows a broad peak but no peak splitting. This result is confirmed by the piezoforce microscopy (PFM) images. Contrast in the in-plane PFM scans indicates different domains are present in the film while no contrast suggests domains at least as large as the scan area (~5 μm). Reproduced and adapted from reference[3] with permission from Current Opinion in Solid State and Materials Science.

3.3 Monodomain $BiFeO_3$ $(111)_{pc}$ by Substrate Engineering

Here we apply the concepts learned in the $(001)_{pc}$ system of reducing the substrate symmetry to control the ferroelastic domain populations. While BFO $(111)_{pc}$ deposited on a cubic substrate is already a single ferroelastic domain as-grown, three degenerate antiferromagnetic domains are still present and lie in the plane of the sample. We theorize that the monoclinic structural distortion of the magnetic domain variants can be used to select a specific magnetic variant in the same way the structural distortion of the ferroelastic

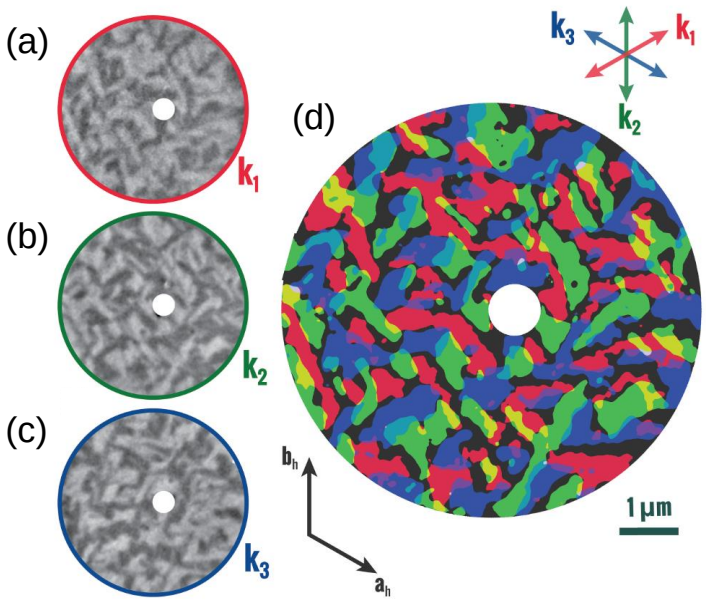

Figure 3-4: XMLD – PEEM vector map of antiferromagnetic domains in $BiFeO_3$ grown on $SrTiO_3$ $(111)_{pc}$. (a-c) PEEM images of the x-ray linear dichroism (XMLD) of the AFM $BiFeO_3$ taken with three different incident x-ray beam directions. The light regions of each direction's image correspond to a propagation vector ($\mathbf{k_1}$, $\mathbf{k_2}$, and $\mathbf{k_3}$). Each propagation direction is assigned a color (red, green, and blue respectively) to construct a vector map of the AFM domain structure. Reproduced and adapted from reference[23] with permission from Physical Review Letters.

domains was used to select for a specific ferroelastic variant. We obtained highly miscut $SrTiO_3$ $(111)_{pc}$ substrates as well as $(111)_{pc}$-orientated non-cubic perovskite substrates, both of which have lower symmetry than the typically-used exact $SrTiO_3$ $(111)_{pc}$ that yields equal populations of the three **k**-domain variants.

3.3.1 Imaging Multidomain $BiFeO_3$ / $SrTiO_3$ $(111)_{pc}$ using XMLD – PEEM

The three **k**-domains present in the $BiFeO_3$ thin films grown on $SrTiO_3$ $(111)_{pc}$ are shown using angle-resolved XMLD – PEEM in Figure 3-4d. The incident x-ray beam was aligned to the in-plane propagation vector of each **k**-domains, Figure 3-4(a-c), with the light regions of each image being the regions of the sample aligned to that specific beam direction. The image contrast comes from the difference in intensity of the Fe L_3 absorption edge when probed with horizontal and vertically polarized x-rays. The intensity of

the vertically polarized x-ray is reduced due to the grazing angle incidence of the beam of 16° and the propagation vectors all in-plane. No contribution from ferroelastic domains is expected as PFM and X-ray RSM of the Bragg peak $(111)_{pc}$ confirm the sample is ferroelectric monodomain. Individual domains are on the sub-micron scale. Additional detail on the XMLD – PEEM setup and the construction of the complete magnetization vector map composited from multiple PEEM images is covered in the next chapter on antiferromagnetic domains in α-Fe_2O_3 thin films.

3.3.2 Substrate Selection

The in-plane strain values for the orthogonal **a** and **b*** directions were calculated for many known non-cubic, stable perovskites particularly in the titanate, ferrite, manganite, gallate, and scandate families. Some of the perovskite materials listed in Figure 3-5 are available commercially as single crystal substrates for research purposes and others could be grown as thick, relaxed buffer layer on a substrate such as $SrTiO_3$. Our first choice for a substrate was the orthorhombic scandate $TbScO_3$. This material was picked due to its small lattice mismatch with $BiFeO_3$ having a small compressive strain of 2.0% along **a** and a small tensile strain of 1.2% along **b***. Having a compressive strain in one orthogonal direction and a tensile strain in the

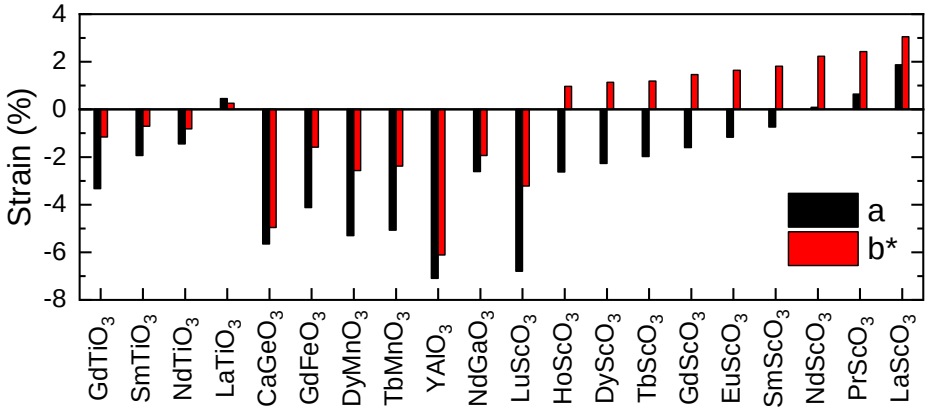

Figure 3-5: In-plane strain percentages between possible substrates and $BiFeO_3$ $(111)_{pc}$. The calculated strain percentages in the **a** and **b*** orthogonal in-plane directions when growing $BiFeO_3$ on a variety of know stable perovskite materials, some of which are commercially available as substrates.

other maximizes the strain anisotropy applied to the $BiFeO_3$ film when it is deposited while the averaged in-plane strain remains small (< 1%).

3.3.3 Characterization of $BiFeO_3$ $(111)_{pc}$ Thin Film

$BiFeO_3$ thin films with thicknesses of 500 nm and 1000 nm were grown using the magnetron sputtering methods outlined in the previous chapter. Five different substrates were used: $SrTiO_3$ $(111)_{pc}$, SrTiO3 $(111)_{pc} \rightarrow (-1-12)_{pc}$, $TbScO_3$ $(011)_o$, $TbScO_3$ $(011)_o \rightarrow (0-11)_{pc}$, and $NdScO_3$ $(011)_o$. All substrates were obtained commercially from CrysTec GmbH Kristalltechnologie in Berlin, Germany. Each substrate was first coated by magnetron sputtering with 30 nm of $SrRuO_3$. The reason to do so is threefold: it acts as a bottom electrode for out-of-plane electrical devices, it selects for the ferroelectric variant of $BiFeO_3$ that has its polarization vector pointed into the $SrRuO_3$ film, and it is a buffer layer that better matches the lattice parameters of $BiFeO_3$ than $SrTiO_3$. Unlike when $SrRuO_3$ is deposited on the $(001)_{pc}$ or $(110)_{pc}$ orientation of a perovskite, $SrRuO_3$ has a 3D growth mode when deposited on a $(111)_{pc}$ perovskite surface as shown in AFM images of the surface of $SrRuO_3$ deposited on each substrate (Figure 3-6). For the samples deposited on highly miscut substrates, the $SrRuO_3$ did not follow a step flow growth mode and thus the step edges were not preserved following the deposition of $SrRuO_3$. This means the high miscut method used to obtain single domain $BiFeO_3$ $(001)_{pc}$ thin films cannot be used to select for certain domains in $(111)_{pc}$ thin films.

The second row of AFM images in Figure 3-6 is that of the $BiFeO_3$ thin film. For comparison, each sample is 500 nm-thick. The AFM images of the $BiFeO_3$ films deposited on exact substrates show roughness values equal to the roughness of the underlying $SrRuO_3$. Distinct atomic layers also appear in the samples on exact substrates. The high miscut samples are entirely different. They have approximately doubled in roughness from the underlying $SrRuO_3$ which was also rougher than the $SrRuO_3$ on exact substrates. The surface morphology of the highly miscut $BiFeO_3$ samples also contain pit-like features whose origin is yet to be resolved.

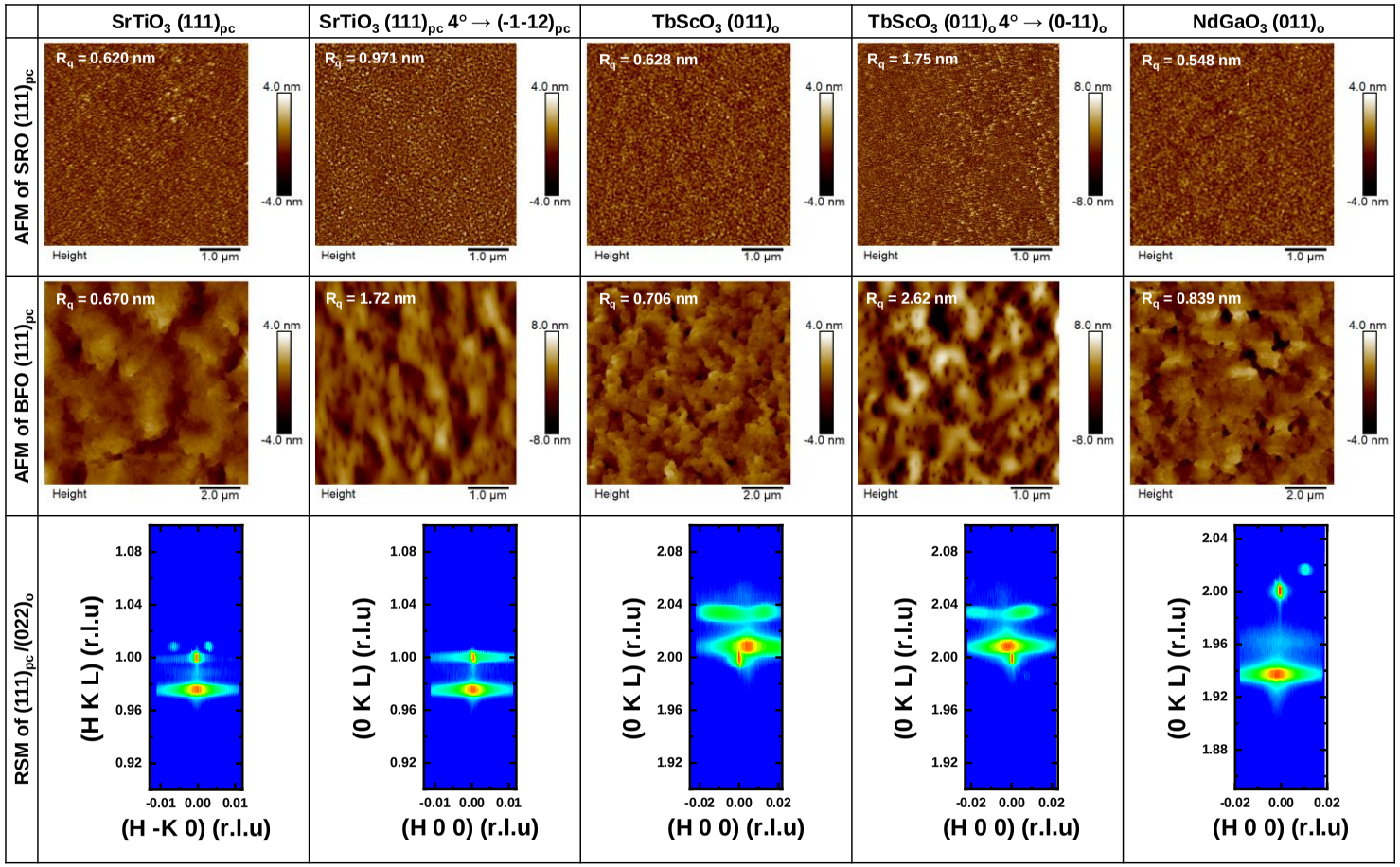

Figure 3-6: Characterization of $BiFeO_3$ $(111)_{pc}$ on different substrates. $BiFeO_3$ $(111)_{pc}$ thin films were grown on $SrRuO_3$ $(111)_{pc}$-buffered substrates with characterization results tabulated from left to right, $SrTiO_3$ $(111)_{pc}$, $SrTiO_3$ $(111)_{pc}$ miscut towards $(-1-12)_{pc}$, $TbScO_3$ $(011)_o$, $TbScO_3$ $(011)_o$ miscut towards $(0-11)_o$, and $NdGaO_3$ $(011)_o$. The atomic force microscopy (AFM) image of the surface topology of the $SrRuO_3$ and $BiFeO_3$ thin films for each is shown as well as the reciprocal space map of the $(111)_{pc}$ / $(022)_o$ Bragg peak.

While all of the x-ray RSM maps of the $(111)_{pc}/(022)_o$ in Figure 3-6 show minority peaks in the $BiFeO_3$ thin film, the degree of minority domains is much greater in the exact and high miscut TSO $(011)_o$ samples. Both samples have two large, bright diffraction peaks belonging to a domain in the $BiFeO_3$ besides the main diffraction peak for $BiFeO_3$.

In Figure 3-7a, the electrical polarization of the $BiFeO_3$ $(111)_{pc}$ thin film deposited on $TbScO_3$ $(011)_o$ is shown. The data was collected using a Signatone Probe Station and a Precision Multiferroic tester from Radiant Technologies. The remnant electrical polarization is above 100 μC cm^{-2} in agreement with what has been reported for the $(111)_{pc}$ direction in $BiFeO_3$. Interestingly, the anisotropic strain from the substrate should stabilize one of the three possible switching pathways possible when switching $BiFeO_3$ polarization vector by 180°. When deposited on a cubic substrate such as $SrTiO_3$ $(111)_{pc}$, the remnant polarization decreases as different parts of the sample switch using different pathways[4,5]. This can potentially cause the polarization vectors of neighboring unit cells that take different pathways to momentarily point their polarization vectors at each other creating a charged head-to-head or tail-to-tail

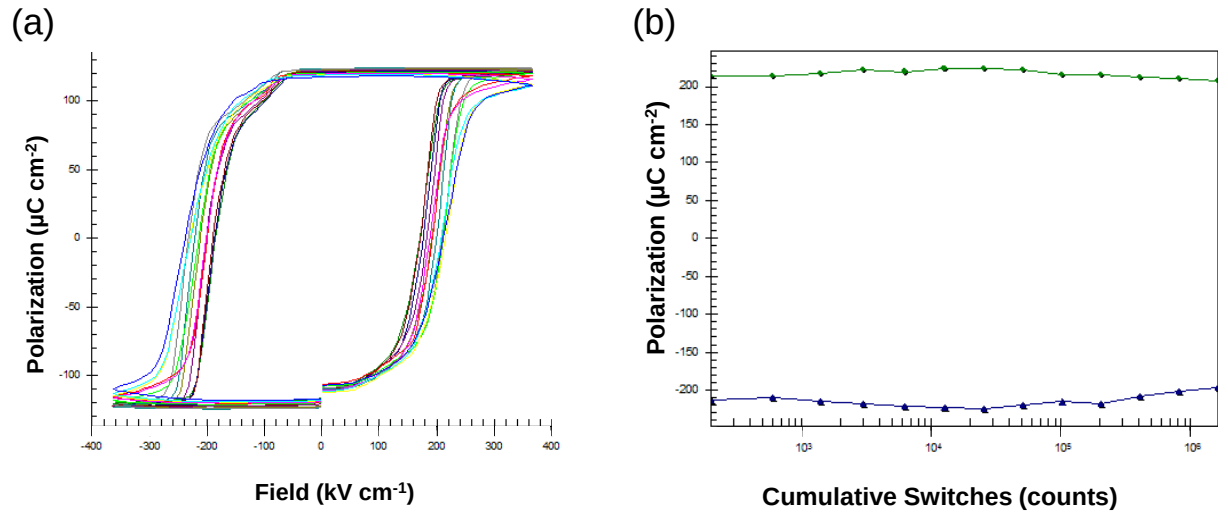

Figure 3-7: Ferroelectric hysteresis loop of BFO $(111)_{pc}$ on $TbScO_3$. (a) The measured out-of-plane ferroelectric response of the $BiFeO_3$ $(111)_{pc}$ thin film grown on $TbScO_3$ $(011)_o$ showing a large remant polarization of greater than 100 μC cm^{-2}, the largest value of any intrinsic ferroelectric material. (b) The remnant polarization is plotted as the sample is repeatedly switched with an applied electric field strength of 300 kV cm^{-1} showing no degradation of the remnant polarization after 10^6 switching cycles.

domain wall, which is a stable configuration, permanently locking the polarization vectors for those unit cells. With only one switching pathway when deposited on $TbScO_3$ $(011)_o$, it would be impossible to form a charged domain wall. The remnant polarization amplitude for $BiFeO_3$ $(111)_{pc}$ is plotted up to 10^6 switching cycles using a 300 kV cm^{-1} electric switching potential and plotted in Figure 3-7b. No degradation of the remnant polarization is observed.

3.4 Measuring Antiferromagnetic Domain Populations

We used diffraction techniques using nonresonant x-rays and neutrons to be able to measure the population of each domain variant in a sample or even a certain region of a sample, such as under an electrically switched pad. While the spatial resolution of the diffraction techniques is insufficient to image the micron-sized domains and is limited to resolving only millimeter sized domains[6], the ability to measure underneath a pad is an advantage over surface sensitive techniques such as X-ray PEEM. The diffraction pattern we expect for a three-fold set of domains is a pair of peaks at positions $\mathbf{N} \pm \mathbf{k_i}$ where $\mathbf{k_i}$ is the spin cycloid propagation vector of the $BiFeO_3$. These peaks originate from the long-ran incommensurate magnetic ordering and are present on all Bragg diffraction peaks. The peaks are normally below the noise level, buried by the much more intense Bragg peak. Perovskites like $BiFeO_3$ have structurally forbidden Bragg peaks at $\mathbf{N} = (0, 0, 3(2n + 1))_h$ due to their symmetry, symmetry that the magnetic ordering doesn't have. Thus peaks such as $(003)_h$ and $(009)_h$ are ideal for looking for magnetic scattering. If all domains are present in the area exposed to the beam, a total of six satellite peaks should be visible. If there is more of one domain in the exposed region than another beam, that peak for the more populous domain will be larger.

3.4.1 Nonresonant X-ray Magnetic Scattering

Experimental beamtime to obtain the magnetic x-ray and neutron diffraction RSM images was led by Noah Waterfield Price and Anuradha Vibhakar with results also reported by them[7]. Synchrotron source nonresonant x-ray magnetic scattering (NXMS) experiments were performed at the Diamond Light Source

using beamline I16[8] which is equipped with a six-circle kappa diffractometer configured in a vertical scattering geometry. The incident x-ray beam was tuned to 4.9 keV which is not in resonance with any of the elements present in the sample. The energy is chosen as a compromise between using higher energy to reduce x-ray absorption from the atmosphere and the Pt top electrode and using lower energy to decrease the amount of multiple scattering processes that can overpower the magnetic scattering signal. The incident x-ray beam is linearly polarized with the E-field component perpendicular to the scattering plane (σ-polarized). Circularly polarized x-rays were obtained using a 100 μm-thick diamond quarter-wave plate. The polarization of the scattered x-rays was determined using a pyrolytic-graphite polarization-analyzer crystal utilizing the (004) reflection. The polarization-analyzer is fixed to the detector arm allowing the analyzer to be positioned such that any linear polarization can be selected for. The azimuthal angle was set to $\phi = 90°$ with respect to $(100)_h$. This was the experimental geometry that minimized multiple scattering. The spot size of the x-ray beam on the sample surface was 50 μm by 90 μm.

3.4.2 Neutron Magnetic Scattering

Neutron magnetic scattering experiments were conducted at ISIS, the UK pulsed Neutron and Muon Spallation Source using the WISH instrument[9]. The sample was orientated such that the $(00l)_h$ zone axis is in backscattering geometry maximizing the resolution of the measurement of the magnetic satellites of the $(003)_h$ forbidden reflection. The spot size of the neutron beam on the sample surface was 20 mm by 20 mm. Data was taken at 10 K and room temperature with the data at 10 K having a better signal-to-noise ratio.

3.4.3 $BiFeO_3$ on TSO $(011)_o$ Substrate

A 1 μm thick $BiFeO_3$ $(111)_{pc}$ thin film was deposited on an exact $TbScO_3$ $(011)_o$ substrate. Figure 3-8(a,b) shows the RSM taken using NXMS of the $(009)_h$ position and neutron scattering of the (003)h position, respectively compared to RSMs shown in Figure 3-8(c,d) taken using identical techniques and of the same diffraction position but for a thin film deposited on an $SrTiO_3$ $(111)_{pc}$ substrate. A single set of satellite peaks for the $\pm\mathbf{k_2}$ domain propagation direction is present in both the NXMS and neutron diffraction data with no peaks from the $\pm\mathbf{k_1}$ and $\pm\mathbf{k_2}$ domain propagation directions, compared with the "triangular"

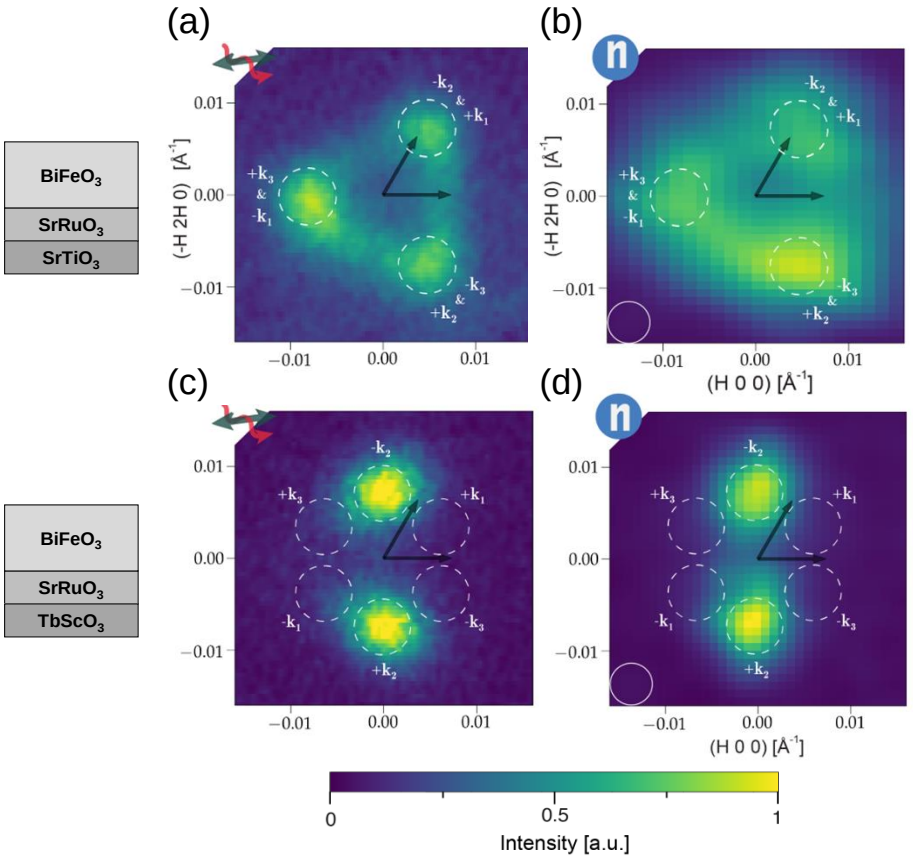

Figure 3-8: Magnetic x-ray and neutron diffraction RSM images of $BiFeO_3$ $(111)_{pc}$ on different substrates. (a-b) RSM images of $BiFeO_3$ grown on $SrTiO_3$ $(111)_{pc}$. (c-d) RSM images of $BiFeO_3$ grown on $TbScO_3$ $(011)_o$. (a,c) The magnetic x-ray RSM images are taken using NXMS with linearly-polarized incident x-rays and show the satellite peaks of the $(009)_h$ position due to the AFM magnetic ordering of the $BiFeO_3$. (b,d) The neutron diffraction RSM images are taken about the $(003)_h$ position. The dashed line circles show the position of possible satellite peaks, and the black arrows indicate the hexagonal reciprocal lattice directions. Measurements are taken at room temperature.

diffraction pattern seen on samples deposited on $SrTiO_3$ $(111)_{pc}$ with satellite peaks from all three domain propagation directions. While the spot size of the NXMS measurements is only 50 μm by 90 μm and could be aligned onto a single large domain, the neutron beam exposes the entire sample, confirming that the entire sample is of a single antiferromagnetic domain.

3.4.4 $BiFeO_3$ on Highly Miscut $SrTiO_3$ $(111)_{pc}$ Substrate

A 1 μm thick $BiFeO_3$ $(111)_{pc}$ thin film was deposited on a $SrTiO_3$ $(111)_{pc}$ substrate that had been miscut by 4° towards the $(-1-12)_{pc}$ direction. Assuming the spin cycloid propagation vectors are the same as observed in the sample deposited on exact $SrTiO_3$ $(111)_{pc}$, the $\mathbf{k_1}$, $\mathbf{k_2}$, and $\mathbf{k_3}$ domains are pointed down the slope of the miscut, perpendicular to the slope of the miscut, and down the slope of the miscut, respectively. Figure 3-9a shows the RSM taken using NXMS of the $(009)_h$ position and Figure 3-9a shows the RSM taken using neutron diffraction of the (003)h position, both on the $BiFeO_3$ deposited on the $SrTiO_3$ $(111)_{pc}$ miscut 4° towards the $(-1-12)_{pc}$ direction. Both NXMS and neutron scattering show that the **k**-domains are still in equal populations, despite the large miscut from the sample surface. Highly miscut substrates seem to have no observable effect on influencing the populations of the monoclinic-distorted magnetic domains.

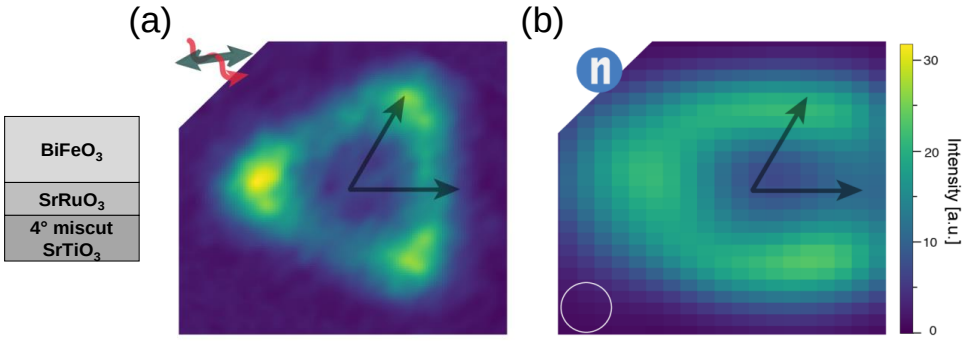

Figure 3-9: Magnetic x-ray and neutron diffraction RSM images of $BiFeO_3$ $(111)_{pc}$ on a highly miscut substrate. (a) RSM of the $(009)_h$ diffraction peak position using NXMS of $BiFeO_3$ grown on 4° miscut $SrTiO_3$ $(111)_{pc}$. (b) Neutron diffraction of the $(003)_h$ diffraction peak position. The diffraction peaks are unchanged from their configuration when growing on non-miscut $SrTiO_3$ $(111)_{pc}$ implying that the $BiFeO_3$ is still three domains.

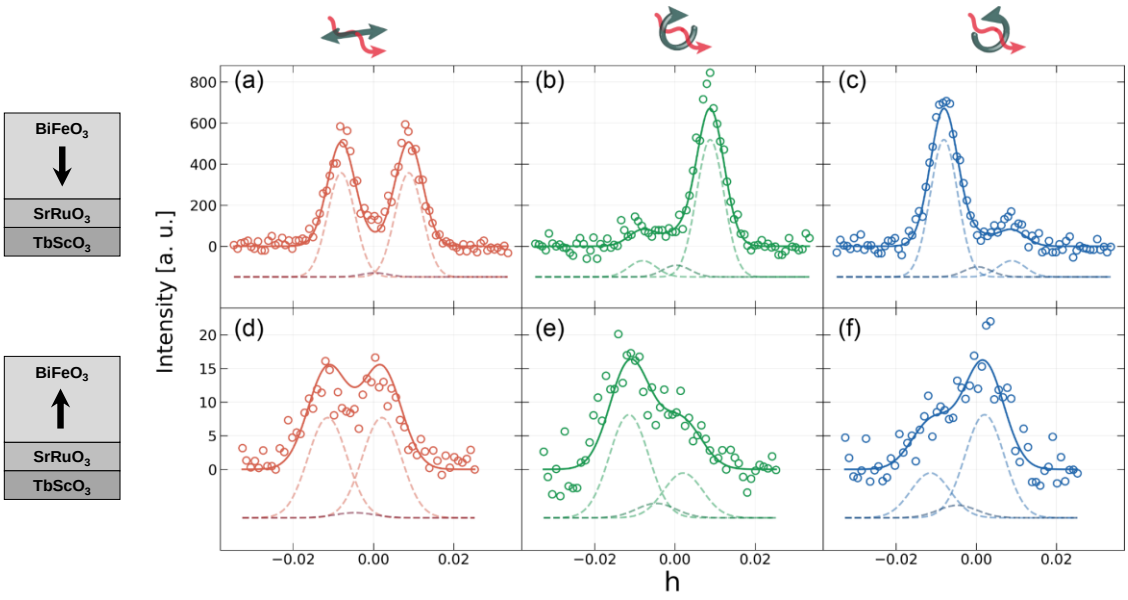

Figure 3-10: Dependence of the NXMS satellite peaks on the polarization of the incident beam. Reciprocal space scans of the $(009)_h \pm k_2$ peaks of the $BiFeO_3$ film grown on $TbScO_3$ $(011)_o$ in the unswitched (a-c) and switched (d-f) states. From left to right is the reciprocal space scans taken with a horizontal linear (red), right-hand circular (green), and left-hand circular (blue) polarized beam. Circles are measured data points with the solid line representing a least-squares fit of the data points.

3.4.5 Electrical Switching of Magnetic Polarity

The advantage of the NXMS technique is the ability to measure a device before and after electrical switching. We hope to be able to get a direct measurement of the change in magnetic ordering caused by ferroelectric switching of the $BiFeO_3$ demonstrating coupling between the ferroelectric and antiferromagnetic orders in $BiFeO_3$. Samples were patterned with top electrodes to make a complete out-of-plane ferroelectric device with the buried $SrRuO_3$ as the other electrode. Using a liftoff method, 10 nm of Pt was deposited by DC magnetron sputtering and patterned into electrodes. Large 200 μm by 500 μm electrodes were used so that the switched area underneath the electrode is much larger than the spatial resolution of the NXMS technique. This allows a spatial map of the magnetic domain populations to resolve the areas of the sample that have been switched, demonstrating voltage control of the magnetic domains[10]. Figure 3-10 shows the clear electric polarization dependence of the NXMS scattered intensity for left and

right circularly polarized x-rays. No change in the scattered intensity of the linearly polarized x-rays due to ferroelectric switching is detected. We calculate that ~79% of the magnetic polarity of the sample on $TbScO_3$ $(011)_o$ switched when the sample was switched from as-grown ferroelectric down state to the ferroelectric up state. Similar calculations performed on the multidomain $SrTiO_3$ $(111)_{pc}$ sample showed a ~93% magnetic polarity reversal upon ferroelectric switching[10]. After switching, a large population of ferroelastic minority domains in the $BiFeO_3$ deposited on $TbScO_3$ $(011)_o$ occurs with less than 50% of the sample still having an entirely out-of-plane polarization vector . This could explain the smaller reported magnetic polarity reversal when ferroelectrically switching the sample.

3.4.6 $BiFeO_3$ on NGO $(011)_o$ Substrate

While the majority domain present in the $BiFeO_3$ thin film on $TbScO_3$ $(011)_o$ was of a single antiferromagnetic **k**-domain and 95% of the sample consisted of the majority domain, after switching only 50% of the film remained in that ferroelastic domain variant. We went back to the drawing board and from Figure 3-5, selected a substrate that has compressive strain in both orthogonal in-plane directions. $NdGaO_3$ is an orthorhombic gallate that is readily available as a substrate, although the $(011)_o$-orientation is usually a custom ordered substrate and not stocked. It has a 2.6% compressive strain along the **a** direction and a

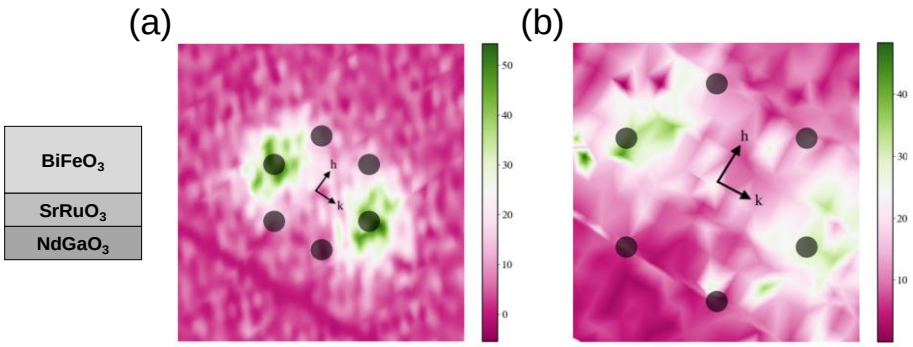

Figure 3-11: Magnetic x-ray RSM images of switched and unswitched $BiFeO_3$ $(111)_{pc}$ on $NdGaO_3$. Reciprocal space maps around the $(009)_h$ reflection using NXMS. Black dots mark the location of expected satellite peaks for a three-domain material. (a) RSM image of an as-grown sample and (b) a sample that is switched 1000 times and then left in the up state.

1.9% compressive strain along the **b*** direction. A 1 μm thick $BiFeO_3$ $(111)_{pc}$ thin film was deposited on an exact $NdGaO_3$ $(011)_o$ substrate. Only an RSM using NXMS of the $(009)_h$ was taken this time which shows a single set of satellite peaks (Figure 3-11a), the same as found in $BiFeO_3$ $(111)_{pc}$ on $TbScO_3$ $(011)_o$. The sample was provided to the beamline with pre-switched 200 μm by 500 μm regions and regions that are as-grown. An identical RSM using NXMS of the $(009)_h$ of a region of the sample switched 1000 times (Figure 3-11b) shows a similar single domain diffraction pattern as seen in the as-grown sample. X-ray diffraction RSM images of the out-of-plane $(006)_h$ Bragg peak of the as-grown and switched sample is shown in Figure 3-12. Unlike the film deposited on $TbScO_3$ $(011)_o$, the film does not break into many ferroelastic domain variants after switching. In fact, only 0.3% of the sample consisted of minority domains as-grown which only increases to 0.9% of the sample after switching. In conclusion, we have obtained a $BiFeO_3$ $(111)_{pc}$ thin

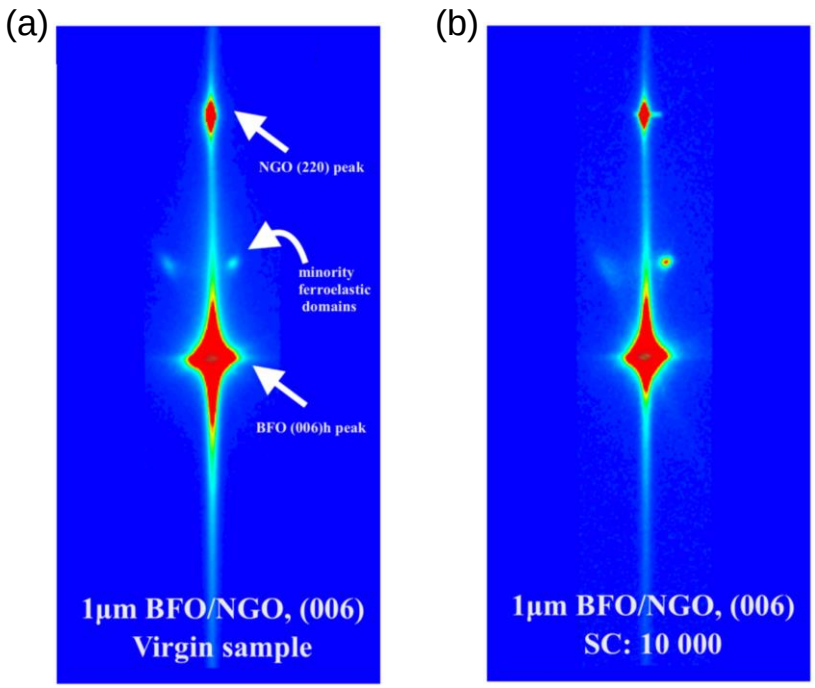

Figure 3-12: X-ray diffraction RSM images of the $(006)_h$ Bragg peak for unswitched and switched $BiFeO_3$ $(111)_{pc}$ on $NdGaO_3$. RSM image of the $BiFeO_3$ $(006)_h$ Bragg peak (a) before switching and (b) after switching 10,000 times showing the $NdGaO_3$ substrate peak, the main BFO peak and peaks from the ferroelastic minority domains in $BiFeO_3$. While minority peaks are still present in the as-grown $BiFeO_3$ and increase after switching, the minority domains make up less than 0.5% of the film compared to 50% in the films grown on $TbScO_3$.

film consisting of a single ferroelectric, ferroelastic, and antiferromagnetic domain that remains stable after thousands of electrical switching cycles.

3.5 Measuring Spin Diffusion Length with ST-FMR

Recently, the spin diffusion length has been measured in prototypical antiferromagnetic materials such as α-Fe_2O_3 and Cr_2O_3 and has been shown to be on the order of microns[11,12] compared to tens of nanometers or nanometers for ferromagnetic[13] and paramagnetic materials[13], respectively. This makes antiferromagnets ideal candidates as spin conductors as part of an antiferromagnet-based spintronic device. We fabricated local geometry devices (Figure 3-13a) with various thicknesses of $BiFeO_3$. The $BiFeO_3$ was inserted as a spacer between the ferromagnet and heavy metal layers of a typical microstrip used in Spin-Torque – Ferromagnetic Resonance (ST-FMR) measurements. We chose Permalloy (Py) for the ferromagnet layer and $SrRuO_3$ for the heavy metal layer as both materials have been used in ST-FMR experiments in our lab before and have been used in conjunction with $BiFeO_3$. To fabricate the device $BiFeO_3$ $(001)_{pc}$/$SrRuO_3$ $(001)_{pc}$ was deposited on a $DyScO_3$ $(110)_o$ substrate. It has previously been reported that $BiFeO_3$ $(001)_{pc}$ on $DyScO_3$ $(110)_o$ will adopt a stripe domain configuration with two alternating domain variants. This substrate and orientation were chosen for a few reasons. While the $BiFeO_3$ is multidomain, only a single domain is present at each location through the thickness of the film. The local device is an out-of-plane device and thus spins traveling through the thickness of the $BiFeO_3$ film and will not encounter any domain walls. For a microwave device $DyScO_3$ is a much more desirable substrate compared to $SrTiO_3$ which has a large dielectric constant at microwave frequencies. Finally, we chose not to use $(111)_{pc}$-orientated $BiFeO_3$ deposited on $TbScO_3$ $(011)_o$ or $NdGaO_3$ $(011)_o$. The uniformity of our $BiFeO_3$ on a $(111)_{pc}$-orientated substrates is highly thickness dependent with 1 μm-thick films having a <1 nm R_q while films less than 400 nm being especially rough. The Py metal overlayer was deposited *in-situ* to prevent contamination from occurring at the interface. Ion milling was used to mill through the Py/$BiFeO_3$/$SrRuO_3$ stack until the substrate is reached creating the microstrip device. A bilayer of Pt/Ti was deposited *ex-situ* to create the

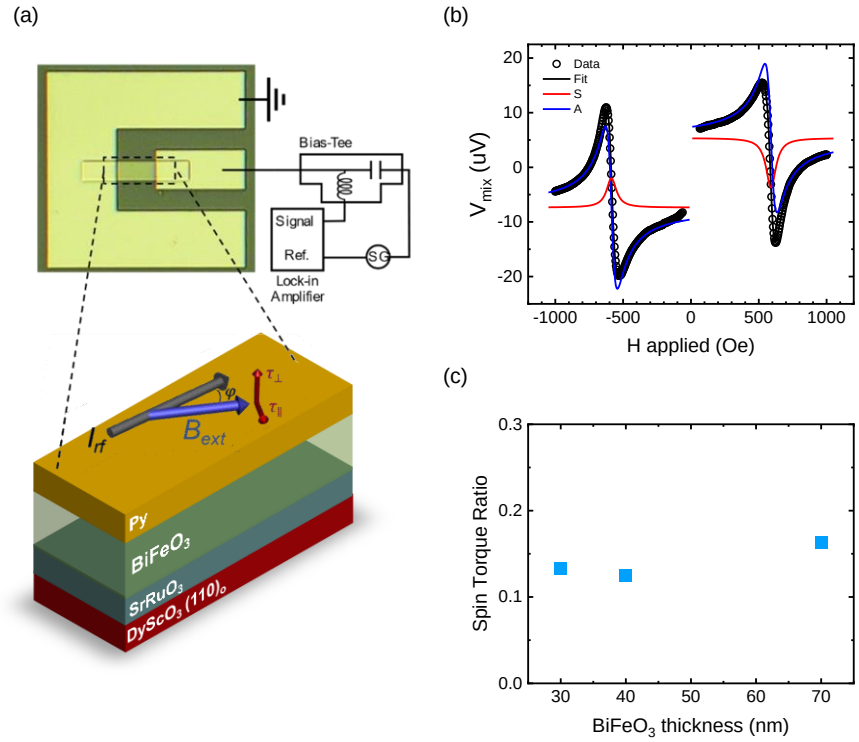

Figure 3-13: Spin-Torque Ferromagnetic Resonance (ST-FMR) setup for measuring the spin conductance of $BiFeO_3$. (a) Top-down image of the fabricated microstrip and a schematic of the ST-FMR measurement. Inset is a schematic of the HM/AFM/FM heterostructure stack of the microstrip. (b) The voltage output at 6000 Mhz from the ST-FMR measurement when the applied magnetic field is varied. The voltage output peak is fit with symmetric and antisymmetric components to get a spin torque ratio. (c) The spin torque ratio for various thicknesses of $BiFeO_3$ spacer layers is plotted.

electrical contacts of the device with Ti helping to adhere the Pt to the sample. All the metallic layers (Py, Ti, and Pt) were deposited using room temperature DC magnetron sputtering. We tested three thicknesses of $BiFeO_3$ (30 nm, 40 nm, and 70 nm). All thicknesses saw spins able to travel through the thickness of the $BiFeO_3$ layer (Figure 3-13b) with all having a similar spin torque ratio (Figure 3-13c). If spins were not conducting, then the Oersted field peak in the external magnetic field dependence of the voltage output would not be visible. The spin torque ratio measured is comparable to the value reported in literature for the HM/FM heterostructure with Py and $SrRuO_3$ thin films[14–16]. This result indicates that the spin diffusion length in $BiFeO_3$, like other antiferromagnetic materials, is much longer than in ferromagnets. The local

device geometry is not suitable for measuring micron-long spin diffusion lengths requiring the deposition of many microns of $BiFeO_3$ followed by ion milling through the many microns of $BiFeO_3$. A nonlocal device geometry is a much more efficient way of measuring the spin diffusion length[17]. Instead of transmission through the antiferromagnet, electrodes are patterned on the surface of the antiferromagnet with varying separation distances. Nanowires of Pt are patterned by electron beam lithography. A current is passed through one of the nanowires which is converted to spins by the spin Hall effect[18]. Additionally, the current caused localized heating, emitting spins by the spin Seebeck effect[19]. The other nanowire acts as an electrode with the heavy metal converting spins to a measurable voltage by the inverse spin hall effect (ISHE)[18]. A nonlocal device was fabricated using a 300 nm-thick monodomain $BiFeO_3$ $(001)_{pc}$ on miscut $SrTiO_3$ $(001)_{pc}$. Our attempts to measure a signal from spin conduction was thwarted by electrical leakage through the $BiFeO_3$ due to our $BiFeO_3$ films not being perfectly insulating. Work is ongoing on a solution to allow our $BiFeO_3$ thin films to be measured using the nonlocal device geometry.

3.6 Monodomain $BiFeO_3$ Spin Transistor Design

Spintronics is a highly active area of research but until recently, spintronic device architectures have focused exclusively on utilizing ferromagnetic materials and not antiferromagnetic materials. Our own

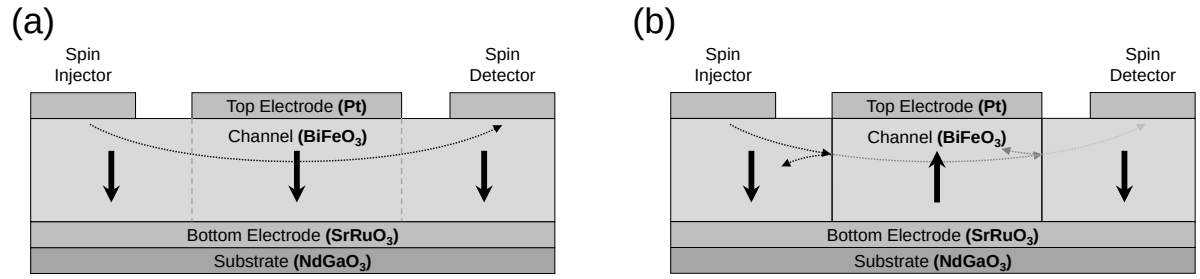

Figure 3-14: Voltage-controlled spin transistor using single domain multiferroic $BiFeO_3$ $(111)_{pc}$. A schematic of a spin transistor designed to utilize the monodomain, spin conductive $BiFeO_3$. A device geometry not unlike that of a planar CMOS transistor is shown where spins are injected into the $BiFeO_3$ which acts as the channel material. If the spins travel freely through the $BiFeO_3$ they are picked up by the spin detector. By ferroelectrically switching the $BiFeO_3$, a set of AFM domain walls is created in the monodomain film which reflect or absorb the spins lowering the spin conductance of the channel.

work with antiferromagnetic $BiFeO_3$ has always focused on coupling the spins in $BiFeO_3$ to a magnetic overlayer to readout the device state[20]. While the most common type of magnetic material that exists and generally considered "interesting but useless" by many in the scientific community, including by Louis Néel himself, antiferromagnetic materials have many benefits over their ferromagnetic counterparts. Antiferromagnets have no net magnetic moment and are thus stable and impervious to external fields, they emit no stray fields so antiferromagnetic devices can scale to much smaller sizes and higher densities, and can operate at terahertz frequencies[21]. We have taken the results from successfully creating completely monodomain $BiFeO_3$ $(111)_{pc}$ and utilized it in the design of an electrically-controlled, ultrafast, low-power, antiferromagnetic insulator-based spin transistor device[22] shown in Figure 3-14. Like all transistors, our device features a source and a drain, with the source acting to inject spins into the $BiFeO_3$ and the drain trying to detect any spins. When the device is in the off state, domain walls in the $BiFeO_3$ between the source and the drain cause it so that spins must pass through the domain walls to reach the detector. In the on-state, the $BiFeO_3$ under the gate is in the same state as the surrounding matrix of $BiFeO_3$ and no interfaces block the path between the source and the gate. Domain walls can cause spins to be reflected or absorbed at the interface.

3.7 References

1. Wang, J. *et al.* Epitaxial BiFeO3 multiferroic thin film heterostructures. *Science* **299**, 1719–1722 (2003).
2. Zavaliche, F. *et al.* Multiferroic BiFeO3 films: domain structure and polarization dynamics. *Phase Transitions* **79**, 991–1017 (2006).
3. Giencke, J. E., Folkman, C. M., Baek, S.-H. & Eom, C.-B. Tailoring the domain structure of epitaxial BiFeO3 thin films. *Curr. Opin. Solid State Mater. Sci.* **18**, 39–45 (2014).
4. Baek, S.-H. *et al.* The Nature of Polarization Fatigue in BiFeO3. *Adv. Mater.* **23**, 1621–1625 (2011).
5. Zou, X. *et al.* Mechanism of Polarization Fatigue in BiFeO3. *ACS Nano* **6**, 8997–9004 (2012).
6. Johnson, R. D. *et al.* X-Ray Imaging and Multiferroic Coupling of Cycloidal Magnetic Domains in Ferroelectric Monodomain BiFeO3. *Phys. Rev. Lett.* **110**, 217206 (2013).

7. Waterfield Price, N. *et al.* Strain Engineering a Multiferroic Monodomain in Thin-Film BiFe O3. *Phys. Rev. Appl.* **11**, 1–8 (2019).

8. Beutier, G., Collins, S. P., Ovchinnikova, E. N., Nisbet, G. & Dmitrienko, V. E. Phase transition of KDP observed by Resonant X-ray Diffraction at forbidden reflections. *J. Phys. Conf. Ser.* **519**, 012006 (2014).

9. Chapon, L. C. *et al.* Wish: The New Powder and Single Crystal Magnetic Diffractometer on the Second Target Station. *Neutron News* **22**, 22–25 (2011).

10. Waterfield Price, N. *et al.* Electrical Switching of Magnetic Polarity in a Multiferroic BiFeO3 Device at Room Temperature. *Phys. Rev. Appl.* **8**, 014033 (2017).

11. Lebrun, R. *et al.* Tunable long-distance spin transport in a crystalline antiferromagnetic iron oxide. *Nature* **561**, 222–225 (2018).

12. Yuan, W. *et al.* Experimental signatures of spin superfluid ground state in canted antiferromagnet Cr2O3via nonlocal spin transport. *Sci. Adv.* **4**, 9–14 (2018).

13. Wang, H., Du, C., Hammel, P. C. & Yang, F. Antiferromagnonic Spin Transport from Y3Fe5O12 into NiO. *Phys. Rev. Lett.* **113**, 097202 (2014).

14. Ou, Y. *et al.* Exceptionally High, Strongly Temperature Dependent, Spin Hall Conductivity of SrRuO3. *Nano Lett.* **19**, 3663–3670 (2019).

15. Zhou, J. *et al.* Modulation of Spin–Orbit Torque from SrRuO 3 by Epitaxial-Strain-Induced Octahedral Rotation. *Adv. Mater.* **33**, 2007114 (2021).

16. Wei, J. *et al.* Enhancement of Spin–Orbit Torque by Strain Engineering in SrRuO3 Films. *Adv. Funct. Mater.* **31**, 2100380 (2021).

17. Cornelissen, L. J., Liu, J., Duine, R. A., Youssef, J. Ben & van Wees, B. J. Long-distance transport of magnon spin information in a magnetic insulator at room temperature. *Nat. Phys.* **11**, 1022–1026 (2015).

18. Sinova, J., Valenzuela, S. O., Wunderlich, J., Back, C. H. & Jungwirth, T. Spin Hall effects. *Rev. Mod. Phys.* **87**, 1213–1260 (2015).

19. Uchida, K. *et al.* Observation of the spin Seebeck effect. *Nature* **455**, 778–781 (2008).

20. Saenrang, W. *et al.* Deterministic and robust room-temperature exchange coupling in monodomain multiferroic BiFeO3 heterostructures. *Nat. Commun.* **8**, (2017).

21. Baierl, S. *et al.* Terahertz-Driven Nonlinear Spin Response of Antiferromagnetic Nickel Oxide. *Phys. Rev. Lett.* **117**, 197201 (2016).

22. Eom, C.-B., Nan, T. & Schad, J. Spin transistors based on voltage-controlled magnon transport in multiferroic antiferromagnets. (2020).

23. Waterfield Price, N. *et al.* Coherent magneto-elastic domains in multiferroic BiFeO3 film. *Phys. Rev. Lett.* **117**, 177601 (2016).

Chapter 4

Antiferromagnetic Spin Textures in α-Fe_2O_3

4.1 Introduction to α-Fe_2O_3

Hematite (α-Fe_2O_3) is an antiferromagnetic insulating (AFI) sesquioxide that has a trigonal corundum crystalline structure ($R\bar{3}c$ space group). In the hexagonal system (α = 120°), α-Fe_2O_3 has the lattice parameters a = 5.038 Å and c = 13.772 Å[1,2]. It is one of two stable crystal structures of Fe_2O_3, the other being γ-Fe_2O_3 which has a cubic spin structure and is ferrimagnetic (FM)[3]. Below the Néel temperature (T_N = 953 K in bulk), α-Fe_2O_3 consists of ferromagnetic sublattices ($\mathbf{M_1}$ and $\mathbf{M_2}$) of Fe^{3+} that alternate in an antiparallel configuration, stacked along the crystallographic c axis (normal to the basal plane). The planes are separated by layers of hexagonal close packed O^{2-} ions. There exists a first order spin reorientation, called the Morin transition, where the Néel vector ($\mathbf{L} \equiv \mathbf{M_1} - \mathbf{M_2}$) reconfigures from an out of plane (OOP) orientation below the transition temperature (Figure 4-1a) to an in plane (IP) orientation above the transition temperature (Figure 4-1b). In bulk, this occurs at $T_M \approx 263$ K[4]. The transition happens due to two competing anisotropies: long range dipolar anisotropy (in-plane) and local single ion crystal field anisotropy (out-of-plane)[5]. The Morin transition temperature can be tuned or in some cases suppressed entirely via chemical doping[4,6,7], thin film thickness[8], or crystallographic orientation[9,10]. Above the Morin transition, a weak spontaneous magnetic moment exists with a strength of roughly ~0.004 μ_B per Fe^{3+}. The weak ferromagnetic signature originates from a small canting of the spins within the basal plane induced by the anisotropic

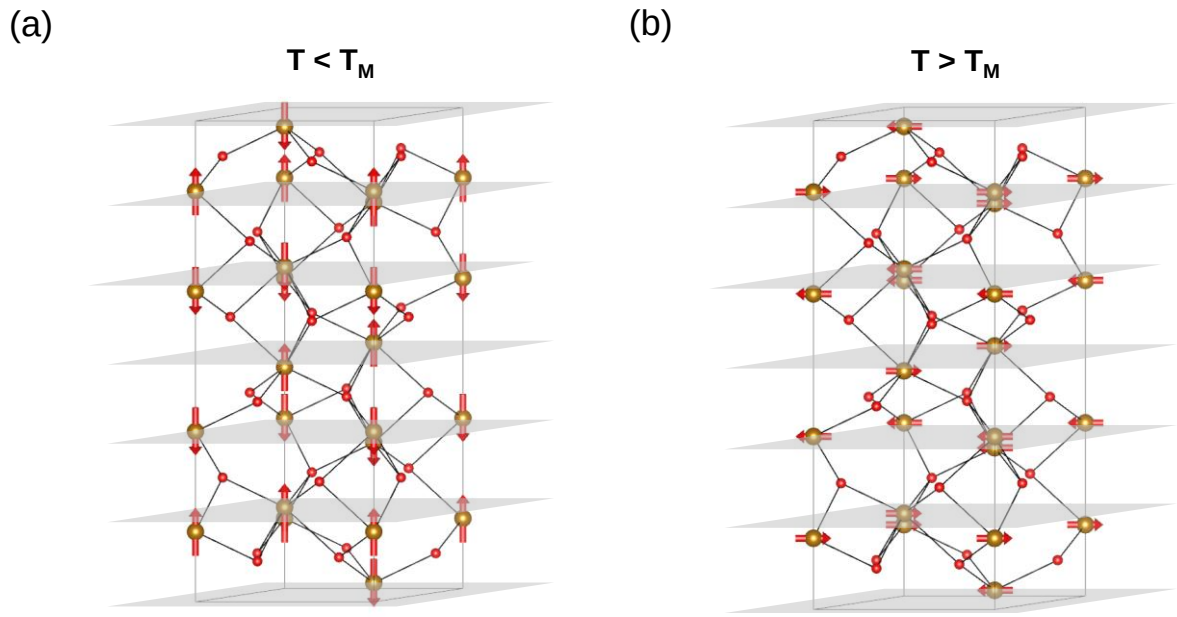

Figure 4-1: The crystal structure of α-Fe_2O_3. Hexagonal unit cell. (a) The out of plane (OOP) orientation of the antiparallel ferromagnetic sublattices that exists when the temperature is below the Morin transition temperature. (b) The in plane (IP) orientation of the antiparallel ferromagnetic sublattices that exists when the temperature is above the Morin transition temperature.

superexchange interaction[11–13]. Like other antiferromagnetic trigonal materials, α-Fe_2O_3 displays three in-plane antiferromagnetic domains (when above T_M) separated by 120° with respect to each other as well as their time inversion equivalents (anti-phase domains) for a total of six unique in-plane domains. The 3-fold rotational symmetry as well as the temporal inversion symmetry is lost in each of these domains making each domain the *C2/c* magnetic space group.

Besides the interest in α-Fe_2O_3 due to its electrochemical properties[14] and its potential use in photocatalysis applications such as water splitting, its interesting magnetic properties make it a promising candidate material for low-dissipation spintronics devices. Recently, there has been a surge of interest in AFI materials for spintronics applications which have several advantages over ferromagnet-based spintronics. With over a century of research, α-Fe_2O_3 is an ideal material for studying AFI-based spintronics.

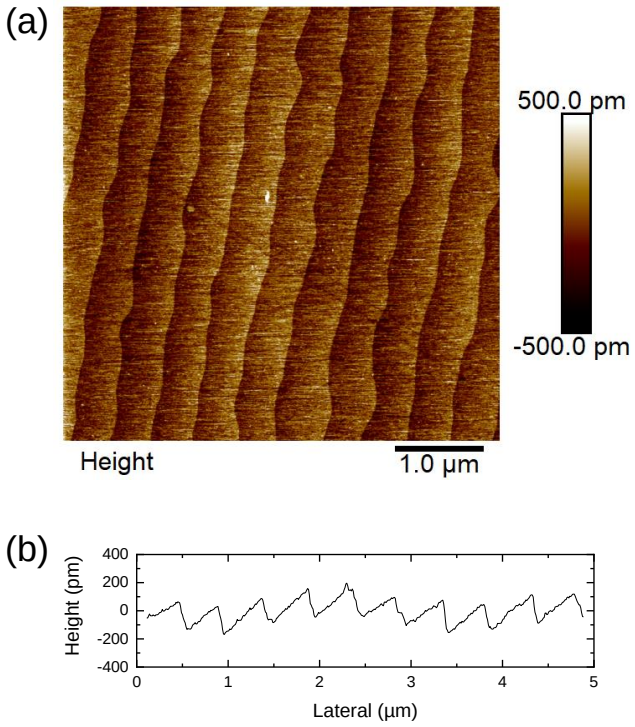

Figure 4-2: Surface of Al_2O_3 substrate. (a) Atomic force microscopy image of the substrate surface after annealing in air at 1050 for 3 hours. (b) Averaged line scan taken perpendicular to the step edge face. The step height is ~215 pm or 1/6 of the *c* lattice parameter of Al_2O_3 which is equal to a single Al - O hcp layer.

4.2 Sample Fabrication

Samples were fabricated on single crystal *c*-plane sapphire, or Al_2O_3 (0001) substrates. Al_2O_3 has the same corundum crystal structure as α-Fe_2O_3 with a 5.3% in plane lattice mismatch. To prepare the substrates to achieve an atomically flat, uniform step terrace structure, the substrate was annealed for 3 hours at 1050°C in air. Atomic force microscopy of the surface (Figure 4-2) shows a step terrace structure with straight step edges. The height of each step corresponds to the thickness of one O – Al – O layer ($1/6^{th}$ of the unit cell). The substrate was attached to a 2.0-inch MeiVac HTR substrate heater and Fe_2O_3 was then deposited using on-axis magnetron sputtering. Two different sputtering methods from literature were evaluated. First, RF

sputtering of a α-Fe_2O_3 target[15] and secondly, reactive RF sputtering of a Fe target[10,16]. Film quality was determined by x-ray diffraction, atomic force microscopy, and SQUID magnetometry.

4.2.1 RF Sputtering

RF sputtering was used to sputter a α-Fe_2O_3 target as it is an electrically insulating material. A stoichiometric ceramic α-Fe_2O_3 target was made using the solid-state synthesis method. To make the target, α-Fe_2O_3 powder (99.9%, Alfa Aesar) was loaded into a 2.125-inch die set and pressed at 5 tons using a Carver 25-ton hydraulic press for 1 minute before slowly releasing the pressure over 5 minutes. The green body target was sintered at 1100°C for 2 hours with a 2°C/min ramp rate. The sintered target was bonded into a copper cup using EPO-TEK H20e silver epoxy. A magnet holds the target to the MeiVac 2-inch spherical MAK magnetron sputtering cathode. The α-Fe_2O_3 thin film was grown by RF sputtering of the target at a power of 50 watts. An atmosphere of 200 mTorr with a 3:2 Ar to O_2 ratio gas mixture was used. The large partial pressure of O_2 was used to prevent the formation of the mixed oxidation phase Fe_3O_4. Fe_2O_3 is the most oxygen-rich solid phase material in the Fe – O binary system so O_2 can be supplied in excess. The sample was held at a temperature of 500°C during the growth and then cooled down in a 300 Torr O_2 atmosphere. The growth rate was 3.0 Å/min.

4.2.2 Reactive Sputtering

Reactive sputtering utilized a metal target in a reactive atmosphere to deposit a compound thin film. The reactive gas species ionizes in the plasma and reacts with the target surface to form the compound material. The compound being deposited (α-Fe_2O_3) is electrically insulating so RF sputtering is still employed to prevent charging of the α-Fe_2O_3 coating that builds up on the sputtering cathode. The constant reversal of the electrical potential used in RF doesn't allow a significant charge to build up and thus electrical arcing doesn't occur. The Fe target was commercially obtained from ACI Alloys with a purity of 99.99%. Due to the large magnetic permeability of pure iron (~ 0.25 H/m), the iron target was thinned to 0.05-inches so that

the magnetic field of the magnetron could adequately pass through the target and confine the plasma. No backing plate or magnet was needed to attach the Fe target to the MeiVac 2-inch spherical MAK magnetron sputtering cathode used. Power was limited to 25 watts due to the high DC bias needed to sustain the plasma. An atmosphere of 10 mTorr with a 3:1 Ar to O_2 ratio gas mixture was used. To ensure that reactive sputtering was occurring, these conditions were chosen by gradually increasing the partial pressure of O_2 in the chamber until a drop in the discharge voltage was observed signaling the change from metal to compound sputtering. The sample was held at the same temperature of 500°C and cooled down in a 300 Torr O_2 atmosphere. The growth rate was 2.5 Å/min.

4.2.3 DC Sputtering of Metal Overlayers

For imaging of the magnetic domains in the α-Fe_2O_3 using PEEM, the α-Fe_2O_3 was either left bare, coated in a non-magnetic metal, or coated in a magnetic metal. Metal overlayers were deposited *ex-situ* by room temperature DC magnetron sputtering. Platinum was used as the non-magnetic metal and deposited by an AJA 1-inch spherical magnetron sputtering cathode at 25 watts and at 3 mTorr of Ar. Cobalt was used as the magnetic metal and deposited at 15 watts and 3 mTorr of Ar and then capped to prevent oxidation using

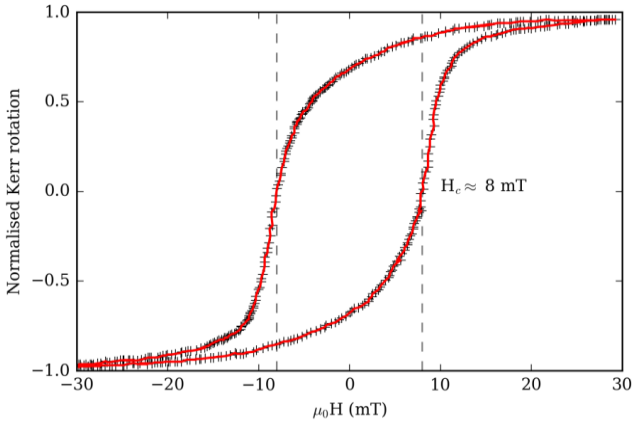

Figure 4-3: Characterization of Co layer. Longitudinal Magneto-Optic Kerr effect magnetometry (L-MOKE) of the α-Fe_2O_3/Co/Al sample used in PEEM experiments. A hysteretic Kerr rotation is observed confirming that the Co layer is ferromagnetic.

aluminum deposited at 40 watts and 5 mTorr of Ar. The aluminum layer self-passivates by forming a layer of Al_2O_3 on the sample surface. A MeiVac 2-inch spherical MAK magnetron sputtering cathode was employed for depositing cobalt and aluminum. To prevent oxidation of the cobalt during deposition, the base pressure of the chamber was at least 1×10^{-8} Torr or lower before sputtering. No external magnetic field was applied to align the magnetic domains when depositing cobalt. All metal overlayers were 1-nm thick so that sufficient signal could be obtained from the underlying α-Fe_2O_3 during PEEM measurements. Thickness was calibrated using x-ray reflectivity. To confirm the 1-nm thick cobalt capped with only 1-nm of aluminum was ferromagnetic, longitudinal magneto-optic Kerr effect magnetometry (L-MOKE) was performed. A hysteretic Kerr rotation was obtained with an 8 mT coercive field which is shown in Figure 4-3. To confirm the MOKE signal came from the cobalt, a bare α-Fe_2O_3 thin film was measured, and no Kerr rotation was observed.

4.3 Thin Film Characterization

The α-Fe_2O_3 thin film was characterized using a variety of methods. The crystalline quality and film thickness was characterized by x-ray diffraction, the surface was characterized by atomic force microscopy, and SQUID magnetometry was used to characterize the magnetic properties.

Using a Bruker D8 Discover diffractometer with a point detector and a $Cu_{K\alpha}$ ($\lambda = 1.5406$ Å) source, X-ray diffraction (XRD) out-of-plane θ-2θ scans centered around the substrate and film (0006) diffraction peak were taken of 30-nm thick α-Fe_2O_3 film grown by RF and reactive sputtering which is shown in Figure 4-4a. The (0006) peak was chosen as it has the highest structure factor for corundum-type materials and therefore the largest peak intensity. The scans were equalized so that the peak intensity of the Al_2O_3 substrate (0006) peak was identical. The RF sputtered thin film shows volume expansion with a *c* lattice parameter of 13.837 Å versus the 13.772 Å bulk lattice parameter. The reactive sputtered thin film has a peak position identical to the bulk value position. The peak intensity of the reactive sputtered thin film has

an intensity 4x greater than that of the RF sputtered thin film. In Figure 4-4b, the θ rocking curve shows a nearly identical FWHM for both RF and reactive sputtered films most likely limited by the layer thickness although the RF sputtered thin film has a slightly higher diffuse background level. The film thickness was determined by x-ray reflectometry as well as the thickness fringing spacing around the film (0006) peaks. In-plane ϕ scans of the {1010} reflections of the substrate and film shows in-plane epitaxial alignment for both the RF and reactive sputtered films.

To analyze the surface topology of the thin film, a Bruker Multimode 8 tapping mode atomic force microscope (AFM) was scanned across a 5μm square area of each sample. Figure 4-5 shows the AFM image obtained for a 30-nm thick α-Fe_2O_3 film grown by RF and reactive sputtering. For both RF sputtering and reactive sputtering, a flat, uniform surface is obtained with a root mean square deviation of 0.350-nm for the RF sputtered film and 0.216-nm for the reactive sputtered film. The absence of the step edges that were present on the surface of the substrate indicate that the thin film grew by island growth (Volmer-Weber) mode for both sputtering methods. This is most likely due to the large lattice mismatch between the thin film and substrate causing the film to grow relaxed and not straining. This means that nucleation sites are much more energetically favorable sites for atoms to bond to than at substrate step edges. Thus, to

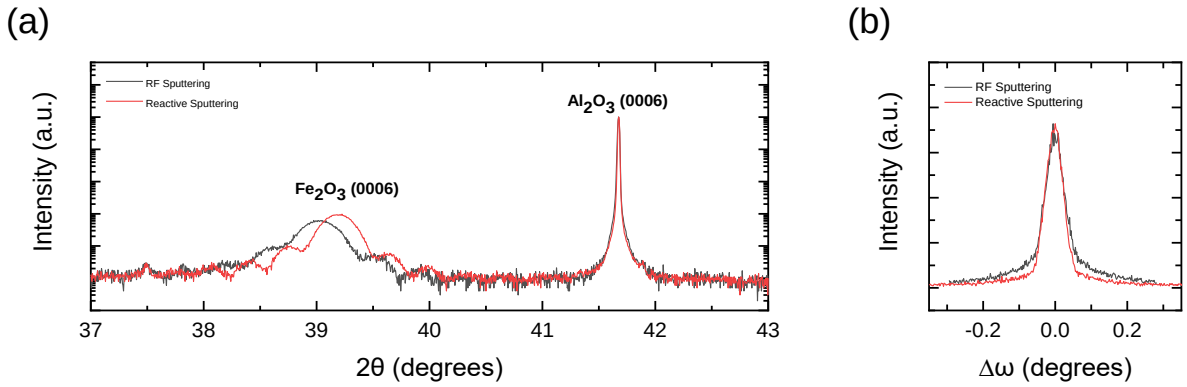

Figure 4-4: X-ray characterization of α-Fe_2O_3 thin film. (a) X-ray out-of-plane θ-2θ patterns of the (0006) peak of the Al_2O_3 substrate and α-Fe_2O_3 thin film for films sputtered by RF sputtering and reactive sputtering. The scans are equalized to the intensity of the substrate peak. (b) Rocking curve scan of the α-Fe_2O_3 thin film peak for films sputtered by RF sputtering and reactive sputtering.

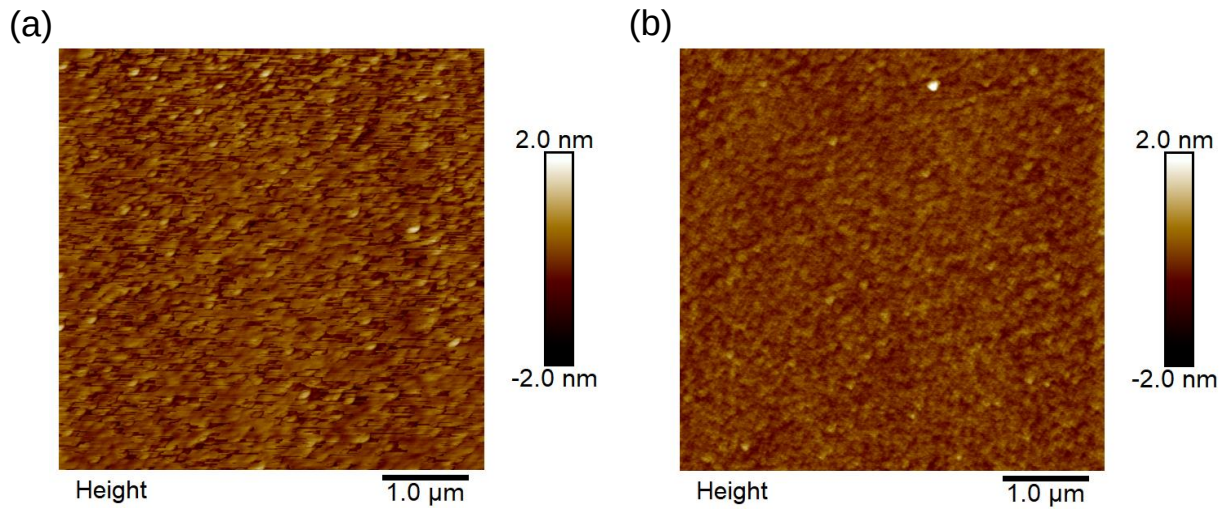

Figure 4-5: Surface of α-Fe_2O_3 thin film. Atomic force microscopy image of the surface of the α-Fe_2O_3 thin film. (a) Surface of α-Fe_2O_3 grown by RF sputtering. (b) Surface of α-Fe_2O_3 grown by reactive sputtering.

simplify sample preparation the substrate annealing step was omitted for most samples, as it did not affect the final film surface topology due to the island growth of the film.

4.3.1 SQUID

There are many different methods of measuring the magnetization of a sample such as MOKE and VSM, but one of the most sensitive is SQUID magnetometry. This is especially important for picking up the weak magnetic moment change that occurs in α-Fe_2O_3 across the Morin transition. A superconducting quantum interference device (SQUID) is a type of magnetometer that is very sensitive to magnetic fields, ideal for measuring the small canted moment present in α-Fe_2O_3 above the Morin transition. It consists of a superconducting ring with two parallel Josephson junctions. A biasing current is passed across the Josephson junctions and the oscillations in the measured voltage are counted. The number of oscillations can be correlated to the change in the magnetic flux through the ring. By passing the sample through the ring, a change in the magnetic flux is observed. The SQUID magnetometer used to measure the α-Fe_2O_3 thin films was a cryogen free Quantum Design MPMS3 EverCool System. Samples were mounted into a

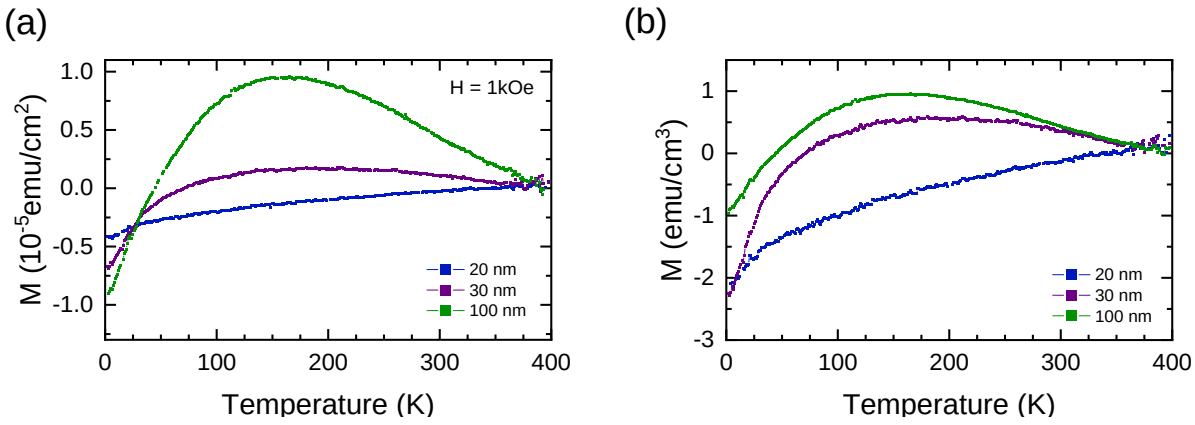

Figure 4-6: Magnetization as a function of temperature for α-Fe_2O_3 grown by RF sputtering. Taken under an applied field of 1 kOe and in ZFC mode. All thickness were zeroed with respect to their magnetization at room temperature. (a) Magnetization for three different thicknesses of α-Fe_2O_3. (b) Magnetization scaled by each film's thickness.

plastic straw which has a low magnetic background signal and then loaded into the system. All measurements were undertaken after cooling the sample down to the minimum measurement with no external magnetic field applied, known as zero-field cooling (ZFC). An applied field strength of 1 kOe was used during all SQUID measurements. Measurements were taken from 2 K to 400 K at 1 K increments. The magnetization was subsequently recorded either as a function of magnetic field or temperature.

First, the magnetization temperature dependence for various film thicknesses was measured with SQUID magnetometry for the film grown by RF sputtering. Three thicknesses were analyzed and plotted in Figure 4-6: 20-nm, 30-nm, and 100-nm. Each thickness was normalized to the magnetization value measured at room temperature. No Morin transition was observed in any film thickness. Instead, a broad peak over the entire temperature range was observed. The intensity of this broad peak increased with increased film thickness. We theorize that this peak is from the Verwey transition (superparamagnetic blocking transition) in magnetite (Fe_3O_4) which is a structural phase transition found at 120 K in bulk material which is accompanied with a change in magnetic moment and electrical conductivity[17,18]. The broadness of this peak can be explained if small regions of secondary phase Fe_3O_4 is present in the film. It

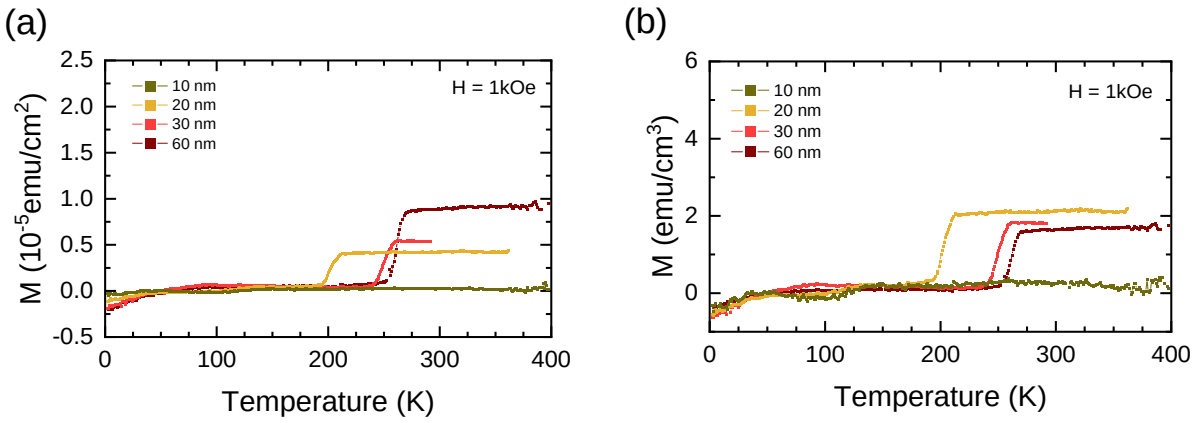

Figure 4-7: Magnetization as a function of temperature for α-Fe_2O_3 grown by reactive sputtering. Taken under an applied field of 1 kOe and in ZFC mode. All thickness were zeroed with respect to their magnetization at 100 K. (a) Magnetization for four different thicknesses of α-Fe_2O_3. (b) Magnetization scaled by each film's thickness.

has been shown that the Verwey transition temperature (T_B) is dependent on crystalline particle size[19,20]. If the secondary phase regions are of various sizes, various regions will go through the transition at varying temperatures leading to the broad transition when analyzing the entire film. This result highlights the sensitivity that SQUID magnetometry can provide on the quantity of impurities present in the α-Fe_2O_3 film. The α-Fe_2O_3 phase is the only crystalline phase in the Fe – O binary system that is antiferromagnetic with α-Fe, Fe_3O_4, γ-Fe_2O_3 all being ferromagnetic and thus much larger magnetic moments. The magnetization of any present small impurities of these FM phases in the α-Fe_2O_3 will overpower the intrinsic small magnetization of the canted moment in α-Fe_2O_3. In the RF sputtered films, no Fe_3O_4 peaks in the x-ray diffraction out-of-plane scan are present meaning the Fe_3O_4 regions of the film are either of poor crystalline quality, or the amount of impurity phase present was insufficient to cause a diffraction peak with an intensity above the background noise floor. SQUID is insusceptible to the crystalline quality of the secondary phase regions making it a better tool for determining phase purity in α-Fe_2O_3 films. In conclusion, we have found that a small minority population of mixed oxidation state Fe_3O_4 is present in our RF sputtered films which

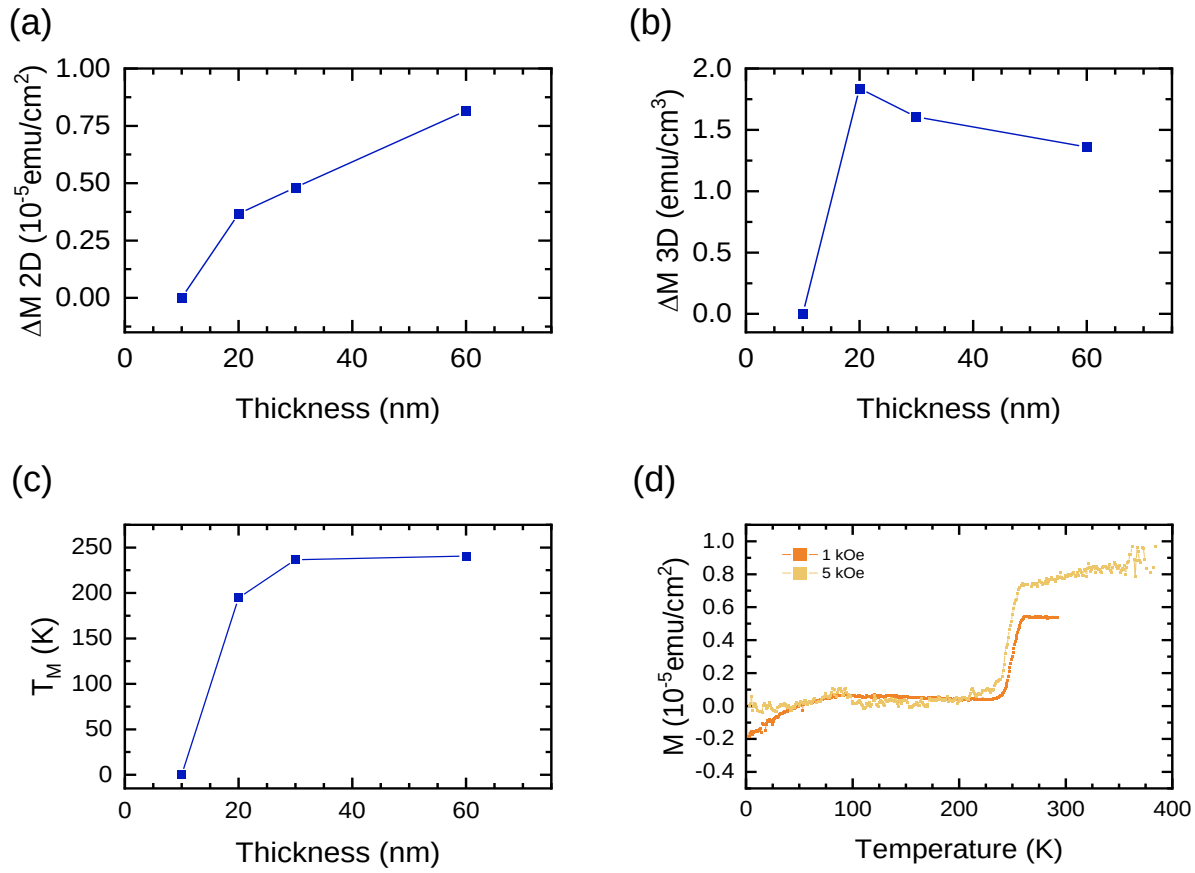

Figure 4-8: Morin transition properties of reactive sputtered α-Fe_2O_3. Magnetization as a function of film thickness with 2D scaling (a) and 3D scaling (b). (c) The dependence of the Morin transition temperature on film thickness. (d) Magnetization versus temperature for the 30-nm thick film at different external magnetic field strengths.

saturates the magnetization of the sample so that the magnetic properties of the majority α-Fe_2O_3 cannot be observed.

Next, we measured the magnetization versus temperature of the reactive sputtered thin films. Four thicknesses were analyzed this time and plotted in Figure 4-7: 10-nm, 20-nm, 30-nm, and 60-nm. Each thickness was normalized to the magnetization value measured at 100 K. A Morin transition is clearly visible in all samples, except for the thinnest 10-nm thick film. In Figure 4-8a,b the amplitude of the magnetization above the Morin transition is plotted as a function of the film thickness with both 2D scaling

(a) and 3D scaling (b). The 3D scaled magnetization is relatively constant with thickness. The 10-nm thick sample is shown here to have no magnetization over the entire temperature range measured but without a Morin transition, no change in magnetization is present. In actuality, the 10-nm film has a similar magnetization as the other samples all the way down to 2K. Some degradation of the magnetization with increasing thickness is observed possibly due to thicker samples having lesser crystalline quality, observed by increasing rocking curve width for thicker films. For the thickest of the films measured, 60-nm, the Morin transition temperature (T_M) occurs at close to the bulk value. As the thickness of the film decreases, T_M is suppressed as shown in Figure 4-8c. We report a ferromagnetic signature in our 10-nm films down to 2 K, the minimum temperature limit of our SQUID magnetometer. This trend agrees with recently published experiments on both α-Fe_2O_3 nanoparticles[13,21–24] and thin films[8]. Recent experiments have shown α-Fe_2O_3 particles of ~20 nm to have ferromagnetic ordering down to as low as 5 K. This effect is similar to the decreasing temperature of the Verwey transition in Fe_3O_4 with decreasing particle size. In Figure 4-8d, the magnetization of the 30-nm thick film is plotted at two different external magnetic field strengths: 1 kOe and 5 kOe. At the low temperature region below the Morin transition, the magnetization seems to increase with field strength while the opposite is true for the high temperature region.

4.4 Magnetic Domain Imaging of α-Fe_2O_3/Co

We imaged the microscopic, real-space magnetic domain morphology of each of the magnetic layers in the α-Fe_2O_3/Co/Al heterostructure using vector-mapped x-ray photoemission microscopy (X-ray PEEM)[25,26]. X-ray PEEM is ideal due to the ability to selective probe antiferromagnetic and ferromagnetic domains, both of which are present in the heterostructure, so that how they influence each other can be deduced. The samples used were 10-nm thick α-Fe_2O_3 coated with 1-nm thick Co and 1-nm thick Al. A complex pattern of vortices of antiferromagnetic domains was observed in the α-Fe_2O_3 film. Furthermore, the pattern of domains imprints through exchange proximity to the Co overlayer yielding a similar domain pattern in the ferromagnet.

4.4.1 Magnetic Domain Imaging Techniques

A significant number of methods for imaging of real-space magnetic ordering exist have been demonstrated that may be useful for measuring the magnetic Co and α-Fe_2O_3 thin film layers including optical, electron, scanning probe, and x-ray microscopies. Magnetic force microscopy (MFM), a specialized type of atomic force microscopy can be used to image the real-space magnetic domain structure in ferromagnets. MFM utilizes a magnetized tip which is deflected by stray fields present at the surface of a ferromagnet to construct an image of the magnetic order[27–29]. Quantifying the magnetization can be difficult as deflection of the tip is not only dependent on the magnetization of the material under measurement but also the tip magnetization and the distance between the surface and the tip. MFM benefits from a relatively high spatial resolution, as good as 10-nm.

Magneto-optical effects such as the Kerr effect can also be harnesses for imaging of magnetic materials in magneto-optical Kerr effect microscopy (MOKE)[30,31]. The Kerr effect is when polarized light reflected from a magnetic material is rotated by a small amount relative to the strength of the overall magnetic field. While easy to setup experimentally and the temporal resolution is in the femtosecond range[32], the spatial resolution is much more limited for MOKE than MFM. Being an optical technique, the resolution is limited by diffraction of the laser light used, with a maximum resolution of 100-μm.

Lorentz microscopy can be used to image the magnetization of thin cross-sections of material using a transmission electron microscope (TEM)[33]. The Lorentz force causes deflection of electrons transmitted through a magnetic material. The technique has a high spatial resolution similar to MFM, but rather than a surface sensitive technique, the signal detected is an average of the magnetization over the entire thickness of the cross-section. Preparation of a thinned cross-section also necessitates destruction of the sample to obtain a measurement.

X-ray microscopy relies on the x-ray magnetic dichroism effect and an energy tunable synchrotron x-ray source to produce an image of the ferromagnetic (XMCD) magnetization[34,35]. The dichroism effect is maximized when an electron is excited to a magnetically polarized band. The energy of the x-ray beam is tuned to the absorption edge of the magnetic ion being probed making x-ray microscopy uniquely elementally sensitive. The elemental sensitivity permits different magnetic layers of a heterostructure to be individually imaged if they consist of disparate magnetic ions.

While the techniques discussed thus far are useful for imaging of ferromagnetic materials, relying either on the bulk magnetization or stray fields, all are insensitive to antiferromagnet domains having weak or zero net magnetization or stray field. A magnetometer with a much higher sensitivity than what is achievable with MOKE, Lorentz, XMCD, or a magnetized probe is needed. We have already seen that a SQUID is sensitive enough to read the magnetization of an antiferromagnetic material can be rasterized across a surface to produce an image. Scanning SQUID, while having a relatively poor spatial resolution of around 10-μm, can image large domains of an antiferromagnet[36]. Progress has been made recently in implementing a nitrogen-vacancy magnetometer into a scanning probe tip and has been used to image antiferromagnetic materials such as $BiFeO_3$[37] as well as α-Fe_2O_3[38,39]. The most widely utilized antiferromagnetic order probe is x-ray magnetic linear dichroism (XMLD) PEEM. Whereas XMCD is relative to the average magnetization of the material, XMLD is relative to the square and can be used to measure compensated magnetic materials. X-ray microscopy images give a contrasting image dependent on the magnetization of each region measured but further work is needed to obtain the magnetization vector. We have developed a technique to not only map the magnetization vector of ferromagnets using XMCD but also to map the spin direction of antiferromagnets using XMLD.

We selected X-ray microscopy (XMCD and XMLD) for this study of the α-Fe_2O_3/Co system. It's combination of high spatial resolution able to image sub-micron domains, ability to image ferromagnetic and antiferromagnetic type magnetic orders, and elemental selectivity to measure multiple layers in a

heterostructure make it the clear choice to study this system. While XMLD – PEEM has been used previously to measure the domain structure in α-Fe_2O_3 thin films grown by MBE and bulk single crystals[40], no study has used the XMLD anisotropy present when images are taken at different incident beam angles to reconstruct the complete vector map of the antiferromagnetic spin direction, which we present here.

4.4.2 X-ray PEEM

X-ray PEEM measurements were performed and reported[25] on by Francis Chmiel, Noah Waterfield Price, Roger Johnson, and Anne Lamirand using beamline I06 at the Diamond Light Source in Didcot, United Kingdom. Beamline I06 (Nanoscience Beamline) delivers circularly or linearly polarized soft x-rays (80-2100 eV) for XMCD and XMLD PEEM experiments[41]. The sample was mounted into the UHV vacuum chamber of the PEEM tool and its surface was grounded by connecting the top metallic layers (Co/Al or Pt) to the instrument's ground. The sample translation stage can rotate the sample in a 180° range about the sample surface normal direction. The incident x-ray beam illuminates the sample at a grazing incidence angle of 16° from the sample surface plane. Photoemission from the sample is collected using an Elimitec SPELEEM-III microscope. Images were taken with different beam polarizations and an image asymmetry (dichroism) is calculated using Equation (4-1). Magnetic order sensitivity is obtained either using XMCD

$$\delta = \frac{I_1 - I_2}{I_1 + I_2} \; where \; I_i \; is \; the \; image \; intensity \tag{4-1}$$

for ferromagnetic domains or XMLD for antiferromagnetic domains. Signal from XMLD is significantly weaker than the signal from XMCD and thus the scan times were longer. Generally, collection times of 3600 seconds was used for XMLD and 300 seconds was used for XMCD. Collection counts were binned every 10 seconds and processed together to eliminate issues caused by the drifting of the sample and x-ray

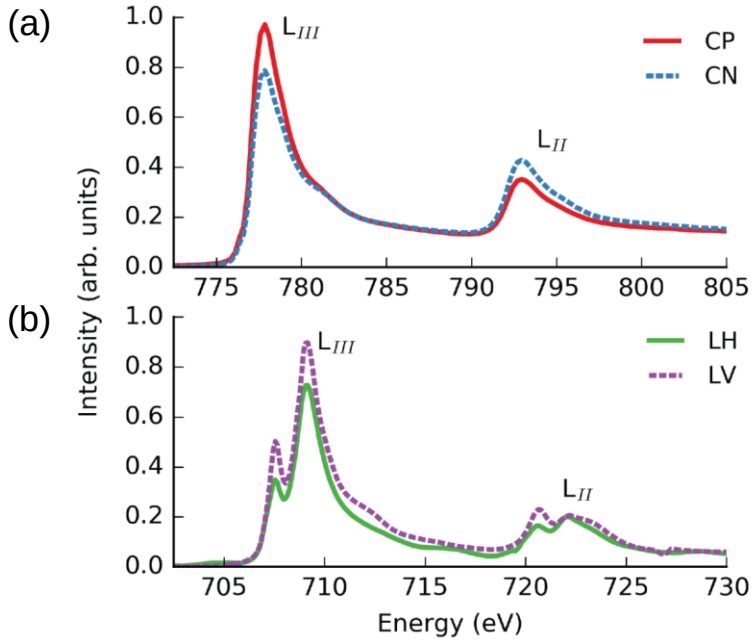

Figure 4-9: XAS of the Co and Fe $L_{2,3}$ edges of the α-Fe_2O_3/Co sample. X-ray absorption spectra at Co (a) and Fe (b) $L_{2,3}$ edges of a roughly 20-μm diameter area. Spectra is taken using circularly positive (red line) and negative (blue dashed line) polarized light for the Co edge and linearly horizontal (green line) and vertical (purple dashed line) polarized light for the Fe edge.

beam positions that occurs over a long collection time. Images were smoothed using a convolution of a 2D gaussian. A fourth order polynomial was used to flatten the image and subtract the background.

4.4.3 Constructing Vector Maps

Prior to imaging, the photoemission intensity from the entire region (20-μm in diameter) was taken. The total photoemission is proportional to the absorbed photons making this method an indirect measurement of the x-ray absorption spectra (XAS). Figure 4-9 shows the result of this measurement covering the energy range around the $L_{2,3}$ absorption edges of both Co and Fe. From Figure 4-9a we can immediately tell that the Co present in the heterostructure in the 1-nm overlayer is metallic in nature and not oxidized due to the absence of any additional structure around the L_3 and L_2 edges[42]. Circular light dichroism is also present at the Co edges confirming the presence of the XMCD effect in the Co which would imply that it is

ferromagnetic. Figure 4-9b covers the Fe L_3 and L_2 edges with signal originating from the F^{3+} magnetic ions present in the α-Fe_2O_3 layer. Peak splitting of each absorption edge is present from the crystal field effect of the metal compound. The shape of the spectra matches well with what is expected for an octahedrally coordinated Fe site, as expected for and not tetrahedral or metallic coordination that might be present in Fe_3O_4 or α-Fe[42]. While not shown here, no dichroism in the x-ray photoabsorption at the Fe edges was seen for circularly polarized light. This is consistent with antiferromagnetism and no XMCD effect in the α-Fe_2O_3 layer.

Vector maps of the ferromagnetic Co layer (Figure 4-10c) were constructed using PEEM images obtained using X-ray circular asymmetry, δ, at two orthogonal incident beam directions (Figure 4-10a,b) and using the anisotropy present in the images due to the XMCD effect[43,44]. First, two incident beam

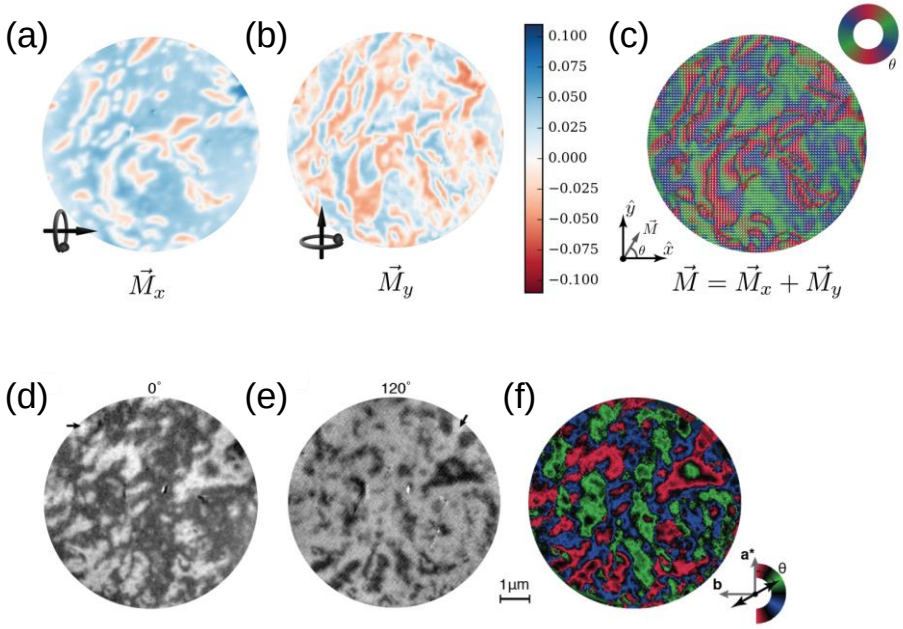

Figure 4-10: Construction of Co XMCD and Fe XMLD vector maps. (a,b) XMCD map of Co taken at two perpendicular incident x-ray directions denoted by the black arrows, at 0° and 90° with respect to the $\hat{x}$ axis. (c) Constructed vector map of the Co magnetization with color representing the phase angle. The diameter of the image is 10-μm. (a,b) XMLD map of Fe taken at two incident x-ray directions 120° apart denoted by the black arrows. (c) Constructed vector map of the α-Fe_2O_3 magnetization with color representing the phase angle. XMLD maps are taken of sample after application of an external magnetic field.

energies were chosen and PEEM images were taken at each energy. The first, the maxima at the Co L_3 edge, E_1 = 777 eV, and second the pre-edge value, E_2 = 770 eV. The image taken at the pre-edge value E_2 was used to normalize the image taken at the position sensitive to the magnetic order, E_1. This technique can eliminate contrast from differences in polarization channels or drifting of the x-ray beam. This method is used to generate an image using x-rays with positive chirality and negative chirality and the two images are then combined using Equation 5-1 to get the actual XMCD image. Finally, the local magnetization vector $\langle\vec{M}\rangle$ is generated by taking the XMCD signal (δ_0 and $\delta_{\frac{\pi}{2}}$) at two incident x-ray directions (parallel to orthogonal unit vector directions $\hat{x}$ and $\hat{y}$) and combining them using Equation (4-2). In summary, a PEEM image is

$$\langle\vec{M}\rangle \propto \delta_0\hat{x} + \delta_{\frac{\pi}{2}}\hat{y} \tag{4-2}$$

taken at two beam energies, two polarizations, and at two incident light directions to generate the complete magnetization vector map of a ferromagnet using XMCD.

To construct the vector map of the antiferromagnetic α-Fe_2O_3 layer (Figure 4-10f), XMLD effect was used to get contrast from the antiferromagnetic spin directions. Like with the XMCD image, two incident beam energies were chosen and PEEM images were taken at each energy. This time, the maxima at the Fe L_3 edge, E_1 = 708 eV was used as the magnetic order sensitive energy, and pre-edge value, E_2 = 700 eV was used to normalize the image. All PEEM measurements were taken at room temperature and above the Morin transition meaning that the spins in the α-Fe_2O_3 layer are all in-plane. Horizontally polarized x-rays will be sensitive to magnetism due to the XMLD effect, but vertically polarized x-rays will not. The dichroic asymmetry dependence on incident x-ray beam angle and antiferromagnetic spin direction is defined by Equation (4-3). By taking an XMLD image and recording the dichroism at many different incident (for this

$$\delta_{XMLD} = A + B(3\cos^2(\theta) - 1)\langle\vec{M}^2\rangle \tag{4-3}$$

experiment, we took six) x-ray beam directions, we can extract the antiferromagnetic spin direction of the film. XMLD images taken at two angles 120° is shown in Figure 4-10d,e. Darker regions represent regions where the spin direction is parallel to the incident x-ray beam while lighter regions represent regions where the spin direction is perpendicular to the incident x-ray beam. The intensity of each pixel (10-nm × 10-nm) of the XMLD image was plotted with respect to the incident beam angle as shown in Figure 4-11d. Green, red, and blue false coloring was assigned to the three different in-plan spin directions allowed by the *C2/c* crystalline symmetry. The assignments are such that (R || [210], B || [120] and G || [$\bar{2}$10]). Black was used for phase angles between each of the colors. By iterating through each pixel and determining its in-plane phase with respect to the incident x-ray beam, a false color vector map can be built up (Figure 4-11a). While

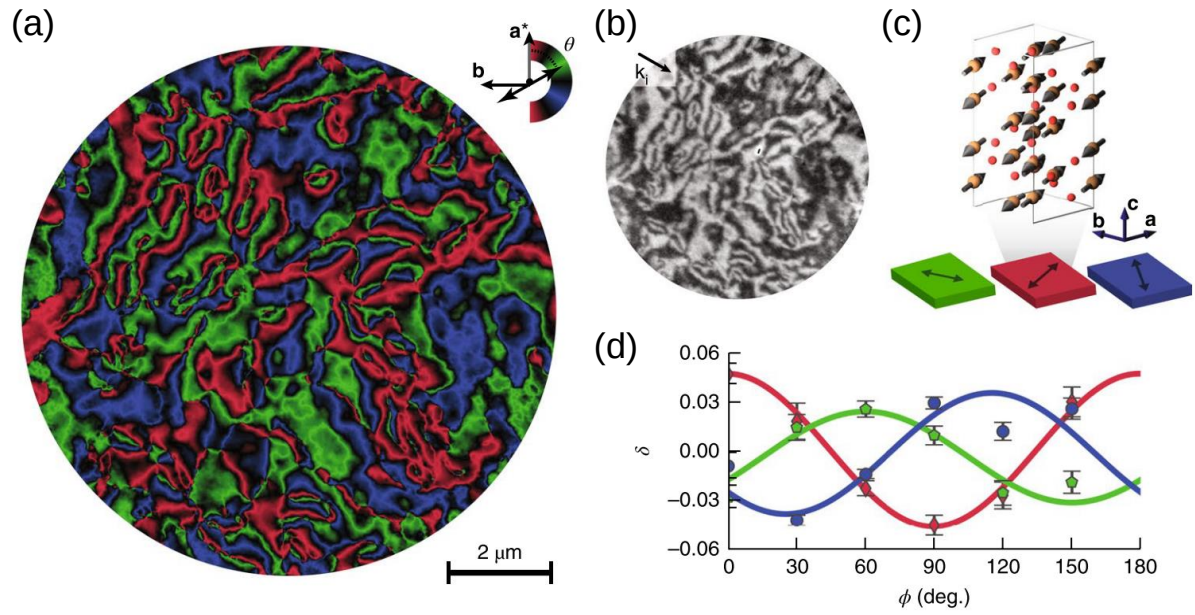

Figure 4-11: Vector map of α-Fe_2O_3 domains imaged using X-ray PEEM. (a) The domain structure of α-Fe_2O_3 constructed from the anisotropy of the XMLD signal taken at multiple incident x-ray directions. (b) Measured XMLD – PEEM image for a single incident x-ray direction denoted by the black arrow. (c) Crystal structure of α-Fe_2O_3 showing the three in-plane domain spin directions (denoted green, red, and blue) possible above the Morin transition temperature. (d) Mean XMLD (dichroism) signal intensity of a 15×15 pixel region of the PEEM image that contains one of the domain spin directions, as a function of the angle of the incident x-ray direction with respect to the a* direction.

each pixel represents a 10-nm × 10-nm region, the resolution is practically limited to 100-nm by sample and beam drifting and optical distortions.

4.4.4 Vector maps of α-Fe_2O_3 Domains

Roughly equal populations of each of the three allowed spin directions is observed with 31.8% red, 33.9% blue, and 34.3% green. This is what would be expected if no external bias was present when the α-Fe_2O_3 layer was grown. The topology is generally described as consisting of domains roughly 1-μm in diameter with some narrower domains of roughly 0.5-μm width that tend to meet at a singular point. The domains at these singular points are arranged in a periodic fashion either having 3-fold or 6-fold symmetries. The 6-fold symmetry points have a R-G-B-R-G-B or R-B-G-R-B-G periodic arrangement going around the point clockwise. The topology of these points is similar to the ferroelastic domain patterns observed in hexagonal $YMnO_3$ thin films[45]. Both systems contain a first order phase transition with α-Fe_2O_3 having the Néel transition at T_N and $YMnO_3$ having a Curie transition at T_C. If we treat α-Fe_2O_3 as a magnetic analog to $YMnO_3$, the vortices are topological defects. Topological defects will form when crossing the transition from paramagnetic to antiferromagnetic phase with size and quantity that survive dictated by the quenching rate due to the Kibble-Zurek mechanism[46]. While our XMLD technique is insensitive to the sign of the spin direction, we can interpret that the singular points are the loci of anti-phase domains. The free energy of the α-Fe_2O_3 system has Z_6 symmetry with six possible domain spin directions. Thus, we can reinterpret our periodic domain arrangement as R-G'-B-R'-G-B' (vortices) or R-B'-G-R'-B-G' (anti-vortices). In Figure 4-12c and Figure 4-13 we label these as white dots (vortices) and black dots (anti-vortices) to mark the core of the vortex. Antiferromagnetic vortices are topologically distinct entities with ± 1 winding numbers. We find that the vortices are usually found in vortex/anti-vortex pairs.

4.4.5 Coupling Between AFM and FM Domain Structures

Exchange proximity in AFM/FM heterostructures has been extensively studied, with particular interest in its use in potential multiferroic devices[47,48]. The magnetization and domain structure of a coupled ferromagnet can easily be red out compared to the much more difficult task of reading out the antiferromagnetic order. The α-Fe_2O_3/Co system of a general antiferromagnet and a simple elemental ferromagnet makes for an ideal system for studying the exchange coupling mechanism. XMCD is used to construct the real space in-plane magnetization vector map of the Co layer as detailed in section 4.4.3. The vector map of the Co layer shows sub-micron scale texturing with the Co magnetization tending to align

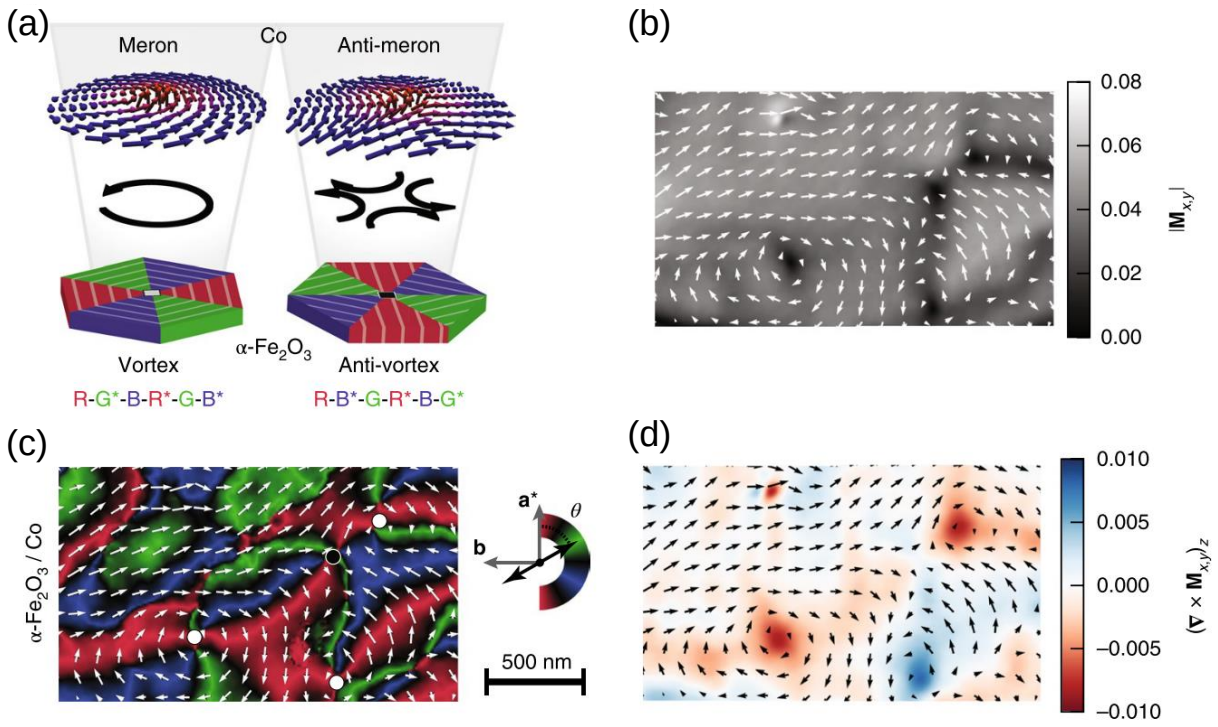

Figure 4-12: Topological features of the α-Fe_2O_3 and Co layers. (a) Schematic showing the coupling that is observed between the α-Fe_2O_3 vortices/antivortices and the Co merons/antimerons. (b) Magnitude of the Co magnetization in-plane. The reduction in intensity at the core of the vortex is consistent with it being a meron/antimeron. (c) Overlay of the magnetic domains of both the α-Fe_2O_3 and Co layers with white arrows signifying the FM domains and color signifying the AFM domains. Measurement area taken from the white dashed region of Figure 4-13a. White and black dots represent topological features with a winding number of +1 and -1, respectively. (d) Out-of-plane component of the curl of the Co vector map.

parallel to the spin direction of the α-Fe_2O_3 layer. Vortex structures present in the α-Fe_2O_3 layer also imprint into the Co layer (Figure 4-12a). Figure 4-12c overlays the Co vector map (white arrows) onto the colored vector map of the α-Fe_2O_3 spin direction. The vortex cores of the Co align exactly with the α-Fe_2O_3 vortices (white and black dots). In Figure 4-12d the curl of the Co magnetization $\left(\vec{\nabla} \times \vec{M}_{x,y}\right)_z$ is plotted to highlight vortices with differing vorticity, with clockwise vortices having negative curl and anti-clockwise vortices having positive curl. Vortex cores are also highlighted by a reduction in the in-plane magnetization magnitude (dark regions of Figure 4-12b). The size of the vortex cores is approximated as 100-nm from the FWHM of the fitted peak of the magnetization magnitude. The reduction of the in-plane magnetization at the vortex core could signify a change to an out-of-plane magnetization vector so that unfavorable exchange is satisfied[49]. If the core has an out-of-plane magnetization, that would make the vortices in the Co layer merons/antimerons (Figure 4-12a) instead of a planar vortex[50]. Previously, merons had only been observed in geometrically confined structures such as nanodots[51,52] with this potentially being the first report of such magnetic topologies in thin films. The extreme thinness of the Co (~1-nm) means that exchange anisotropy with the antiferromagnetic layer dominates over the energy associated with magnetic dipole-dipole interactions that would favor a more topologically trivial parallel alignment of the Co spins.

4.4.6 Vortex Annihilation

A vortex core, being a topologically protected defect, is invariant under external perturbations such as the application of an external magnetic field. However, if a vortex core is paired with a topological defect with an equal and opposite winding number, the pair can annihilate assuming sufficient energy is provided to overcome the kinetics. If the vortices observed in the x-ray PEEM vector maps of α-Fe_2O_3/Co are topological defects, it follows that they must show this stability. To test this, an external field was applied to the sample outside of the PEEM vacuum chamber with a strength of 100 mT along the [110] direction and then

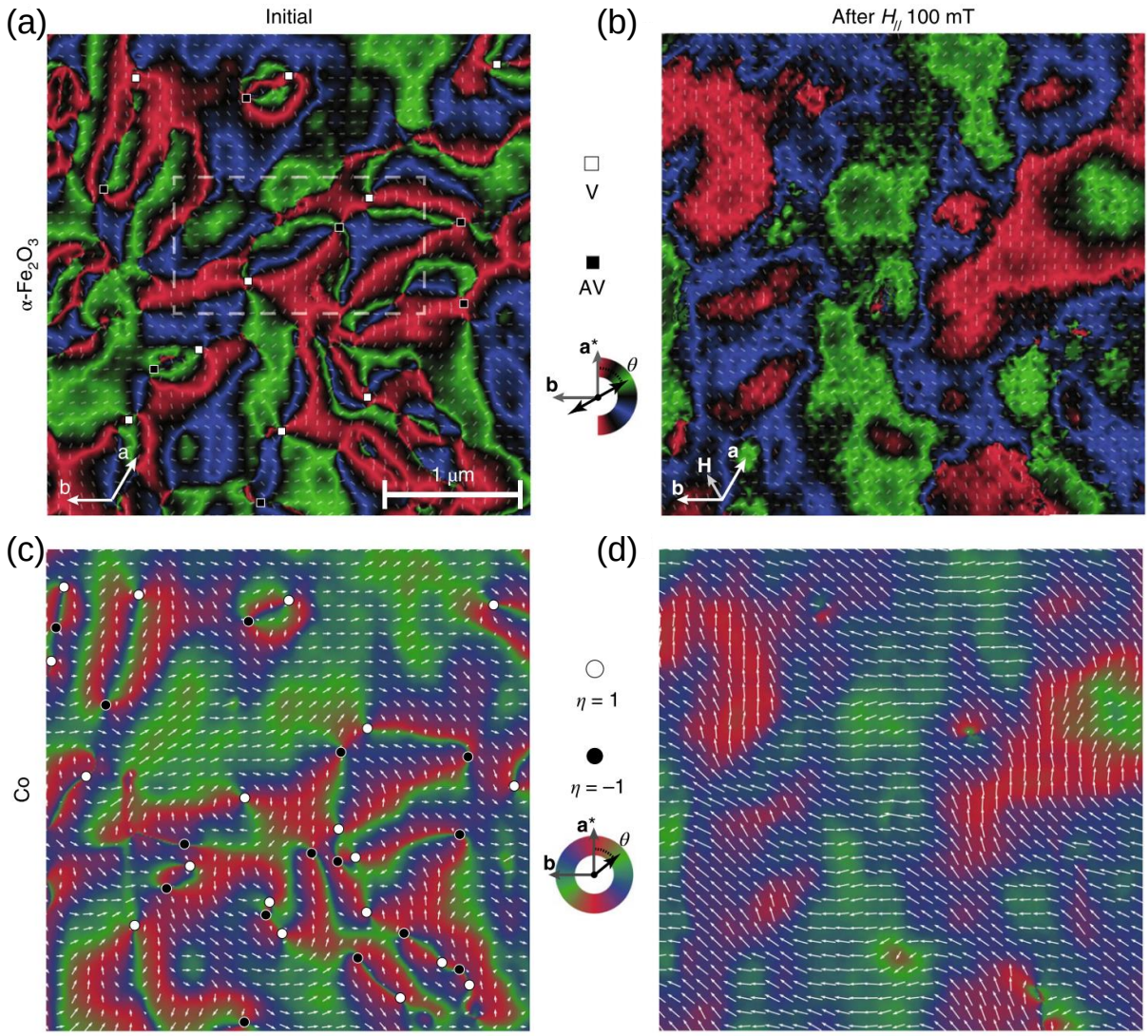

Figure 4-13: Magnetic domains of the α-Fe_2O_3 and Co layers before and after application of external field. (a) AFM domain structure of the α-Fe_2O_3 before application of external magnetic field. Domain image is constructed from XMLD – PEEM images. White and black dots mark the approximate center of vortices and antivortices, respectively. The white bars mark the averaged AFM spin direction for each 10×10 pixel region. The RGB colors represent the angle of the AFM spin direction with respect to the a* direction with black regions representing areas that deviate in angle from the three domain spin directions. Domain walls between the domains are in these black regions. (b) AFM domain structure of the α-Fe_2O_3 after application of external 100 mT magnetic field along [110]. (c) A vector map of the Co spin orientations. White and black dots represent topological features with a winding number of +1 and -1, respectively. White arrows mark the averaged FM spin direction for each 10×10 pixel region. The RGB colors represent the angle of the AFM spin direction with respect to the a* direction. (d) Vector map of Co after field was applied. All images of the same region of the sample.

remeasured again. The same region of the sample was located again by locating the carbon contamination caused by exposure to the x-ray beam. Figure 4-13 shows the domain morphology in the Co and α-Fe_2O_3 layers before and after application of the magnetic field. The domain morphology after exposure to the magnetic field has been transformed with large domains several microns in size and no vortices at all. The vortices present before applying the field have disappeared. Regions not near or between pairs of vortices seem to be unaffected by the applied field demonstrating that the change in domain morphology was caused by vortex annihilation. The Co is still magnetically aligned parallel to the α-Fe_2O_3 magnetic spin direction confirming that the Co layer is strongly coupled to the α-Fe_2O_3 layer. The stability of the antiferromagnetic vortices to external perturbation could make them useful for memory devices. Information could be stored in the vorticity of each vortex (1 for clockwise, 0 for anti-clockwise).

4.5 Conclusions

In conclusion, we have optimized the deposition of α-Fe_2O_3 thin films using reactive sputtering leading to a phase pure thin film with no discernible minority phases of Fe_3O_4. We have shown that the Morin transition temperature decreases and is ultimately suppressed entirely in ultrathin films. Vector maps of the domain structure present in the ultrathin α-Fe_2O_3 thin film was created using x-ray PEEM showing sub-micron sized domains and vortices much like the structural vortices in $YMnO_3$ due to the Kibble mechanism. The antiferromagnetic domains and vortices are imprinted onto the Co overlayer which was deposited directly onto the α-Fe_2O_3. In the future, mapping the magnetization of the Co layer using MFM could be used as an indirect method of mapping the domain structure in the antiferromagnetic α-Fe_2O_3 layer. Follow on studies are focused on regeneration of vortices using thermal cycling after annihilation with an external magnetic field as well as chemical doping of the α-Fe_2O_3 to change the size of the vortices[26].

4.6 References

1. Pauling, L. & Hendricks, S. B. The crystal structures of hematite and corundum. *J. Am. Chem. Soc*. **47**, 781–790 (1925).
2. Blake, R. L., Zoltai, T., Hessevick, R. E. & Finger, L. W. Refinement of Hematite Crystal Structure. *Am. Mineral.* **51**, 123–129 (1970).
3. Verwey, E. J. W. The Crystal Structure of γ-Fe2O3 and γ-Al2O3. *Zeitschrift für Krist. - Cryst. Mater*. **91**, 65–69 (1935).
4. Morin, F. J. Magnetic Susceptibility of αFe203 and αFe203 with Added Titanium. *Phys. Rev.* **78**, 819–820 (1950).
5. Artman, J. O., Murphy, J. C. & Foner, S. Magnetic Anisotropy in Antiferromagnetic Corundum-Type Sesquioxides. *Phys. Rev.* **138**, A912–A917 (1965).
6. Besser, P. J., Morrish, A. H. & Searle, C. W. Magnetocrystalline anisotropy of pure and doped hematite. *Phys. Rev.* **153**, 632–640 (1967).
7. Coey, J. M. D. & Sawatzky, G. A. A study of hyperfine interactions in the system (Fe1-xRh x)2O3 using the Mossbauer effect (Bonding parameters). *J. Phys. C Solid State Phys.* **4**, 2386–2407 (1971).
8. Shimomura, N. *et al.* Morin transition temperature in (0001)-oriented α-Fe2O3 thin film and effect of Ir doping. *J. Appl. Phys.* **117**, 1–5 (2015).
9. Fujii, T., Takano, M., Kakano, R., Isozumi, Y. & Bando, Y. Spin-flip anomalies in epitaxial α-Fe2O3 films by Mössbauer spectroscopy. *J. Magn. Magn. Mater.* **135**, 231–236 (1994).
10. Gota, S., Gautier-Soyer, M. & Sacchi, M. Magnetic properties of Fe2O3 (0001) thin layers studied by soft x-ray linear dichroism. *Phys. Rev. B* **64**, 224407 (2001).
11. Néel, L. & Pauthenet, R. Etude thermomagnétique d'un monocristal de Fe2O3-alpha. *Comptes Rendus Hebd. Des Seances L Acad. Des Sci.* **234**, 2172–2174 (1952).
12. Nathans, R., Pickart, S. J., Alperin, H. A. & Brown, P. J. Polarized-Neutron Study of Hematite. *Phys. Rev.* **136**, A1641–A1647 (1964).
13. Hill, A. H. *et al.* Neutron Diffraction Study of Mesoporous and Bulk Hematite, α-Fe2O3. *Chem. Mater.* **20**, 4891–4899 (2008).
14. Mishra, M. & Chun, D. M. α-Fe2O3 as a photocatalytic material: A review. *Appl. Catal. A Gen.* **498**, 126–141 (2015).
15. Jia, L., Harbauer, K., Bogdanoff, P., Ellmer, K. & Fiechter, S. Sputtering Deposition of Ultra-thin α-Fe2O3 Films for Solar Water Splitting. *J. Mater. Sci. Technol.* **31**, 655–659 (2015).
16. Aragón, F. F. H. *et al.* Effect of the thickness reduction on the structural, surface and magnetic properties of α-Fe2O3 thin films. *Thin Solid Films* **607**, 50–54 (2016).
17. Walz, F. The Verwey transition - A topical review. *J. Phys. Condens. Matter* **14**, (2002).

18. García, J. & Subías, G. The Verwey transition - A new perspective. *J. Phys. Condens. Matter* **16**, (2004).

19. Mamani, J. B., Gamarra, L. F. & Brito, G. E. de S. Synthesis and characterization of Fe3O4 nanoparticles with perspectives in biomedical applications. *Mater. Res.* **17**, 542–549 (2014).

20. Frandsen, B. A. *et al.* Superparamagnetic dynamics and blocking transition in Fe3 O4 nanoparticles probed by vibrating sample magnetometry and muon spin relaxation. *Phys. Rev. Mater.* **5**, 1–12 (2021).

21. Bhowmik, R. N. & Saravanan, A. Surface magnetism, Morin transition, and magnetic dynamics in antiferromagnetic α-Fe2O3 (hematite) nanograins. *J. Appl. Phys.* **107**, (2010).

22. Mørup, S., Madsen, D. E., Frandsen, C., Bahl, C. R. H. & Hansen, M. F. Experimental and theoretical studies of nanoparticles of antiferromagnetic materials. *J. Phys. Condens. Matter* **19**, (2007).

23. Amin, N. & Arajs, S. Morin temperature of annealed submicronic α - F2O3 particles. *Phys. Rev. B* **35**, 4810–4811 (1987).

24. Bødker, F., Hansen, M. F., Koch, C. B., Lefmann, K. & Mørup, S. Magnetic properties of hematite nanoparticles. *Phys. Rev. B* **61**, 6826–6838 (2000).

25. Chmiel, F. P. *et al.* Observation of magnetic vortex pairs at room temperature in a planar α-Fe2O3/Co heterostructure. *Nat. Mater.* **17**, 581–585 (2018).

26. Jani, H. *et al.* Antiferromagnetic half-skyrmions and bimerons at room temperature. *Nature* **590**, 74–79 (2021).

27. Sáenz, J. J. *et al.* Observation of magnetic forces by the atomic force microscope. *J. Appl. Phys.* **62**, 4293–4295 (1987).

28. Martin, Y. & Wickramasinghe, H. K. Magnetic imaging by ‘“force microscopy”’ with 1000 Å resolution. *Appl. Phys. Lett.* **50**, 1455–1457 (1987).

29. Freeman, M. R. & Choi, B. C. Advances in Magnetic Microscopy. *Science (80-.).* **294**, 1484–1488 (2001).

30. Williams, H. J., Foster, F. G. & Wood, E. A. Observation of Magnetic Domains by the Kerr Effect. *Phys. Rev.* **82**, 119–120 (1951).

31. Argyle, B. E. & McCord, J. G. New laser illumination method for Kerr microscopy. *J. Appl. Phys.* **87**, 6487–6489 (2000).

32. *Spin Dynamics in Confined Magnetic Structures I*. vol. 83 (Springer Berlin Heidelberg, 2002).

33. Rougemaille, N. & Schmid, A. K. Magnetic imaging with spin-polarized low-energy electron microscopy. *EPJ Appl. Phys.* **50**, 201011–2010118 (2010).

34. Schtz, G. *et al.* Absorption of circularly polarized x rays in iron. *Phys. Rev. Lett.* **58**, 737–740 (1987).

35. Vogel, J. *et al.* Interplay between magnetic anisotropy and interlayer coupling in nanosecond magnetization reversal of spin-valve trilayers. *Phys. Rev. B - Condens. Matter Mater. Phys.* **71**, 1–4 (2005).

36. Kirtley, J. R. *et al.* High-resolution scanning SQUID microscope. *Appl. Phys. Lett.* **1138**, 1138 (1995).

37. Gross, I. *et al.* Real-space imaging of non-collinear antiferromagnetic order with a single-spin magnetometer. *Nature* **549**, 252–256 (2017).

38. Wang, H. *et al.* Noninvasive measurements of spin transport properties of an antiferromagnetic insulator. *Sci. Adv.* **8**, 4–10 (2022).

39. Welter, P. *et al.* Fast scanning nitrogen-vacancy magnetometry by spectrum demodulation. **1**, 1–11 (2022).

40. Bezencenet, O., Bonamy, D., Belkhou, R., Ohresser, P. & Barbier, A. Origin and Tailoring of the Antiferromagnetic Domain Structure in α-Fe2O3 Thin Films Unraveled by Statistical Analysis of Dichroic Spectromicroscopy (X-Ray Photoemission Electron Microscopy) Images. *Phys. Rev. Lett.* **106**, 107201 (2011).

41. Dhesi, S. S. *et al.* The nanoscience beamline (I06) at diamond light source. *AIP Conf. Proc.* **1234**, 311–314 (2010).

42. Laan, G. van der & Kirkman, I. W. The 2p absorption spectra of 3d transition metal compounds in tetrahedral and octahedral symmetry. *J. Phys. Condens. Matter* **4**, 4189–4204 (1992).

43. Stöhr, J. & Siegmann, H. C. *Magnetism: From Fundamentals to Nanoscale Dynamics*. (Springer Berlin Heidelberg, 2006). doi:10.1007/978-3-540-30283-4.

44. Laan, G. van der. Applications of soft x-ray magnetic dichroism. *J. Phys. Conf. Ser.* **430**, 012127 (2013).

45. Huang, F.-T. & Cheong, S.-W. Aperiodic topological order in the domain configurations of functional materials. *Nat. Rev. Mater.* **2**, 17004 (2017).

46. Zurek, W. H. Cosmological experiments in superfluid helium? *Nature* **317**, 505–508 (1985).

47. Heron, J. T. *et al.* Deterministic switching of ferromagnetism at room temperature using an electric field. *Nature* **516**, 370–373 (2014).

48. Saenrang, W. *et al.* Deterministic and robust room-temperature exchange coupling in monodomain multiferroic BiFeO3 heterostructures. *Nat. Commun.* **8**, (2017).

49. Shinjo, T., Okuno, T., Hassdorf, R., Shigeto, K. & Ono, T. Magnetic vortex core observation in circular dots of permalloy. *Science (80-.).* **289**, 930–932 (2000).

50. Senthil, T., Vishwanath, A., Balents, L., Sachdev, S. & Fisher, M. P. A. Deconfined Quantum Critical Points. *Science (80-.).* **303**, 1490–1494 (2004).

51. Cowburn, R. P., Koltsov, D. K., Adeyeye, A. O., Welland, M. E. & Tricker, D. M. Single-domain circular nanomagnets. *Phys. Rev. Lett.* **83**, 1042–1045 (1999).

52. Wintz, S. *et al.* Topology and origin of effective spin meron pairs in ferromagnetic multilayer elements. *Phys. Rev. Lett.* **110**, 1–5 (2013).

Chapter 5

Adsorption-controlled Growth of $SrTiO_3$ using Metal-organic Pulsed Laser Deposition

5.1 Introduction to $SrTiO_3$

Strontium titanate ($SrTiO_3$ or STO) is a commonly used perovskite material that has been studied extensively for several decades both for its functional properties as well as its usefulness as a substrate template for the growth of other perovskite materials. STO is a cubic perovskite with a $Pm\bar{3}m$ structure with a lattice parameter of a = 3.905 Å. Electrically, it is a wide-band gap semiconductor with an indirect band gap of 3.2 eV[1]. The first-principles ground state of STO has a ferroelectric distortion however such long-range order is prevented by quantum mechanical fluctuations and the paraelectric-ferroelectric quantum phase transition is not reachable in bulk STO[2]. As a result, a large dielectric constant of $\varepsilon_0 \approx 2\times10^4$ arises[3] which has led to the STO being studied as a potential high-k dielectric in CMOS. At low temperatures (T < 0.5 K) and high doping (10^{18} cm^{-3} < n < 10^{21} cm^{-3}), unconventional superconductivity has been observed with ongoing debate about its origins[4,5]. A conductive two-dimensional electron gas was found to form at the interface of $LaAlO_3$ and $SrTiO_3$ (LAO/STO 2DEG)[6]. For this investigation, we chose to use the LAO/STO 2DEG as a model system to demonstrate adsorption-controlled growth and was chosen instead of measuring the properties of the STO itself to avoid the need for chemical doping. The properties

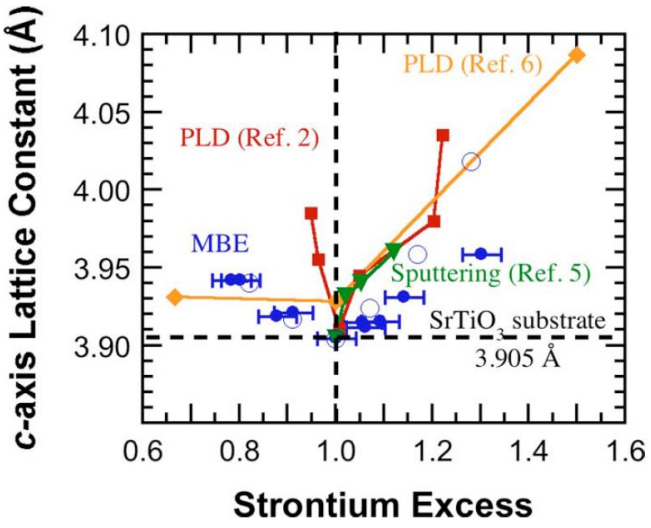

Figure 5-1: Lattice expansion of $SrTiO_3$ due to non-stoichiometry. Out-of-plane lattice parameter is plotted as a function of strontium concentration in STO grown by a variety of thin film deposition techniques (PLD, MBE, and RF Sputtering). Reproduced from reference[14] with permission from Applied Physics Letters.

of the 2DEG resemble that of STO itself, including a similar superconducting dome[7], implying that the properties of the 2DEG are highly dependent on the properties and quality of the STO.

5.2 Introduction to MOPLD

Stoichiometry control in compound materials is much like balancing on a sharp edge. Small deviations from the stoichiometric growth parameters which can occur run-to-run when depositing thin films, can lead to off-stoichiometry that is observable in the film's properties (Figure 5-1). If we could use thermodynamic-driven processes to drive each deposition towards stoichiometry, the film quality would no longer be dictated by the repeatability of the growth. The first demonstration of an adsorption-controlled thin film deposition method was with the growth of GaAs using reactive molecular beam epitaxy (MBE). The high volatility of As gives rise to the growth window shown in Figure 5-2a with a As pressure range that yields stoichiometric GaAs that is many orders of magnitude. The growth window is bounded by two equilibrium equations that bound the region where As will condense on the surface to form GaAs and excess As will

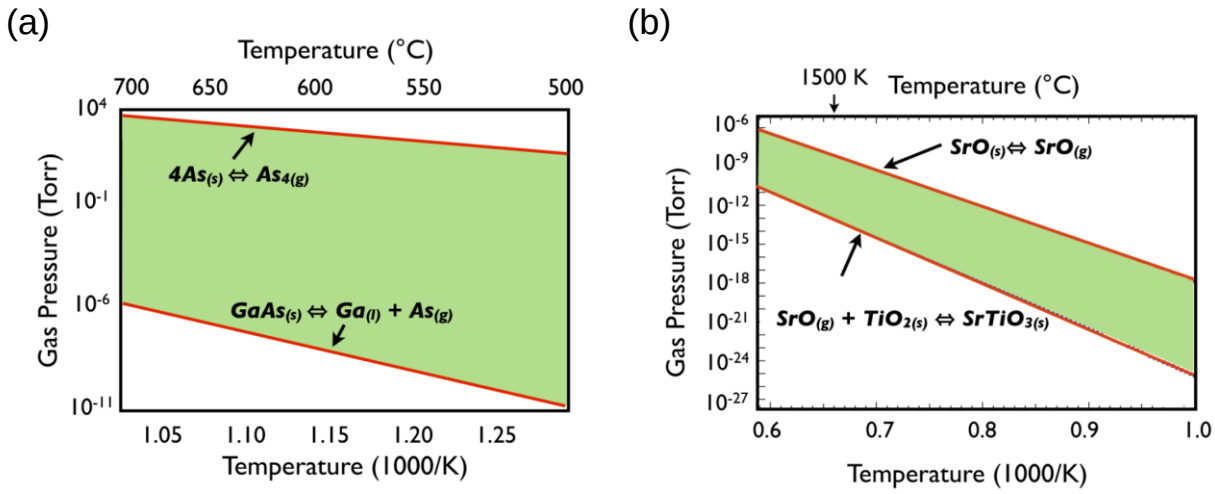

Figure 5-2: Gas pressure growth window for GaAs and $SrTiO_3$. The growth window is shaded green bounded by the equilibrium curves in red for the two reactions governing adsorption-controlled growth. (a) Growth window of As gas pressures and substrate temperatures where stoichiometric GaAs can be grown. (b) Growth window of Ti gas pressures and substrate temperatures where stoichiometric STO can be grown. Reproduced from reference[21] with permission.

desorb. Above the upper equation, excess As will not be desorbed from the GaAs surface and below the lower equation, the GaAs compound will not form. Using the same methods, a theoretical growth window of STO grown by MBE is calculated (Figure 5-2b). Not only is the width of the STO growth window much narrower, the lower SrO pressures and higher growth temperatures needed make the growth window experimentally unobtainable. This necessitates a high vapor pressure source for one of the elements.

Recently, a hybrid MBE technique that combines the near-equilibrium process of MBE and MOCVD has been developed[8]. Instead of using an elemental Ti source, Ti is supplied by a metal-organic precursor. This makes the Ti source volatile like an As source making the adsorption-controlled growth window obtainable. We have taken this idea further by combining the near-equilibrium process of MOCVD with the high energy pulsed laser deposition (PLD) technique, or metal-organic pulsed laser deposition (MOPLD). We demonstrate that we can not only control the stoichiometry of STO grown by MOPLD, but also control the concentration of defects.

5.2.1 TiO_2 Deposition by Metal-organic Precursor

A near-equilibrium Ti source is challenging as Ti metal has a low vapor pressure and heating Ti to a high temperature to obtain a suitable vapor pressure is complicated by titanium's reactivity to crucible materials limiting the Ti growth rate. Use of an oxygen source when depositing TiO_2 further complicates the issue and can cause flux instability of the Ti source by oxidizing the surface of the Ti melt in the source. Electron beam evaporators can obtain higher Ti growth rates at the expense of flux instability. A Ti metal-organic precursor such as titanium tetra isopropoxide (TTIP) benefits from many orders of magnitude higher vapor pressure, with little to no flux drift or need for *in-situ* flux calibration, and has been previously used to grow TiO_2. TiO_2 growth rate by TTIP is highly temperature dependent. Growth rate r_S is determined by three different rate constants that follow a simple Arrhenius form, the reaction rate k_S, the adsorption rate k_A, and the desorption rate k_D using Equation 5-1. Usually such precursors, especially for atomic layer deposition

$$\mathrm{r_s} = \frac{k_S K_A P_{TTIP}}{\frac{k_S}{k_D} + 1 + K_A P_{TTIP}} \; where \; K_A = \frac{k_A}{k_D} \tag{5-1}$$

(ALD), are used at low temperatures where growth rate is inelastic to growth temperature. This region can be found at the low temperature end of the reaction-limited regime of a precursor's rate versus temperature curve[9]. The reaction-limited regime is exponential due to the Arrhenius dependence of decomposition with thermal energy. ALD uses the low slope at the foot of the exponential curve. Above the reaction-limited regime is an intermediate region where all precursor molecules that impinge on the surface decompose and the only limit is the flux of precursor hitting the surface. The reaction rate is greater than the desorption rate. Finally, at high-temperatures, desorption from the surface dominates. Desorption rates are greater than reaction rates meaning the precursor molecules statistically will leave the surface of the substrate before it reacts with the surface and decomposes. For the case of STO, the desorption rate is higher for TiO_2-terminated surfaces than SrO-terminated surfaces leading to the adsorption-controlled growth window.

5.3 System Design

Specific adaptations to the conventional PLD system design had to be made to make MOPLD possible. Foremost, is the requirement for a source port for the gas injector that is on-axis with the sample stage. While multiple on-axis ports are a common feature of MBE or sputtering deposition systems, PLD systems may only have one on-axis port usually used for the target carousel. First, a test system was developed using a single rotating ablation target and a second on-axis port for the precursor gas injector. The existence of an adsorption-controlled growth window was confirmed using this system setup. Next, a custom MOPLD system was developed (Figure 5-3). An ablation target carousel with up to four targets was mounted perpendicular to the sample stage with six on-axis source ports facing the sample stage arranged circularly around the target stage, 44° from the sample stage normal. The target carousel is designed to be low profile as to not block line of sight to the sample from the six source ports. For MOPLD, single crystal ablation targets are desired over typical polycrystalline sintered targets due to single crystal's higher purity and 100% density, reducing defects in the grown thin film from impurities. These source ports were used for precursor gas injectors, molecular beam effusion cells, e-beam evaporators, and *in-situ* analysis tools. Two of the ports were upwards facing and so reserved for molecular beam effusion cells. Additionally, these ports were equipped with retractable stages and could be gated off so that hot cells could be isolated from high growth pressures of subsequent PLD-grown thin films or post-growth high pressure annealing. This feature could also be used for reloading or swapping of effusion cells. For *in-situ* growth analysis, a reflection high energy electron diffraction (RHEED) system was added to the new system. While growth pressures for MOPLD are in the high vacuum regime like MBE, layers of heterostructures grown by conventional PLD require growth pressures in the low vacuum regime (1 to 1000 mTorr). The RHEED electron beam source filament is differentially pumped through a series of two small orifices by small turbomolecular pumps such that the pressure at the filament can be up to six orders of magnitude lower

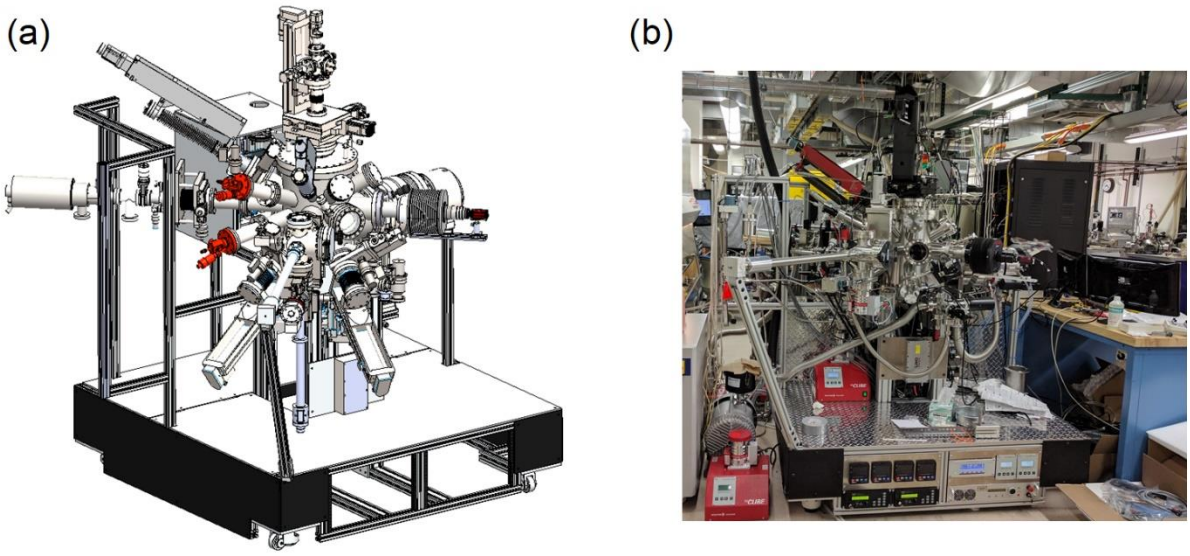

Figure 5-3: MOPLD system. (a) An isometric view of the computer aided design (CAD) design of the MOPLD system. The gas injectors are highlighted in red. (b) A picture of the MOPLD system.

than the growth pressure. The mean free path of the electron beam in the low vacuum regime is reduced so the final orifice and the RHEED screen are placed close to the sample stage reducing the distance electrons need to travel at growth pressures. A fiber laser powered sample heating system is used to reach sample temperatures not possible with a resistive sample heater (as shown in Figure 5-5a). A resistive heater is limited to around 900°C while the laser heater can reach temperatures up to 1200°C. Higher sample temperatures are desirable as the width of the adsorption-controlled growth window was found to increase with increasing sample temperature[10].

5.3.1 Precursor Gas Delivery Design

The precursor gas was supplied by thermal evaporation of the precursor. For the deposition of STO, the metal-organic TiO_2 precursor titanium(IV) tetra isopropoxide (TTIP) was used which was supplied by Sigma Aldrich (99.999% trace metals basis). Four oxygen atoms are bonded to the central Ti atom of TTIP supplying both titanium and oxygen when the molecule decomposes on the heated sample surface following Equation 5-2 at temperatures above 400°C[11,12]. Originally, a heated mass flow controller (MKS 1150C) was

$$\mathrm{Ti(OC_3H_7)_4} \xrightarrow{\mathrm{T > 400°C}} \mathrm{TiO_2} + 4\mathrm{C_3H_6} + 2\mathrm{H_2O} \tag{5-2}$$

used to control the flow rate. However, the resolution and repeatability of the mass flow controller (±0.1% of full scale) was insufficient to reliably control the flow of the precursor. Instead, to control the flow rate of the precursor gas, the pressure in the foreline feeding the gas injector (E-Science Ultra Low Temperature Gas Injector with PBN showerhead and heated using a EpiTech 800 power supply) was controlled. A

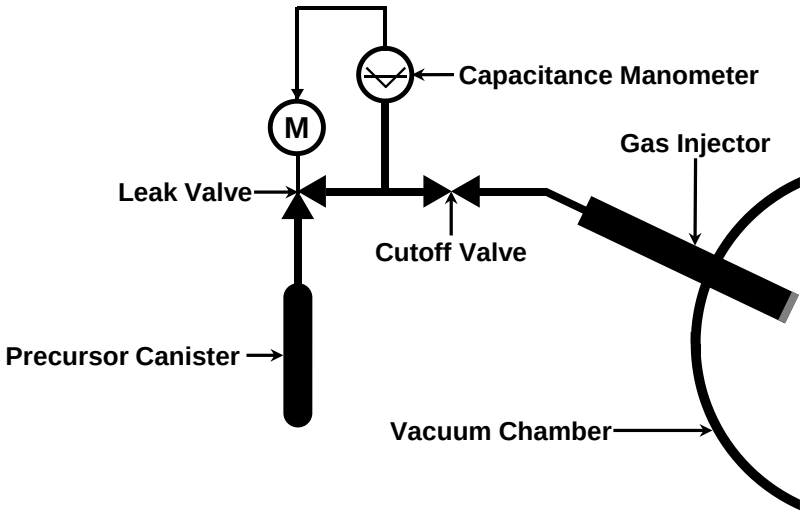

Figure 5-4: Metal-organic precursor gas delivery system schematic. The liquid precursor is held in a canister which is heated to produce sufficient vapor pressure. The motorized leak valve controls the flow of the vapor into the foreline. The amount of vapor in the foreline is measured by a capacitance manometer which is fed back to control the position of the leak valve. A cutoff valve controls the flow to the gas injector and into the chamber.

schematic of the control system is shown in Figure 5-4. The pressure controller (MKS 651C) used a heated capacitance manometer pressure gauge (MKS 631F 1-Torr) connected to the gas injector foreline as an input and using a PID control loop, set the position of an upstream control valve (MKS 245 with 8-inch valve extender between the valve body and the motor assembly allowing for elevated working temperatures) to maintain the pressure setpoint in the foreline. Flow was turned off and on using a pneumatic valve (Swagelok ALD). All components of the foreline were heated to prevent condensation of the precursor. For TTIP, the gas injector was held at a temperature of 120°C. The temperature of the precursor canister was slowly raised until a suitable pressure in the foreline was maintained. To heat the gas line and components without built in heating elements, heating tape was wrapped around each component and then insulated with aluminum foil. Power to the heating tape is set using a variable AC transformer and temperature was monitored by thermocouples placed on each component.

5.3.2 Pump Layout

Special consideration to what types of vacuum pumps are used is needed due to the use of the metal-organic precursor gas. An overview of how pumps were connected to the system is shown in Figure 5-5b. For the main chamber, a turbomolecular pump (Pfeiffer HiPace 1200) is used as the high vacuum pump. This allows the main chamber to quickly reach an acceptable base pressure after doing a post-growth 1-atmosphere O_2 anneal. A scroll pump (Edwards XDS35i) is used as the backing/low vacuum pump. Using a dry pump negates the need to use expensive fluorocarbon oil needed when pumping on a chamber containing O_2 gas. This also eliminates challenges disposing of oil used to pump potentially toxic precursor gases. To further increase the pumping speed of the precursor, a cryopanel was inserted into the chamber (as seen in Figure 5-5a). Cryopanels are often used in molecular beam epitaxy chambers and use LN_2 for cooling to condense low boiling point gases such as O_2. For MOPLD, we are only interested in condensing the metal-organic precursor, most of which have melting points around room temperature. A propylene glycol-based coolant is used to chill the cryopanel to -20°C, cold enough that most precursors that might

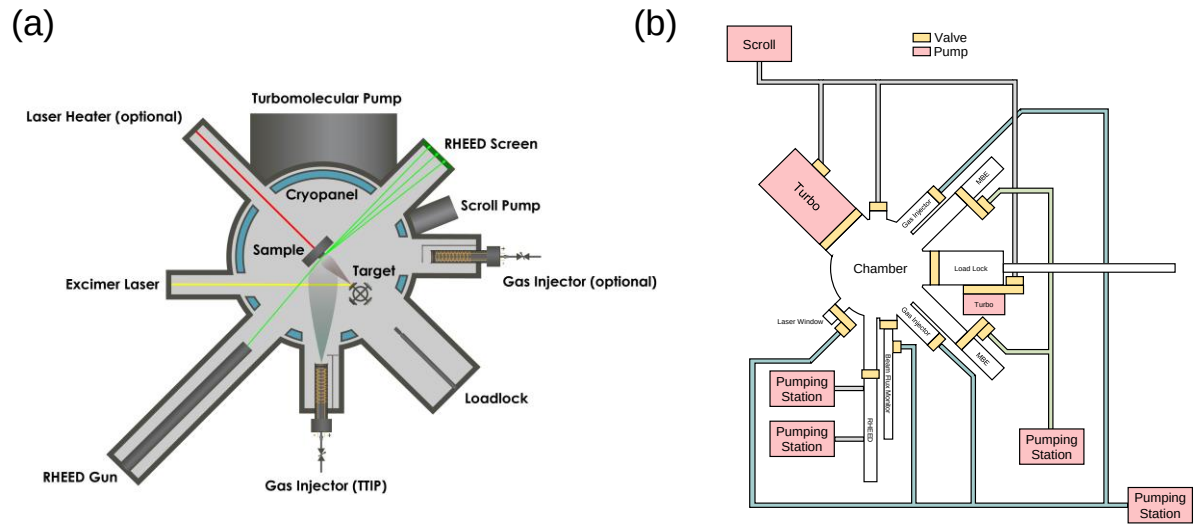

Figure 5-5: MOPLD chamber schematics. (a) A schematic showing the layout of the main chamber and the positioning of various subsystems attached to the chamber. RHEED electron beam (green), PLD excimer laser (yellow), and substrate heating laser (red) are shown as lines. (b) A schematic of how the chamber and subsystems are connected. Valves are shown in yellow, and pumps are shown in red.

be used have negligible vapor pressures. The cryopanel sits in front of the chamber walls and provides a chilled surface for precursor molecules to condense on instead of contributing to the background pressure of the chamber during growth. If a buildup of precursor occurs during growth, the effective flux of precursor at the sample could increase during the growth, eventually changing the effective flux rate enough so that the rate falls outside the adsorption-controlled growth window. The cryopanel can also reduce transient affects where precursor continues to be present in the chamber after the gas injector is closed. Precursor that condenses on the chilled cryopanel during the growth is pumped out of the chamber by the turbomolecular pump when the cryopanel is heated back to room temperature. The cryopanel was normally allowed to warm up overnight when the chamber was not in use.

5.3.3 PLD Laser Window Design

Unique to combining PLD with the use of a metal-organic precursor is metal-organic related contamination of the laser entrance window which can decrease the laser fluence that reaches the ablation target. Contamination of the laser entrance window is a common issue in regular PLD that can occur over the course of many runs especially for depositions with high laser fluence or high repetition rate. This necessitates periodic cleaning of the vacuum side surface of the window. The contamination issue for MOPLD occurs much more quickly, enough to cause the growth conditions to drift out of the growth window after a particularly long deposition. We theorized that TTIP molecules that are adsorbed onto the window surface are decomposed by the energy of the excimer laser light transmitting through the window. This breaks the ligands from the TTIP depositing TiO_2 on the window surface. Contamination does not occur on parts of the window where the laser doesn't pass through suggesting the contamination occurs due to a combination of the presence of the TTIP precursor and the excimer laser light.

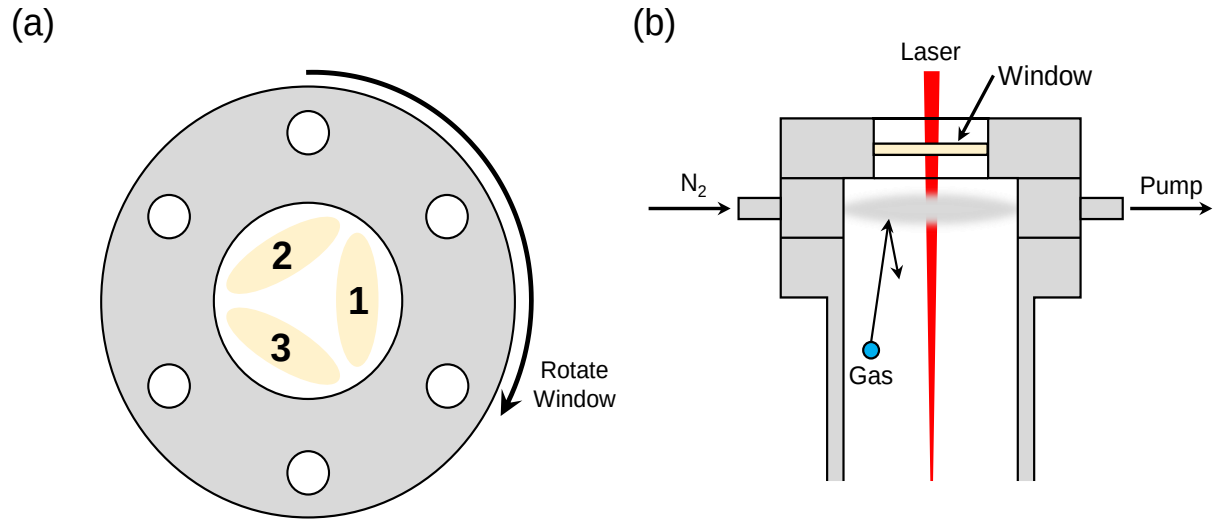

Figure 5-6: PLD laser entrance window designs. (a) A schematic of how the laser entrance window is rotated to expose three separate regions of the window to the laser beam, which has an ellipsoidal shape. The laser beam is offset from the window centerline. (b) A schematic of how a flow of gas on the vacuum side of the window can prevent gas molecules present in the chamber from reaching the window where they can cause contamination.

Many different solutions to this issue were examined. First, we need to make decontamination of the laser entrance window easier. Typically, a laser entrance window for 248 nm excimer lasers is made of fused silica with antireflective coating yielding a greater than 99.5% transmission at 248 nm. It was found that to remove the contamination on the window, a diamond polishing powder was needed to physically remove the layer. This can be time consuming and could easily lead to damage to the window. To be able to remove the contamination using chemical methods instead of physical ones, the window material was switched from a fused silica material to a crystalline MgF_2 material, which has a 94% transmission rate at 248 nm. The MgF_2 is cut along the c-axis of the crystal to minimize birefringence. Using MgF_2, buffered HF can be used to remove the contamination without etching of the window material. A few drops of buffered HF were applied to the vacuum side of the window and allowed to sit on the window surface before washing the entire window under RO water. Both physical and chemical methods require removal of the window from the chamber for cleaning. To accomplish this without venting of the whole chamber to atmosphere, a gate valve is placed between the window and the chamber. The gate valve is equipped with an extra port which is used for venting and pumping of the small volume between the valve and the window. To maintain ultra-high vacuum (UHV) conditions in the chamber, a copper O-ring is used to seal the gate valve to the window which is replaced whenever the window is removed to be cleaned.

By offsetting the position of the laser spot on the window, a total of three separate nonoverlapping positions were achievable, as shown in Figure 5-6a. Once a position becomes contaminated, the window could be rotated by 120 degrees to expose a new position of the window. Only once all three positions were contaminated, was the window cleaned chemically.

Ultimately, a method that prevents contamination of the laser entrance window entirely is preferred. Similar window contamination is a problem for MBE/PLD hybrid deposition techniques where flux from the molecular beam effusion cell can coat the vacuum side of the window. A technique that shields the inside of the window with a curtain of gas (Figure 5-6b) would presumably work well for the MOPLD

contamination problem as well. A molecular beam of N_2 gas was passed in front of the window which was aimed directly at a vacuum pump port. Many of the gas molecules pass directly from the gas inlet to the pumping port without colliding with each other or the chamber walls and thus not contributing to the background pressure in the chamber. Metal-organic molecules present in the chamber collide with the stream of N_2 gas and are unable to reach the window surface. While acting as a barrier to molecules in the chamber, the 248 nm excimer laser light passes through unaffected.

5.4 Deposition of $SrTiO_3$ using MOPLD

Substrates were either $(LaAlO_3)_{0.3}$-$(Sr_2AlTaO_6)_{0.7}$ (LSAT) or $SrTiO_3$ (STO) (001)-orientated single crystals depending on whether heteroepitaxy or homoepitaxy is desired. STO substrates were also annealed (1000°C for 6 hours in oxygen) as well as etched before and after annealing (double etched) to obtain a TiO_2-terminated step-terrace structure. To etch STO, substrates were soaked in water for 30 minutes and then dipped in 7:1 buffered hydrofluoric acid (BHF) for 1 minute and rinsed in RO water. The substrate was loaded into the MOPLD system and heated to a growth temperature of 900°C in an oxygen atmosphere. TTIP gas was supplied by a gas injector with a constant foreline pressure set by the control valve. A SrO single crystal is ablated by a KrF excimer laser (λ = 248 nm) with an energy fluence of 0.7 J/cm^2 and a repetition rate of 2 Hz supplying SrO. Thin film thickness was controlled by RHEED (Figure 5-7a). The growth mode was layer by layer and atomically flat step terracing of the surface was observed by AFM (Figure 5-7a inset). When grown on a LSAT substrate, XRD of the (-103) peak of the substrate and film (Figure 5-7b) show the STO thin film peak with the same in-plane lattice parameter showing that the film is epitaxially constrained to the substrate and not relaxed. Fitting of the XRR fringes of the STO on LSAT (Figure 5-7c) was used to calculate a film thickness *ex-situ* and agreed with the value obtained from counting the RHEED oscillations. After growth, a post growth anneal is performed at 600 Torr of oxygen while the sample cools. To grow LAO/STO heterostructures, the sample was cooled down to 600°C after

depositing STO. LAO was grown by conventional PLD where 750°C was the growth temperature, 7.5 × 10^{-5} Torr was the oxygen partial pressure, 1.0 J/cm^2 was the energy fluence, and 1 Hz was the repetition rate. After LAO was grown, the sample was annealed at 600°C in 150 Torr of oxygen for 1 hour before

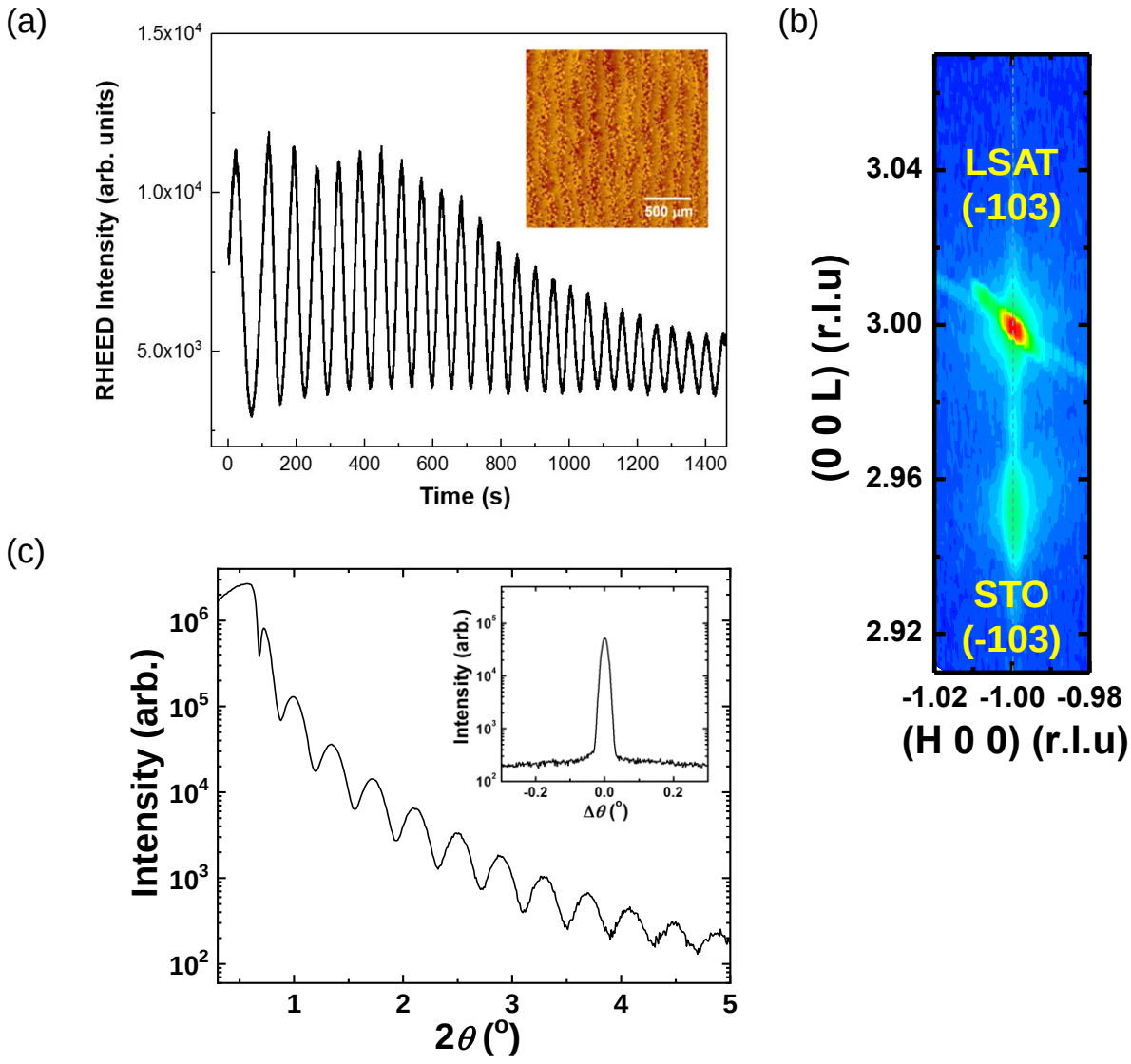

Figure 5-7: Characterization of MOPLD grown $SrTiO_3$ thin films on LSAT. (a) Intensity of the RHEED spot during deposition. Each oscillation of the spot intensity represents deposition of one unit cell of STO. Atomic force microscopy image of the atomically flat surface is shown inset. (b) X-ray diffraction reciprocal space map (RSM) of the (-103) peak of the substrate and thin film. (c) X-ray reflectometry (XRR) showing oscillations from the thickness of the thin film. Inset is the rocking curve plot of (002) thin film x-ray diffraction peak.

cooling down further. To perform four-probe Van der Pauw measurements, the sample was mounted to a chip carrier with aluminum wires ultrasonically wire-bonded to the sample corners.

5.5 Characterization

The quality of the MOPLD grown STO was evaluated using a variety of different characterization techniques. These techniques can be divided into two main groupings. One group, where the structural properties of the STO was analyzed which are sensitive to the stoichiometry. The other grouping characterized the amount of impurity scattering from defects that arise from off-stoichiometric growth in the STO using the electrical properties of a conductive STO interface. To further analyze impurities, the defect concentrations were directly measured by cathode luminescence spectroscopy.

5.5.1 Structural Characterization by X-ray Diffraction and Raman Spectroscopy

When Sr or Ti are in excess in STO, volume expansion occurs[8,13,14] which can be measured with x-ray diffraction (XRD). Volume expansion can also allow increased amounts of oxygen vacancies (V_O) to be present in the film[13], a type of defect in the crystalline structure where an oxygen atom is missing. Homoepitaxially STO films with a thickness of 25 u.c. were grown by MOPLD on STO (001) single crystal substrates using a range of TTIP gas foreline pressures from 9 mTorr to 23 mTorr producing a range of STO thin films from Ti-rich to stoichiometric to Sr-rich. Out-of-plane θ-2θ XRD patterns centered around the STO (002) diffraction peak (Figure 5-8a) were taken of each film using a Bruker D8 Discover diffractometer with a point detector and a $Cu_{K\alpha}$ source (λ = 1.5406 Å). The (002) peak was chosen as it has the highest structure factor for perovskite-type materials. Since the expansion of the lattice parameter is highly dependent on the film's stoichiometry, shifting of the film peak away from the bulk substrate peak would imply off-stoichiometry. The scans show a window of foreline pressures (11 to 21 mTorr) where the film peak directly overlaps the peak of the substrate. No discernible difference in the film peak is seen implying identical structural characteristics of these films. At lower foreline pressures (9 and 10 mTorr),

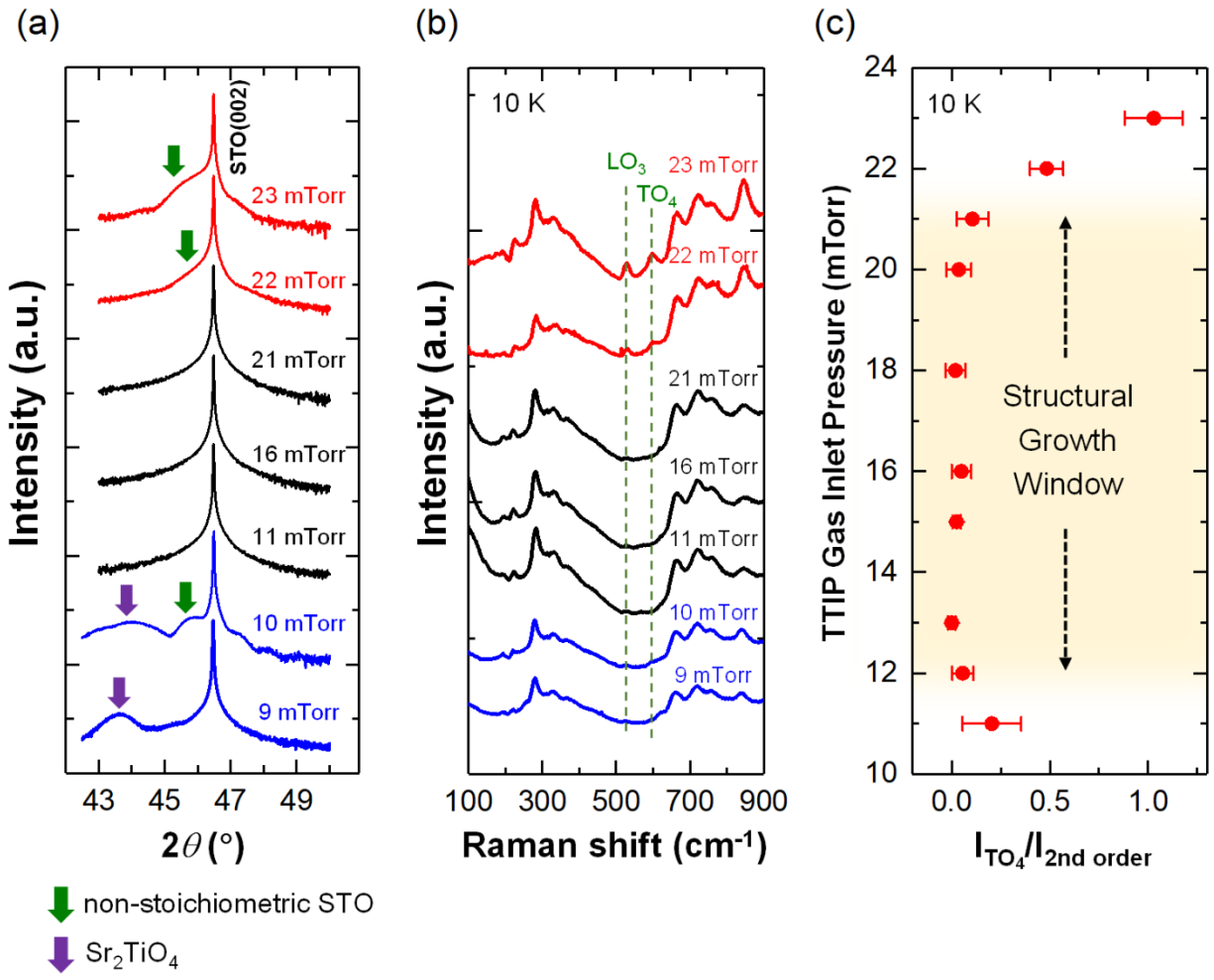

Figure 5-8: Structural analysis of MOPLD grown $SrTiO_3$ thin films on STO. X-ray out-of-plane θ-2θ patterns of the STO (002) peak for thin films grown at different foreline pressures with Sr-rich in blue, stoichiometric in black, and Ti-rich in red. Peaks from non-stoichiometric STO are denoted by the green arrows and peaks from Sr_2TiO_4 are denoted by the purple arrows. (b) Raman spectroscopy spectra of thin films grown at different foreline pressures. First order Raman peak positions are denoted by the green dashed line. (c) Ratio of the Raman spectra peak intensity of the first order peak TO_4 at 550 cm^{-1} to the second order peak at 620 cm^{-1} for thin films grown at different foreline pressures. The growth window is denoted in yellow for films with no discernible first order peaks.

the film peak is shifted to lower angles implying a lattice expansion from off-stoichiometry. A second phase peak is also present which can be attributed to Sr-rich Sr_2TiO_4. At higher foreline pressures (22 and 23 mTorr), the film peak is also shifted to lower angles indicative of Ti-rich STO. The further away the foreline pressure is from the window, lower or higher, the further the film peak is shifted to lower angles and the

more off stoichiometric the film is. The absence of any interference fringing on the film peaks from the growth window confirms the stoichiometry of the film and that contamination at the interface that might cause an offset are not present and have been desorbed by the high growth temperature[15].

The structure of the MOPLD grown STO was further characterized by performing low temperature Raman spectroscopy. Ideally, STO has a cubic crystalline structure ($Pm\bar{3}m$ space group) which has 12 unique optical phonon modes[16] all of which have odd symmetry with respect to the inversion symmetry and are inactive and don't appear in the Raman spectra. Only second order or two-phonon features appear in the spectra[17]. However, if the inversion symmetry is broken due to a distortion of the crystal structure, the first order will appear in the spectra. By testing for the presence of first order peaks (specifically the LO_3 and TO_4 modes), we can determine if the STO film is stoichiometric. Raman spectra, shown in Figure 5-8b, were taken using a Horiba Jobin Yvon T64000 triple spectrometer equipped with a LN_2-cooled multichannel CCD detector. Spectra were recorded in backscattering geometry at 10 K, using a variable temperature closed cycle He cryostat. A 325 nm He–Cd laser was used for excitation with a laser power density below 0.5 W/mm^2 at the sample surface to avoid local heating of the sample. The TO_4 peak (~550 cm^{-1}) was used for analysis of symmetry breakdown. This peak was chosen because it does not overlap with any second order peaks. The intensity of the peak was normalized to the intensity of the broad second order peak at 620 cm^{-1} to quantitatively plot the stoichiometry in Figure 5-8c. MOPLD grown STO over an identical range of TTIP gas foreline pressures as used to measure XRD were measured. The presence of first order peaks LO_3 and TO_4 in the Ti-rich STO films grown at TTIP gas foreline pressures of 22 and 23 mTorr is apparent. For foreline pressures from 12 to 21 mTorr, no first order peaks are present agreeing with the window of growth parameters that yield stochiometric thin films determined by XRD. Weak first order peaks are again present in Sr-rich STO thin films grown at low foreline pressures (9 to 11 mTorr). The window determined by Raman spectroscopy is noticeably narrower than that calculated from XRD implying that the Raman spectra is more sensitive to structural distortion and thus defects than XRD.

5.5.2 LAO/STO Two-dimensional Electron Gas

Electron mobility at low temperatures (< 5 K) is dominated by impurity scattering. Thus, electron mobility can be directly related to the concentration of defects in the system. As a model system, electron mobility of the two-dimensional electron gas (2DEG) at the interface between $SrTiO_3$ and $LaAlO_3$ can be used to test the stoichiometric control of MOPLD. STO films with a thickness of 12 u.c. were grown by MOPLD using a range of TTIP gas foreline pressures from 12 to 24 mTorr followed by a 5 u.c. thick LAO film grown by conventional PLD. The low temperature (T = 2 K) electron mobility of each sample was then taken (Figure 5-9a). In the range of 15 to 21 mTorr of TTIP gas foreline pressure, the LAO/STO interface was found to be conducting with electron mobilities increasing with increasing foreline pressure within this range. Below the range window (12 and 13 mTorr), the interface was insulating. An insulating interface was also observed at high TTIP gas foreline pressure (24 mTorr). At 22 and 23 mTorr, the interface was conducting but the mobility was reduced. The highest mobility observed with MOPLD grown STO was on the Ti-rich side of the window (21 mTorr) and had a mobility of ~6,260 $cm^2/V{\cdot}s$ at 2 K. The interface of LAO/STO where the STO is grown by conventional PLD is typically insulating while the interface when a

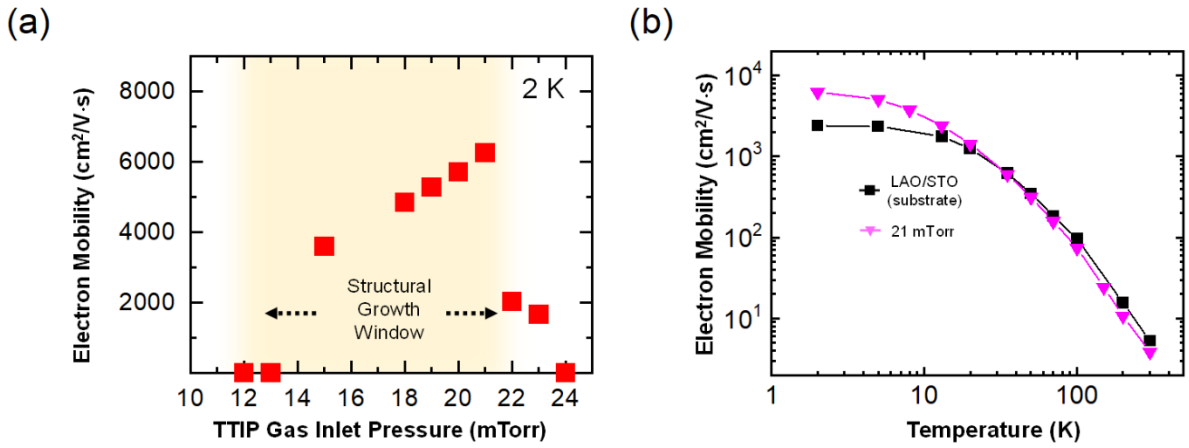

Figure 5-9: Electrical properties of 2DEG at LAO/STO interfaces. (a) The electron mobility versus TTIP gas inlet pressure of LAO 5 u.c./MOPLD-grown STO 12 u.c./STO (001) substrate taken at 2K. The structural growth window determined by XRD and Raman spectroscopy is denoted in yellow. (b) Temperature dependence of electron mobility of the 2DEG at the interface between LAO 5 u.c./MOPLD-grown STO 12 u.c./STO (001) substrate (in pink) and LAO 5 u.c./STO (001) substrate (in black).

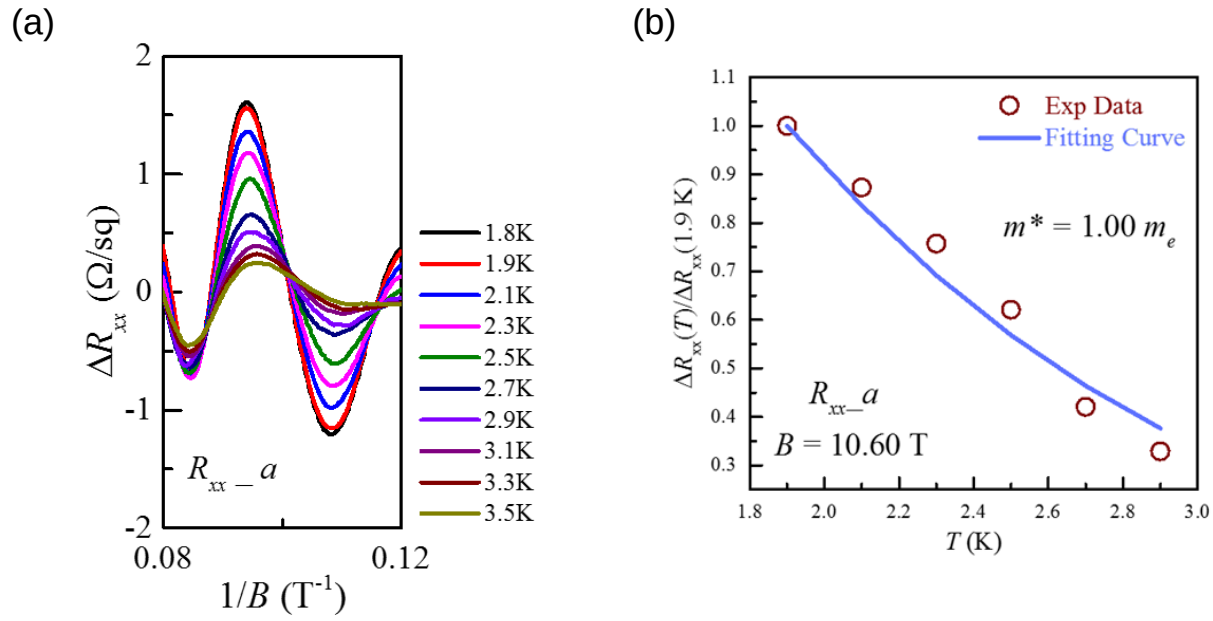

Figure 5-10: Quantum properties of 2DEG at LAO/STO interfaces. (a) Shubnikov-de Hass (SdH) oscillations of 2DEG at LAO 5 u.c./MOPLD-grown STO 12 u.c./ (001) STO substrate where TTIP gas inlet pressure of 21 mTorr was used. Data was collected at the temperature range of 1.8-3.5 K. (b) Temperature dependence of the amplitude of the SdH oscillations taken at B = 10.60 T. Effective electron mass is calculated using the temperature dependence of the oscillations.

STO single crystal substrate has a mobility of ~2,400 $cm^2/V{\cdot}s$. In Figure 5-9b, electron mobility temperature dependence (2 to 300 K) for the best LAO/STO with MOPLD grown STO was plotted against LAO/STO with bulk STO of the substrate. It follows that the MOPLD grown STO has less impurities that could cause scattering than a STO single crystal substrate which has less impurities than a conventional PLD grown STO. In all three cases, the LAO layer was grown by conventional PLD under the same growth conditions.

The LAO/STO 2DEG can further be characterized by analyzing the Shubnikov – de Haas (SdH) oscillations in the 2DEG conductivity at low temperatures in the presence of high magnetic fields (Figure 5-10a). SdH oscillations are a macroscopic effect of the quantum mechanical nature of the material. At low temperatures, conduction band electrons behave like simple harmonic oscillators which change period directly dependent on magnetic field strength. The low defect concentration in the 2DEG with MOPLD grown STO means clear SdH oscillations can be observed. From the amplitude of the SdH oscillations

(Figure 5-10b) at each temperature, we extracted the effective electron mass of 1.0 me, partial carrier density of 1.7×10^{12} cm^{-2}, and a quantum mobility of 1,500 $cm^2/V\cdot s$. These values exceed those measured for the LAO/STO 2DEG made using a STO single crystal substrate. A CRYOGENIC cryogen-free system was used to measure the SdH oscillations with a magnetic field strength of up to 16 T and at 0.2 K temperature steps from 1.8 to 3.1 K.

5.5.3 Defect Analysis using Depth Resolved Cathodoluminescence Spectroscopy

To directly probe the type of defects and their concentrations in the MOPLD grown STO, we performed depth resolved cathodoluminescence spectroscopy (DRCLS). Figure 5-11a is a schematic of how DRCLS measurements are accomplished. A parabolic mirror collects photons emitted from the surface of the sample

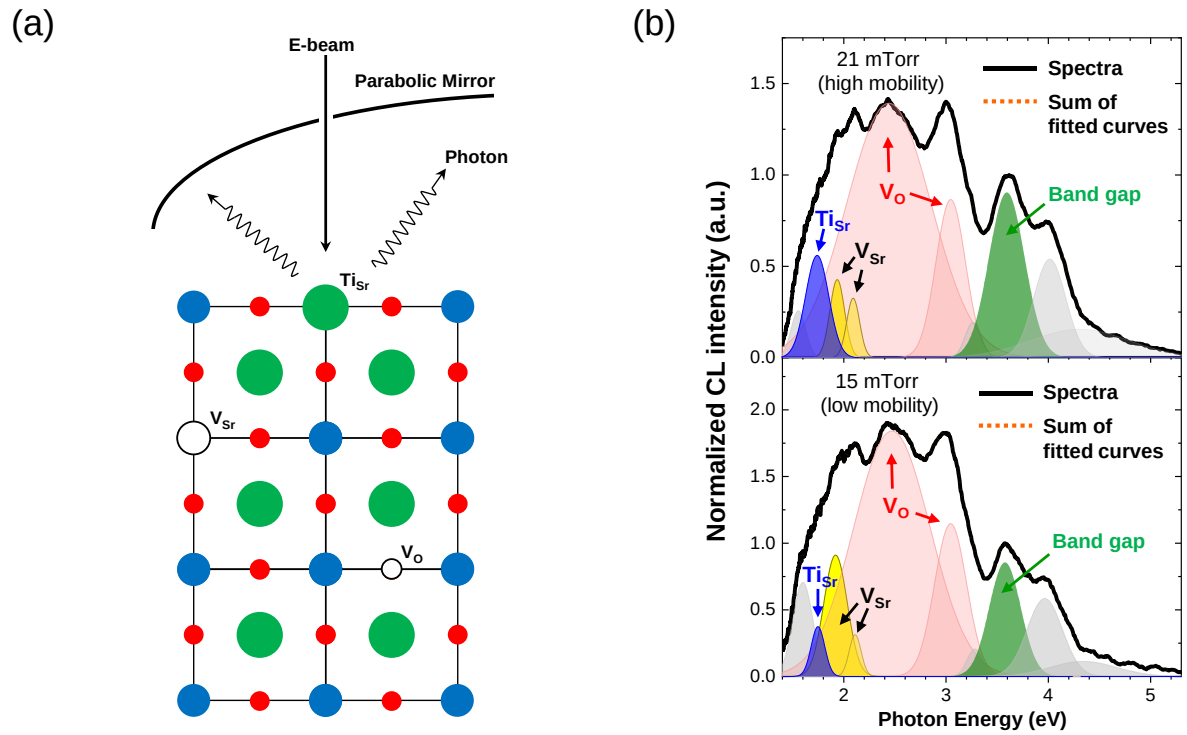

Figure 5-11: Depth resolved cathodoluminescence spectroscopy (DRCLS) of MOPLD-grown STO. (a) Cathodoluminescence spectroscopy uses an electron beam to interact with the material which causes luminescence. The emitted photons are collected by the parabolic mirror. Different types of defects in the material have characteristic energies associated with them. Energy of the electron beam changes the depth profile of the electron-solid interactions. (b) Cathodoluminescence spectra of Ti-rich (top) and Sr-rich (bottom) MOPLD grown STO thin films.

and directs them into a spectrometer. The electrons that excite the sample are collimated into a beam that passes through a hole in the parabolic mirror. In a defect-free semiconductor, photons that luminesce have an energy equal to the energy difference between the conduction band and the valance band (band gap). If defects are present in the semiconductor additional defect energy levels are present in the band gap and photons can be emitted with energies equal to the difference between the conduction band and these defect energy levels. In Figure 5-11b, DRCLS spectra are collected for STO grown on the Sr-rich (15 mTorr) and Ti-rich (21 mTorr) limits of the growth window. The intensity of the spectra in the energy range from ~1.5 to ~3.4 eV is greater in the STO grown at lower TTIP gas foreline pressure (Sr-rich) implying greater concentrations of defects in the Sr-rich STO. In Figure 5-12, the intensity of the CL peak attributed to V_O defects is plotted with respect to the TTIP gas foreline pressure. A direct correlation between V_O concentration and electron mobility is seen. The concentration ratio Ti_{Sr}/V_{Sr} is found to be indirectly related to both the concentration of V_O defects and electron mobility.

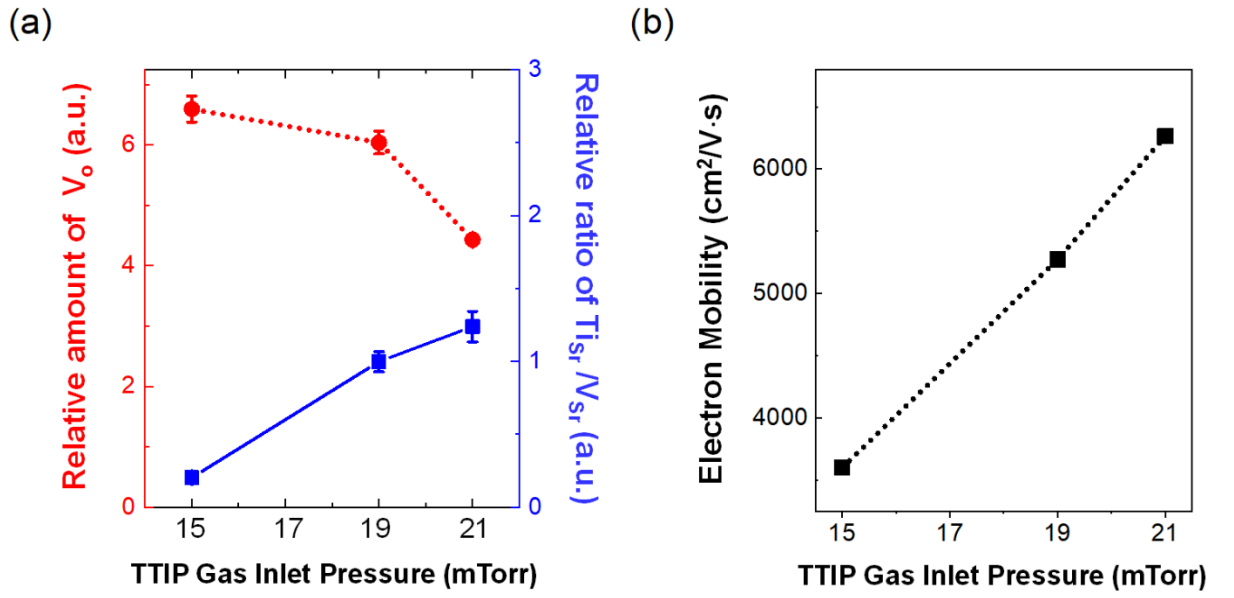

Figure 5-12: Defect concentrations and electron mobilities of 2DEG at LAO/STO interfaces for STO grown at various TTIP gas inlet pressures. (a) Relative defect concentrations in STO thin films grown at different TTIP gas inlet pressures within the adsorption-controlled growth window. (b) Electron mobility at 2K of 2DEG at the LAO/STO interface in STO thin films grown at different TTIP gas inlet pressures within the adsorption-controlled growth window.

To determine the penetration depth of electrons at various beam energies we used Monte Carlo simulations (CASINO). The simulates were used to simulate the electron energy loss as the electron interacts with the solid. To analyze the 12 u.c. MOPLD-grown STO layer underneath the 5 u.c. LAO layer in the LAO/STO 2DEG samples, 0.3 kV was selected as the beam voltage. To prevent deflection of the low energy beam, a fine copper grid was placed over the sample surface to ground the surface and reduce surface charge buildup.

5.6 Future Directions for MOPLD

While our work on MOPLD has so far been limited to Ti metal-organic precursors, a variety of elements have been supplied by chemical sources for hybrid MBE including Li, Al, Ti, V, Y, Zr, Nb, Sn, Hf, and Dy[18]. Complex oxides that contain these elements should theoretically also have adsorption-controlled growth windows when grown by MOPLD. Additionally, MOPLD could be useful for doping of the oxygen

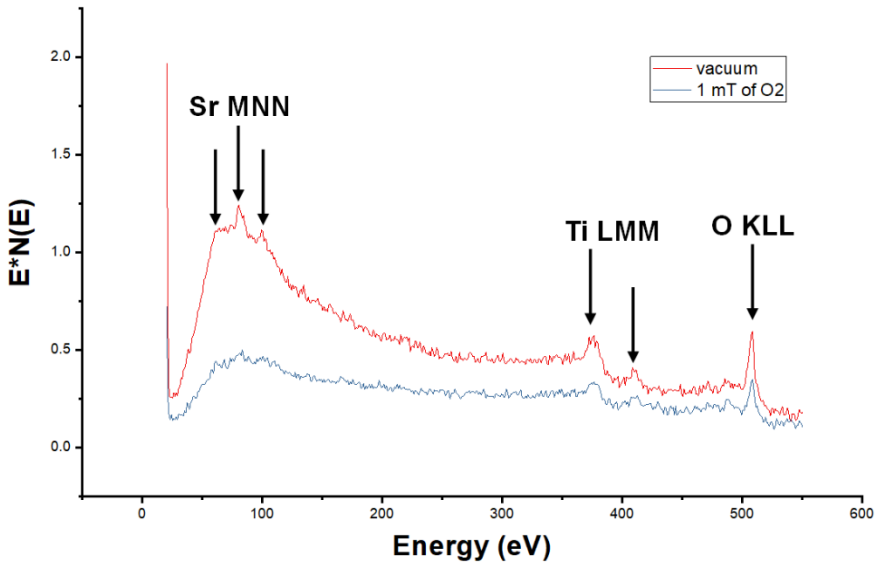

Figure 5-13: Auger spectra of $SrTiO_3$ (001) single crystal substrate. The auger spectra of a STO (001) orientated single crystal substrate taken under high vacuum and at 1 mTorr of oxygen gas in the MOPLD chamber. The characteristic energy peaks for Sr, Ti, and O are annotated.

site of a complex oxide to form an oxynitride. Other Ti metal-organic precursors are available including tetrakis(dimethylamido)titanium(IV) (TDMAT) which is a precursor designed for the deposition of TiN. Providing TDMAT in addition to TTIP when growing STO by MOPLD could lead to $SrTiO_{1-x}N_x$. Nitrogen doping of STO has been theorized to be a pathway to p-type STO[19,20] which has remained elusive compared to n-type STO (by doping with Nb^{5+}, La^{3+}, or Y^{3+}). Conventional PLD requires a bulk ablation target. Growth of complex oxides that are difficult to synthesize a bulk target of or are only stabilized by substrate-induced strain could benefit from being grown by MOPLD.

Additional *in-situ* growth characterization techniques may be useful in speeding up the time to map the growth window. Recently, an Auger spectrometer was installed in our custom MOPLD system enabling *in-situ* elemental analysis of the surface of the film. The Auger spectrometer collects electrons with elementally specific energies and uses the RHEED electron source to provide the incident electrons. The energy of Auger electrons given off by a certain element is determined by the difference in electron shell energy levels. While the PLD ablation plume was found to saturate the photodetector of the spectrometer, data could be collected between pulses or by pausing the laser pulses. While the best signal to noise ratio was when no gases were present in the system, elemental peaks were still observable up to 1 mTorr of growth pressure as seen in Figure 5-13.

5.7 References

1. Cardona, M. Optical properties and band structure of SrTiO3 and BaTiO3. *Phys. Rev.* **140**, (1965).
2. Müller, K. A. & Burkard, H. SrTiO3: An intrinsic quantum paraelectric below 4 K. *Phys. Rev. B* **19**, 3593–3602 (1979).
3. Weaver, H. E. Dielectric properties of single crystals of SrTiO3 at low temperatures. *J. Phys. Chem. Solids* **11**, 274–277 (1959).
4. Schooley, J. F., Hosler, W. R. & Cohen, M. L. Superconductivity in Semiconducting SrTiO3. *Phys. Rev. Lett.* **12**, 474–475 (1964).
5. Gastiasoro, M. N., Ruhman, J. & Fernandes, R. M. Superconductivity in dilute SrTiO3: A review. *Ann. Phys. (N. Y).* **417**, (2020).

6. Reyren, N. *et al.* Superconducting Interfaces Between Insulating Oxides. *Science (80-.).* **317**, 1196–1199 (2007).

7. Ohtomo, A. & Hwang, H. Y. A high-mobility electron gas at the LaAlO3/SrTiO3 heterointerface. *Nature* **427**, 423–426 (2004).

8. Jalan, B., Engel-Herbert, R., Wright, N. J. & Stemmer, S. Growth of high-quality SrTiO3 films using a hybrid molecular beam epitaxy approach. *J. Vac. Sci. Technol. A Vacuum, Surfaces, Film.* **27**, 461 (2009).

9. Taylor, C. J. *et al.* Does chemistry really matter in the chemical vapor deposition of titanium dioxide? Precursor and kinetic effects on the microstructure of polycrystalline films. *J. Am. Chem. Soc.* **121**, 5220–5229 (1999).

10. Jalan, B., Moetakef, P. & Stemmer, S. Molecular beam epitaxy of SrTiO3 with a growth window. *Appl. Phys. Lett.* **95**, 1–4 (2009).

11. Ahn, K. H., Park, Y. B. & Park, D. W. Kinetic and mechanistic study on the chemical vapor deposition of titanium dioxide thin films by in situ FT-IR using TTIP. *Surf. Coatings Technol.* **171**, 198–204 (2003).

12. Buerger, P., Nurkowski, D., Akroyd, J. & Kraft, M. A kinetic mechanism for the thermal decomposition of titanium tetraisopropoxide. *Proc. Combust. Inst.* **36**, 1019–1027 (2017).

13. Ohnishi, T., Shibuya, K., Yamamoto, T. & Lippmaa, M. Defects and transport in complex oxide thin films. *J. Appl. Phys.* **103**, (2008).

14. Brooks, C. M. *et al.* Growth of homoepitaxial SrTiO3 thin films by molecular-beam epitaxy. *Appl. Phys. Lett.* **94**, 1–4 (2009).

15. Lebeau, J. M. *et al.* Stoichiometry optimization of homoepitaxial oxide thin films using x-ray diffraction. *Appl. Phys. Lett.* **95**, 10–13 (2009).

16. Tenne, D. A. *et al.* Ferroelectricity in nonstoichiometric SrTiO3 films studied by ultraviolet Raman spectroscopy. *Appl. Phys. Lett.* **97**, 1–4 (2010).

17. Narayanan, P. S. & Vedam, K. Raman spectrum of strontium titanate. *Zeitschrift für Phys.* **163**, 158–164 (1961).

18. Brahlek, M. *et al.* Frontiers in the Growth of Complex Oxide Thin Films: Past, Present, and Future of Hybrid MBE. *Adv. Funct. Mater.* **28**, 1–41 (2018).

19. Betsuyaku, K., Tanaka, H., Katayama-Yoshida, H. & Kawai, T. Material design for the fabrication of p-type SrTiO3. *Japanese J. Appl. Physics, Part 1 Regul. Pap. Short Notes Rev. Pap.* **40**, 6911–6912 (2001).

20. Wei, W., Dai, Y., Guo, M., Yu, L. & Huang, B. Density functional characterization of the electronic structure and optical properties of N-doped, La-doped, and N/La-codoped SrTiO3. *J. Phys. Chem. C* **113**, 15046–15050 (2009).

21. Jalan, B. Hybrid Molecular Beam Epitaxy for High Quality SrTiO3 Films. (University of California, Santa Barbara, 2011).

Chapter 6

Conclusions

6.1 Summary

The goal of this thesis was to present how we solved uniquely challenging epitaxial thin film quality requirements using innovative deposition techniques. Along with explaining how quality thin films were obtained, the research and discoveries that the thin films unlocked was also presented.

Chapters 2 and 3 covered the method by which monodomain $BiFeO_3$ thin films are sputtered. While the unique dual off-axis sputtering technique used to deposit $BiFeO_3$ thin films has already been reported, we extend the usefulness of this technique by developing a system to enable *in-situ* deposition of metallic overlayers such as Py and Pt using DC magnetron sputtering, all without changing the deposition system that has been optimized for the deposition of $BiFeO_3$. This enabled work to quantify the spin transport properties of monodomain $BiFeO_3$ using local and nonlocal device geometries. The ability to deposit high quality $BiFeO_3$ with thicknesses of 1 μm or more was used to study the domain populations in $(111)_{pc}$-oriented $BiFeO_3$ on cubic and reduced symmetry substrates. The typical method of depositing epitaxial $BiFeO_3$ by pulsed laser deposition would have difficulties depositing films of this thickness. The large thickness increased the amount of material that could scatter incident x-rays and neutrons which was used to confirm that we created a monodomain $(111)_{pc}$-orientated $BiFeO_3$ thin film with a single ferroelastic, ferroelectric, and antiferromagnetic domain across the entire sample.

In Chapter 4, we needed epitaxial thin films of α-Fe_2O_3 with no minority phases of Fe_3O_4, γ-Fe_2O_3, or Fe. The ferromagnetic signature from the presence of any of these minority phases would overpower the weak signal from the antiferromagnetic canted moment in α-Fe_2O_3 and hinder the study of the Morin phase transition. This was indeed the case for α-Fe_2O_3 thin films deposited using RF sputtering of a stoichiometric α-Fe_2O_3 sputtering target. The SQUID magnetometry results were saturated by the broad Verwey transition occurring in nanometer-sized secondary phases of Fe_3O_4. Not until reactive RF sputtering was used to deposit α-Fe_2O_3 was the Morin transition clearly visible in the SQUID magnetometry data revealing the suppression of the transition for ultrathin α-Fe_2O_3 films. A detailed study was then conducted to fully map the antiferromagnetic spin direction in the films revealing a complex pattern of sub-micron size antiferromagnetic domains with vortices at the singular points where domains meet their anti-phase domain counterparts.

Finally, in Chapter 5 a novel new deposition technique was presented combining the high energy deposition technique of pulsed laser deposition with the near equilibrium process of metal-organic chemical vapor deposition in a new process we called MOPLD. The absorption-controlled growth window afforded by the desorption of excess metal-organic precursor at high temperatures (>800°C) allowed for a wide range of growth conditions to yield an identical quality of epitaxial thin film. The increased quality of the $SrTiO_3$ (001) thin films deposited using MOPLD yielded repeatably conductive heterointerface between $SrTiO_3$ and $LaAlO_3$ thin films. Further study of these high quality 2-dimensional electron gases at the oxide interface revealed quantum properties such as Shubnikov-de Hass oscillations at low temperatures (~2 K).

6.2 Future work

The work presented here is a mix of new research projects and long-standing projects. It is hoped that for each project, significant progress has been made to further each project's goals and that work continues to be done to further build on the scientific discoveries reported here. Research into $BiFeO_3$ thin films is one

such long-standing project with RF sputtering of $BiFeO_3$ thin films ongoing in the lab for over two decades as lab members continue to discover new properties and new uses for the material. The upgraded ability to deposit metallic thin films *in-situ* unlocked new research avenues in the field of spintronics that the existing $BiFeO_3$ RF sputtering deposition system could not accomplish. While the research that this new capability opened is still in progress, our work so far warrants a brief overview here.

6.2.1 Spin Hall Magnetoresistance of $BiFeO_3$ Thin Films

Spin Hall magnetoresistance (SMR) could serve as a powerful electrical transport-type technique for interacting with and reading out the antiferromagnetic state of the $BiFeO_3$ thin film without the use of a ferromagnetic overlayer[1,2]. The effect is based on the interfacial exchange of angular momentum between the magnetic sublattices of a magnetic insulator and the conduction electrons of a heavy metal. The SMR

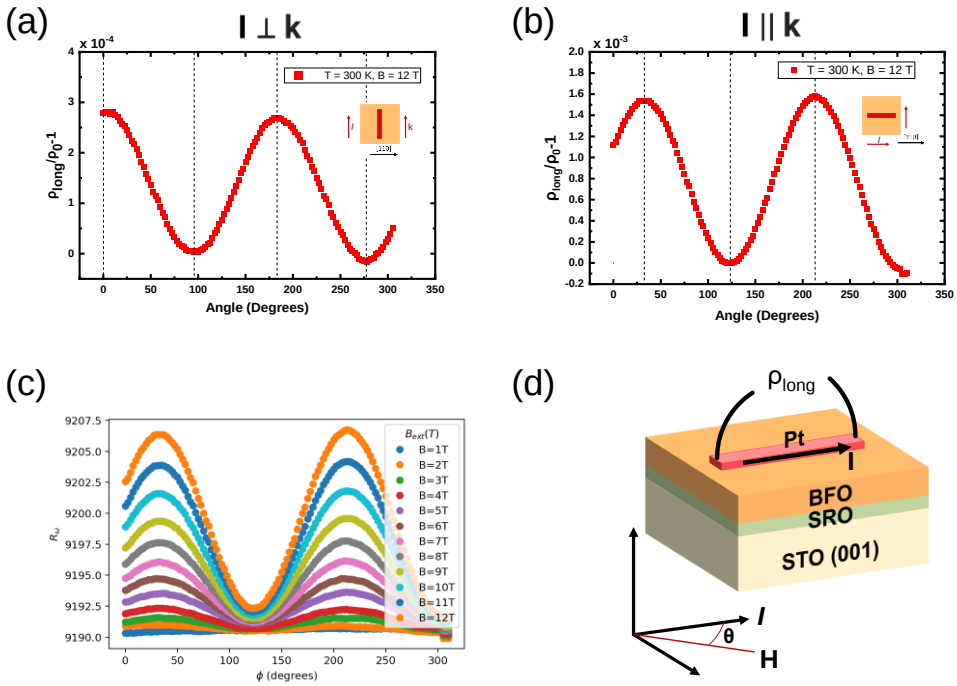

Figure 6-1: Spin Hall magnetoresistance results for monodomain $BiFeO_3$. (a-b) Angular dependence of the resistivity of the Hall bar along the longitudinal axis as a function of the angle between the external magnetic field and the Hall bar axis. Measured with the Hall bar axis (a) perpendicular and (b) parallel to the spin cycloid propagation vector. (c) Quadratic dependence of SMR amplitude on the strength of the applied magnetic field. (d) Schematic of the SMR device.

effect is useful in the study of both ferromagnetic[3–5] and antiferromagnetic[6,7] insulators (FMI and AFI respectively). While electrically insulating, this class of materials exhibits long-range magnetic ordering that allow the propagation of magnetic excitations (spin currents) to flow through the material, a useful property that could be harnessed to make a spintronic device.

A Hall bar of Pt is deposited *in-situ* onto the $BiFeO_3$ thin film (Figure 6-1d). Patterning of the Hall bar is done using Ar ion milling. A current is passed through the Hall bar and the external magnetic field angle dependence of the Hall bar longitudinal resistance is measured (Figure 6-1a-b). We report that we see a large SMR signal for monodomain $BiFeO_3$ $(001)_{pc}$ thin films grown on highly miscut $SrTiO_3$ $(001)_{pc}$ substrates and that the SMR signal has a quadratic dependence on the applied magnetic field strength (Figure 6-1c). Further work is determining the effect ferroelectric switching of the $BiFeO_3$ has on the measured SMR signal.

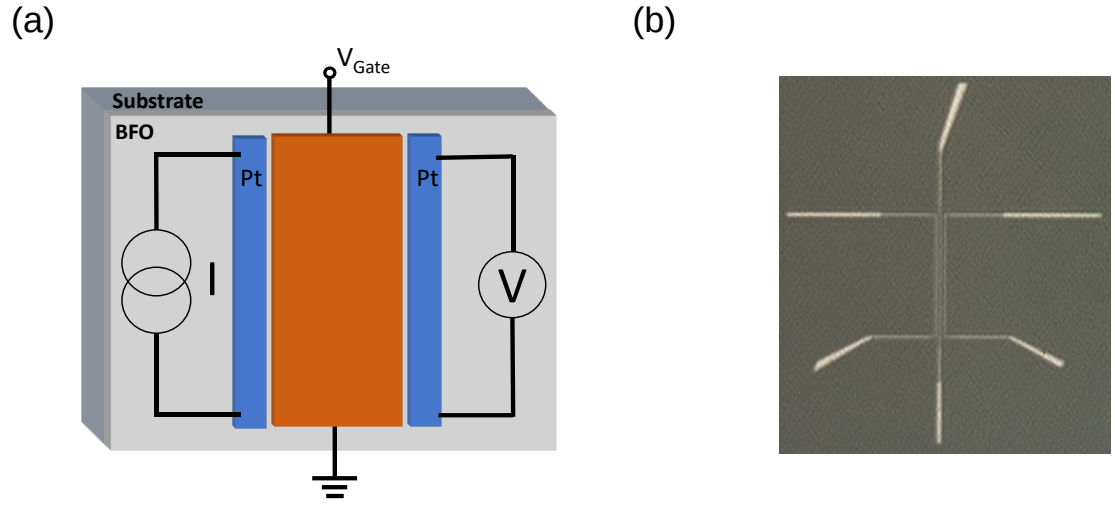

Figure 6-2: Nonlocal spin transport device. (a) Schematic of the experimental device. A current is applied to one nanowire while the voltage is measured on the other. The nanowire in the middle is used to switch the $BiFeO_3$ between the two electrodes. (b) Optical microscopy image of the typical device patterned on Pt (10 nm) / $BiFeO_3$ (300 nm) / $SrRuO_3$ (30 nm) / $SrTiO_3$ (001) miscut 4°→ $(110)_{pc}$. The electrodes are 20 μm long and 200 nm wide with a separation of 1 μm. The checkboard pattern of the background is the surface topology of $BiFeO_3$ on highly miscut substrates.

6.2.2 Measurement of Long-Range Spin Transport in Monodomain $BiFeO_3$

As discussed in Chapter 3, we are working to understand the spin transport properties of monodomain $BiFeO_3$. So far, we have made a series of local devices with spins transporting through each thickness with seeming no loss in intensity. A nonlocal device geometry is needed to measure longer spin transport distances. We aim to go a step further by adding antiferromagnetic domains between the nonlocal electrodes by ferroelectric switching of the $BiFeO_3$ (Figure 6-2). With this study, we hope to better understand the effect domain walls plays on spin transport.

6.3 References

1. Heron, J. T. *et al.* Deterministic switching of ferromagnetism at room temperature using an electric field. *Nature* **516**, 370–373 (2014).
2. Saenrang, W. *et al.* Deterministic and robust room-temperature exchange coupling in monodomain multiferroic BiFeO3 heterostructures. *Nat. Commun.* **8**, (2017).
3. Nakayama, H. *et al.* Spin Hall Magnetoresistance Induced by a Nonequilibrium Proximity Effect. *Phys. Rev. Lett.* **110**, 1–5 (2013).
4. Althammer, M. *et al.* Quantitative study of the spin Hall magnetoresistance in ferromagnetic insulator/normal metal hybrids. *Phys. Rev. B* **87**, 224401 (2013).
5. Ganzhorn, K. *et al.* Spin Hall magnetoresistance in a canted ferrimagnet. *Phys. Rev. B* **94**, 94401 (2016).
6. Fischer, J. *et al.* Spin Hall magnetoresistance in antiferromagnet/heavy-metal heterostructures. *Phys. Rev. B* **97**, 14417 (2018).
7. Fischer, J. *et al.* Large Spin Hall Magnetoresistance in Antiferromagnetic α-Fe 2 O 3 /Pt Heterostructures. *Phys. Rev. Appl.* **10**, (2020).